FRACTURE BEHAVIOUR OF COPPER STRENGTHENED HSLA STEEL

by

Swapan Kumar Das

A thesis submitted for the degree of

Doctor of Philosophy (Engineering)

of the

Bengal Engineering and Science University, Shibpur

Department of Metallurgy & Materials Engineering
Bengal Engineering and Science University, Shibpur
Howrah 711 103, West Bengal, India

January, 2007

FRACTURE BEHAVIOUR OF COPPER STRENGTHENED HSLA STEEL

by

Swapan Kumar Das

a Thesis Submitted for the Degree of

Doctor of Philosophy (Engineering)

of the

Bengal Engineering and Science University, Shibpur

Department of Metallurgy & Materials Engineering
Bengal Engineering and Science University, Shibpur
Howrah 711 103, West Bengal, India

January, 2007

Acknowledgements

I take this opportunity to express my sincere gratitude to Professor S. Chatterjee, Head, Department of Metallurgy and Materials Engineering, Bengal Engineering and Science University (BESU), Shibpur, and Dr. S. Tarafder, Deputy Director, Materials Science and Technology Division, National Metallurgical Laboratory (NML), Jamshedpur, for their guidance, supervision, suggestions and discussion throughout the research work and during the preparation of this thesis. Their encouragements and inspiration were the driving force behind this programme.

I express my sincere gratitude to Professor S.P. Mehrotra, Director, NML, Jamshedpur and Professor N.R. Banerjea, Vice-Chancellor, BESU, Shibpur, for their permission and provision of facilities to carry out this research programme successfully.

I am grateful to Dr. R.N. Ghosh, Head, Materials Science and Technology Division, NML, Jamshedpur, for his advice and support in carrying out the present work.

I gratefully acknowledge the moral support received from Professor P.S. Banerjee and other faculty members of the Department of Metallurgy and Materials Engineering, BESU, Shibpur. I express my sincere thanks to all the staff members of the Department of Metallurgy and Materials Engineering, for their help and co-operation.

I am thankful to Dr. A. Mitra, Dr. I. Chattoraj, Dr. Samar Das and Dr. S. Sivaprasad of NML, Jamshedpur, for their valuable suggestions, support and encouragements during the course of this work. Their support has considerably enhanced the quality of the work performed.

I am indebted to Dr. N. Narasiah, Dr. M. Ghosh, Dr. A.K. Panda, Mr. P.K. Dey and other colleagues at NML, Jamshedpur for their kind help and co-operation.

I will be failing in my duty if I do not record the support and co-operation of Dr. S.K. Mishra and Mrs. M. Tarafder. The advice, encouragements and suggestions of numerous other friends and colleagues during the course of this research work, whom I am unable to name individually, will be remembered and cherished.

I am thankful to my wife Sukla and son Aniruddha for their love and patience in achieving this milestone.

Shibpur *Swapan Kumar Das*
January, 2007

Contents

List of Figures

List of Tables

Synopsis

High strength, high toughness and good weldability are the major criteria for engineering structural materials. HSLA-100 steel is essentially low carbon microalloyed and copper-strengthened high strength steel. It is one of the important materials in naval, and others structural applications in which high strength (UTS >1000 MPa) and good toughness can be obtained without impairing weldability by judiciously engineering the microstructure. This steel can provide various strength–toughness combinations over a wide range of plate thickness by different heat treatments. Available literatures concerning the influence of heat treatment on microstructure and mechanical properties are confined to the characterisation of microstructure and the variation in mechanical properties such as tensile strength and impact toughness. Such mechanical property evaluation is insufficient to characterise the mechanical behaviour of the materials. Modern engineering design approach demands a fracture mechanics based characterisation of material behaviour.

The deformation and fracture behaviour of material is controlled by its microstructure. Desired microstructural constituents in HSLA steel can be optimised through microstructural engineering by adopting a combination of thermo-mechanical controlled process (TMCP), along with accelerated controlled cooling (ACC). The optimisation of different microstructural constituents can also be achieved through different processes like rolling and ageing, normalising and ageing, quenching and ageing etc.

A brief description of the subject matter, pertaining to the study forms the content of Chapter-1: introduction. Chapter-2: literature review reveals the important and relevance studies carried out in HSLA steels with a focus on physical metallurgy of HSLA steel, assessment of microstructural evolution by differential scanning calorimetry (DSC) study and magnetic techniques, fatigue and fracture behaviour of material. Various phases associated with the evolution of microstructure have been described. Role of various alloying elements relevant to the present study has also been discussed. As the processing parameters have strong influence on the microstructure and mechanical properties of steel, this aspect has also been included in this chapter. The mechanisms which are operative in strengthening of these categories of steels have

been elucidated. Chapter-3 describes the experimental work related to heat-treatment and characterisation of HSLA-100 steel. Microstructural modification through solution treatment followed by quenching and ageing has been discussed in this chapter. Microstructural characterisation by electron microscopy, evaluation of mechanical properties like hardness and tensile properties are included in the chapter. Variation of microstructures and mechanical properties of the steel on ageing have also been discussed in Chapter-3. In view of the changes in magnetic properties with structural modification, magnetic techniques can be used for microstructural assessment for structural component by non-invasive way. Chapter-4 describes indirect assessment of the microstructural evolution of the material using magnetic hysterisis loop and magnetic Barkhausen emission techniques. In this chapter the effect of precipitation of copper in HSLA–100 steel on the magnetic properties has been evaluated and the kinetics of copper precipitation process has been highlighted using differential scanning calorimeter. Chapter-5 is associated with the influence of various ageing treatments on the fatigue crack growth (FCGR) behaviour of the steel. Microstructure exhibiting same tensile and hardness properties may not offer same resistance to fracture. Chapter-6 consists of a deeper understanding on the effect of different microstructure on fracture behaviour and fracture mechanics parameters. Finally, Chapter-7 consists of the summary and conclusions drawn from the present investigation.

The material used in this study was Cu-strengthened HSLA-100 steel that was developed for naval structural use demanding high strength and toughness together with enhanced weldability. Carbon is kept at a very low level (0.04 wt%) to improve the weldability, and a substantially high content of Ni (3.50 wt%) is provided for increasing the hardenability and improving the hot workability of the steel. Microalloying with Ti, V and Nb induces strengthening via stable carbide and carbo-nitride precipitations. The high amount of Cu (1.60 wt%) in the steel is necessary for obtaining additional precipitation strengthening through quenching and ageing heat treatments that can be designed to provide optimum combination of strength and toughness required for specific applications. The material was available in the form of flat plates from which blanks were machined with their axes oriented along the rolling direction for the fabrication of tensile and fracture specimens. These were austenitised for 1 hour at 910^{o}C and water quenched (WQ). The quenched specimens were then aged for 1 hour at various temperatures between 350^{o}C to 750^{o}C in steps of 50^{o}C and few additional

blanks were aged at 675^{o}C in order to produce systematically varying microstructures. Some blanks were preserved after quenching treatment to investigate the as-quenched properties.

Metallographic samples were prepared from the heat treated blanks using 4% nital as the etchant and examined in a JEOL JSM 840A scanning electron microscope (SEM) equipped with Noran Quest energy dispersive X-ray (EDS) microanalysis system. More detailed microstructural characterisation was carried out with a Philips CM 200 transmission electron microscope (TEM) with EDS attachment on twinjet electro-polished thin foils prepared from 3mm discs cut from the heat treated blanks.

The mechanical properties of the various microstructures were obtained through hardness test using a computerised hardness tester in Vickers scale and through tensile tests conducted as per ASTM standard E-8M using a 100kN Instron servo hydraulic testing system. A constant displacement rate of $3x10^{-3}$ mm/s, with a 25mm gauge length extensometer mounted over the 5mm gauge diameter specimens was employed for the tests.

Magnetic hysteresis loop (MHL) and Magnetic Barkhausen emission (MBE) techniques were used to characterise the material. Magnetic hysteresis and Barkhausen emission were carried out using surface magnetising probe. Magnetic hysteresis loop was measured at a quasi-dc (50 mHz) magnetising field whereas the Barkhausen emission were measured at 40 Hz using a 30kHz-300kHz band pass filter. The Cu precipitation behaviour of the steel under study was carried out using differential scanning calorimeter (Perkin-Elmer, DSC-7). The DSC was calibrated using Zinc and Indium sample prior to the experimental run for the specimen. The heating was done in an inert atmosphere at a heating rate of 10^{o}C/min. However, various heating rates were used for activation energy calculation. The broad exothermic peak indicated the formation of nanocrystalline particle. Activation energy for this phase transformation was calculated using Kissinger plot

Single-edge notched three-point bend specimens, of 150mm (L) x 30mm (W) x 20mm (B) nominal dimensions, were employed for both FCGR and fracture toughness testing. The specimens were fabricated with integral knife-edges at the notch mouth on which a crack opening displacement (COD) gauge could be fixed for crack length

measurement using the compliance method. Tests were conducted on a 100kN Instron servo hydraulic testing system equipped with a digital controller that was interfaced to a computer for test control and data acquisition. All tests were carried out in ambient laboratory air environment. Fractographic observations were carried out on tested specimens using a SEM.

FCGR tests were conducted as per ASTM standard E-647 employing the decreasing ΔK test methodology. Tests were carried out at 15 Hz frequency with a load-ratio, R, of 0.1 under software control. Instantaneous crack lengths, crack closure levels, ΔK and crack growth rates were computed on-line by the testing software.

The single-specimen method was employed for carrying out fracture toughness tests as per ASTM standard E-1820 with the primary objective of obtaining *J-R* curves. A displacement rate of $3x10^{-3}$ mm/s was used for imposing a loading scheme consisting of concatenated sequences of loading through 0.3mm, followed by partial unloading through 0.15mm and reloading through the same amount, repeated continuously till sufficient crack growth has taken place. Software was used for test control and data acquisition, the data being analysed off-line as per the guidelines laid down in ASTM E-1820. The widths of stretch zones spanning the culmination of pre-fatigue cracks and the initiation of ductile fracture were quantified from SEM fractographs for correlation with the ductile fracture behaviour.

The microstructure in quenched condition is consisted of mixture of lath martensite, bainite and acicular ferrite along with little amount of retained austenite (RA), carbides, and carbo-nitrides. Ageing upto 500^{o}C facilitated fine coherent nano-size Cu precipitation that lost its coherency above 550^{o}C. Simultaneously, recovery of martensite and acicular ferrite occurred at higher temperatures above 550^{o}C. As the ageing temperature exceeds A_{C1} temperature, a few ferrites transform to reverted austenite and subsequently on cooling, a part of reverted austenite converts to small new martensite islands above 675^{o}C. Carbides, carbo-nitrides and retained austenite were remained unchanged upto 700^{o}C. Ageing above 700^{o}C, causes softening of the material due to formation of granular bainite, recovery of martensitic laths and acicular ferrite as well as coarsening of carbides and Cu precipitates. Therefore, specimens aged beyond

700^{o}C were excluded from magnetic characterisation as well as FCGR and fracture toughness tests in this investigation.

The hardness of the material increased with the increase in ageing temperatures and reached maximum (350 Hv) at 500^{o}C followed by a gradual decrease with a further increase in ageing temperature up to 675^{o}C. Again, hardness increased and a second maxima was observed at 700^{o}C. Hardness decreased when the steel was aged above 700^{o}C. Similar trend was observed in tensile properties like yield strength (YS) and ultimate tensile strength (UTS). The YS and UTS initially increased during ageing upto 500^{o}C and then gradually decreased during ageing up to 675^{o}C. Subsequently the increase in strength was recorded and at 700^{o}C, a second peak was observed. Strength again decreased when the steel was aged above 700^{o}C. A reverse trend was observed in percentage elongation (%EL) and in percentage reduction in area (%RA). Microstructural and fractographic studies indicate that nano size coherent copper precipitate introduces the brittleness and high strength in the material in the initial stage of ageing whereas loss of coherency of Cu precipitate in later stages causes the increase in ductility in the material. The plastic flow of the material was restricted in the initial stage of ageing (350^{o}C to 500^{o}C) due to the formation of very fine coherent Cu precipitates, which restrict the dislocations movement. Plastic flow of material again increased during ageing above 550^{o}C when Cu precipitates were coarsened and lost coherency.

The magnetic properties did not response in the same manner as that of hardness and tensile strength. The material became magnetically softer at the initial stage of ageing, which was due to the tempering of lath microstructure. The Cu precipitation did not have much influence on the magnetic softness because of the smaller size of precipitate compare to the domain wall width. However, the materials became magnetically harder when the precipitate size increased, which hindered the domain wall movement. The kinetics of Cu-precipitation was studied using differential scanning calorimeter and the activation energy was found to be 68 kCal/mol.

Variations in fatigue crack growth rate (FCGR) curve, *J-R* curve, blunting-line slope and stretch zone width (SZW) with variation in microstructure of the steel was carried out. It was observed that blunting line slope *M* i.e., slope of the initial linear region in *J-R* curve varies with ageing temperature. The slope first increased, and then

decreased and again increased with increase in temperature. The material exhibited total brittle crack extension or pop-in behaviour between 400^{o}C to 500^{o}C. A decrease in slope was observed with increase in ageing temperature above 500^{o}C and the ductile fracture behaviour of the material again sets in. The co-efficient in the tearing region and J_i as well as J_Q also showed similar trends. Beyond 500^{o}C, the ductile fracture behaviour occurred followed by a marginal increase in brittleness at 700^{o}C, owing to the formation of new martensitic islands from austenite. It was observed that although there was a systematic trend, the FCGR curves were less sensitive to microstructural changes. The variation of fracture toughness value is characterised by J_Q in most cases and by K_Q for the microstructure showing highest strength, correlated well with the inverse relationship between fracture toughness and strength. A systematic trend was also observed for the pre-exponent and exponent of the power-law tearing curve (for cases in which brittle fracture was precluded), the blunting line slope and the SZW.

From the present study, it is possible to develop an appreciation of the role played by microstructural constituents in controlling the deformation processes and the fracture behaviour of HSLA-100 steel for monotonic as well as fatigue loading. The major role played by the coherency of Cu precipitates in restricting plastic flow, as implied from the variation of mechanical properties with ageing temperature is thought to be responsible for the effects observed. Since fatigue crack growth is also governed by accumulation of damage through localised plastic deformation, precipitate coherency is an important factor in controlling its rate. The conditions under which microvoid coalescence was totally suspended in spite of a constant resident population of void initiating carbide and carbo-nitride particles, leading to brittle fracture through cleavage mode, was observed. The effect of tempering of the background matrix on fracture mechanics parameters was also evidenced. The evolution of new austenite and small martensite islands in the microstructure on ageing around 700^{o}C was responsible for a desirable combination of high strength and high toughness in the HSLA-100 steel for critical engineering applications.

Chapter 1.0

Introduction

1.0

Introduction

Low carbon, Cu containing high strength low alloy (HSLA) steels are emerging materials for naval and other structural applications due to their good combination of strength and toughness and excellent weldability. The improved weldabilty is achieved through lower concentrations of carbon. The copper addition provides the required strength through ageing. These steels can provide different combinations of strength and toughness in a wide range of plate thickness by different heat treatments. So appropriate selection of heat treatment is possible to obtain the best strength-toughness combination in these steels. However, it requires an investigation of microstructural change vis-à-vis mechanical behaviour due to various heat treatments. The assessment of integrity of any structure requires study of the fracture and fatigue resistance besides conventional mechanical property evaluation.

The deformation behaviour of a material is controlled by its microstructure. Since the event of fracture is essentially an extension and, in a sense, culmination of the processes initiated during deformation, microstructure has profound effect on fracture behaviour of materials. From an engineering standpoint, the parameters used for characterising fracture behaviour are derived within the framework of fracture mechanics, and include -

- Pre-exponent and exponent of the Paris curve which are used to describe fatigue crack growth rates (FCGR)

- Fracture toughness in the linear-elastic and the elastic-plastic fracture mechanics regimes, based on stress intensity factor, *K*, and energy parameter *J*-integral respectively
- Tearing modulus, *T*, defined as the slope of the *J*-resistance curve for ductile fracture.

In recent years, considerable amount of interest has been generated in ductile fracture parameters such as blunting-line slope, *M*, and the related fractographic manifestation of stretch zone.

The above fracture mechanics parameters are known to be influenced by microstructure, as well as by environment, stress triaxiality, and geometry of engineering components. However, while other parameters can be quantified, or at least specified, unequivocally, the same is not often true for microstructure. Description of microstructure include grain size, preferred orientations of grains if any, degree and nature of banding, distribution of phases in microstructure, chemistry of different phases, size distribution of particles and precipitates present in microstructure, chemistry of particles and precipitates. Microstructural features can obtain various length scales from macroscopic (like band spacing) to sub-microscopic (for example precipitates which may be of a few nanometres in size). All of these features will influence on deformation and fracture behaviour of materials. Considering the complexities involved in defining microstructure, they are often indexed using mechanical properties like hardness or tensile strength, which reflect overall performance of a microstructure. These indices are further used to understand the influence of microstructure on fracture mechanics parameters.

The indirect appreciation of the effect of microstructure as described above, provides engineering leverage in comparative assessments, however they are somewhat empirical in nature. To elucidate: microstructure exhibiting the same hardness may contain completely different combination of phases that in totality provides same resistance to deformation by an indentor, but not same resistance to fracture. It is therefore imperative to develop a deeper understanding of the effect of microstructural constituents, on fracture behaviour and, to assimilate the effect of microstructure on fracture mechanics parameters.

Most investigations concerning the influence of heat treatment were confined to hardness, impact and tensile properties of HSLA–100 steels. However, these mechanical properties are insufficient to evaluate deformation behaviour of materials. Modern engineering design approach demands characterisation of material behaviour based on different fracture mechanics parameters. The influence of Cu precipitation and microstructural constituents on fatigue crack growth and fracture behaviour of Cu-strengthened HSLA steels has not been explored much. In the present investigation, efforts have been given to evaluate the effect of various microstructural constituents with a focus on Cu precipitation as a function of various ageing temperatures on different fracture mechanics parameters of HSLA–100 steel.

In this study, an attempt was made to assess evolution of microstructure by magnetic techniques, phase change by differential scanning calorimetry and correlate them with direct observation techniques. Variations in fatigue crack growth rate (FCGR), *J-R* curve, blunting-line slope and stretch zone width (SZW) for variation of microstructure in Cu-strengthened HSLA-100 steel has been investigated. The microstructural variation in the steel has been introduced through ageing at various temperatures after an initial quenching treatment. This has resulted in progressive tempering of the as-quenched martensitic matrix, accompanied by nanoscale precipitation of coherent Cu particles which gradually coarsen and loose coherency on over ageing. The high temperature precipitate population, which plays an important role in the process of ductile fracture, has been retained throughout the implementation of the scheme. Descriptions of various microstructures have been obtained through detailed scanning and transmission electron microscopy. These have been used to illustrate variation in mechanical properties and in fracture mechanics parameters obtained through standard tests.

Chapter 2.0

Literature Review

2.0

Literature Review

2.1 Introduction

HSLA steel can provide various strength–toughness combinations over a wide range of plate thickness for various structural applications. Microstructural engineering by thermo-mechanical controlled process (TMCP), along with accelerated controlled cooling (ACC) in this steel can optimise the desired microstructural constituents. The optimisation of different microstructural constituents can also be achieved through different processes like rolling and ageing, normalizing and ageing, quenching and ageing.

Literature review on HSLA steel in this chapter has revealed that investigation concerning the influence of ageing on microstructure and characterisation is not sufficient for modern engineering design approach, which includes fracture mechanics parameters. Section 2.1 is the introduction highlighted the need and content of this literature review. History of the development of HSLA steel has also been highlighted. Physical metallurgy of HSLA steel pertaining to the study forms the content of section 2.2 of this review. It reveals the important and relevance studies carried out in HSLA steels with a focus on role of alloying elements, thermo-mechanical and ageing treatment, strengthening mechanism, evolution of microstructures and mechanical properties. Section 2.3 contains the review of the changes in magnetic properties with structural modification. Magnetic techniques can be used for microstructure assessment for structural component by non-invasive way. In this section, possibility of using differential scanning calorimeter for the study of kinetics

of copper precipitation process has been reviewed. Section 2.4 and 2.5 are associated with fatigue crack growth and fracture behaviour of material. Other relevant literatures have been referred in results and discussion sections.

2.1.1 History of HSLA Steel

High strength steel was first developed in the 1960's for naval applications. Ferrite-pearlite steels had been used for many years for high strength structural applications. Medium carbon low alloy steels were also conventionally used for engineering structures in quenched and tempered condition. Advancements in high strength plate steels were stimulated by the demand for [1] (a) higher yield strength (YS), for greater load bearing capacity by thinner section (b) high resistance to brittle fracture as well as low impact transition temperature (c) a high degree of weldability. This led to the development of a new series of low carbon steels based on (1) low carbon content (2) adequate alloying elements to get desired transition temperature and (3) microstructural refinement by micro alloying and thermo mechanical processing. In these steels, strengthening mechanisms do not primarily depend on carbon. The strength of this category of steels is due to the dislocation sub-structure and solid solution strengthening [2]. The ultra low carbon bainitic (ULCB) steel is one category of such steel. A second category is copper containing HSLA steels, which are low-carbon, copper precipitation strengthened low alloy steels. These steels can provide various combinations of strength and toughness over a wide range of plate thickness. Research on HSLA steels has led to the development of HSLA-80 and HSLA-100 steel with many publications on the processing, microstructure and properties of these steels [3-29].

Carbon is an efficient and economic element for increasing strength in steels. However, its presence is associated with poor notch toughness. Weldability and weldment toughness are inversely related to the carbon equivalent (CE) in steels, and high fabrication costs may have to be incurred for steels due to stringent control requirements of welding procedures like preheat etc. Copper bearing HSLA steels have been developed to counter usual welding problems. The main objective of welding preheats is to minimise hydrogen related cracking in the hard martensitic heat affected zone (HAZ). The HAZ of very low carbon copper strengthened HSLA-80 steel is not significantly hardened due to dissolution

of copper and grain coarsening caused by heat of welding [24]. HAZ microstructure of such HSLA steels are thus less sensitive to hydrogen cracking and consequently achieve excellent weldability at low or without preheats. Hot cracking and cold cracking resistance of copper bearing HSLA-80 steels are superior to those of the conventional medium carbon high strength (HY-80 being a typical example of high strength carbon steel that was being used for naval structural applications) steels under similar conditions. Preheat or interpass temperature and electrode handling requirements for HSLA-80 applications are also less stringent than those for HY-80 welding. The relative fabricability of HSLA-80 in a shipyard production environment has demonstrated significant reduction of fabrication costs [25].

The US Navy first certified copper strengthened HSLA-80 steel for naval applications [7]. It is however unsuitable for complex structures, especially when subjected to complex dynamic loading. It is also not suitable for higher plate thickness applications due to limited hardenability. Later on, HSLA-100 steel with a higher YS, similar toughness and almost equivalent weldability is developed which is a modified version of the copper strengthened HSLA-80 steel, and is conceived as a replacement of high strength carbon steel (HY-100) for naval structural applications. This steel is also weldable without preheat and exceed strength and toughness of HY-100. It is not prone to HAZ softening because of increased hardenability. HSLA-100 steel has been found to be better in all aspects of structural performance in comparison to HY-100 steel. The copper containing HSLA-100 steel could be used in rolled and aged, normalized and aged, and quenched and aged conditions. It could provide higher strength and toughness over a wide range of plate thickness, in comparison to copper strengthened HSLA-80 steel.

2.2 Physical Metallurgy of HSLA Steel

2.2.1 Classification

The American Society for Metals (ASM) has classified the different varieties of high strength low alloy (HSLA) steels into four categories [30]:

(a) as hot-rolled C-Mn steel with minimum yield strength of 250-400 MPa (36-58 ksi)

(b) microalloyed HSLA steel with properties which result from low alloy additions and controlled hot rolling with minimum yield strength of 275-450 MPa (40-65 ksi)

(c) high strength structural carbon steels either in normalized or in quenched and tempered condition with minimum yield strength of 550-690 MPa (80-100 ksi)

(d) heat-treated structural low alloy steels quenched and tempered with minimum yield strength of 620-690 MPa (90-110 ksi)

Cu-strengthened HSLA steels belong to the last category of HSLA steels.

2.2.2 Role of Alloying Elements

Steel chemistry, and microalloying additions in particular, is an important factor that controls the microstructure of HSLA steels. Microalloying elements like niobium (Nb), titanium (Ti) and vanadium (V) play a major role in grain refinement and precipitation hardening which in turn alter the microstructure and mechanical properties of steels. The total amount of alloying elements is generally less than 10 wt%. Strength, toughness, hardenability, corrosion resistance and weldability properties can be improved by addition of alloying elements like nickel (Ni), copper (Cu), chromium (Cr), molybdenum (Mo) for specific applications. The main constituents of copper bearing HSLA steels are combinations of carbon (C), manganese (Mn), silicon (Si), sulphur (S), phosphorus (P), nitrogen (N), Nb, Ti, Cu, Ni, Cr, and Mo in different weight percentages. S and P remain in steel as primary impurities. The level of carbon is kept below 0.07 wt% to control HAZ hardness, toughness and cold cracking, whereas Cu addition up to 1.5 wt% raises yield and tensile strengths of the steel [31]. Cu imparts solid solution and precipitation strengthening in addition to resistance to corrosion. Cr, Ni and Mo improve toughness of the steel. The hardenability is improved by addition of Ni, Mo, Mn and corrosion resistance in marine environment is improved by addition of Cu, Mo and Cr [32-40]. Detailed discussions on the role of various alloying elements are available in literatures [30,41,42]. In this section, a brief discussion on the effect of alloying additions in HSLA steels is made.

Carbon is one of the cheapest element, forms interstitial solid solution of iron, conventionally used to increase the strength of steel. It forms carbides and carbonitrides by combining with other alloying element and have significant effect on mechanical

properties of steel. It increases hardenability, raises impact transition temperature, lowers weldability and resistance to corrosion. Weldability and toughness are deteriorated with higher amounts of carbon. The influence of carbon content and carbon equivalent [C.E.] on weldability of steel is shown in the Graville diagram in Fig. 2.1 [43]. In late seventies and early eighties, steels with low carbon content came into picture due to increasing demand for good weldability and formability along with high toughness at low temperatures for line pipe applications [44]. Further details of the influence of carbon content on steel microstructure are available in literature [45]. Bainitic microstructure appears in HSLA-100 steel in water quenched condition when carbon content is less than 0.02 wt% and lath martensite appears when carbon is kept above 0.03 wt%.

Manganese is one of the major alloying elements, which is added in different categories of steels in a wide range of wt%, depending upon cooling rate, thickness and strength of the products [46]. When Mn is added in steel, it acts as austenite stabilizer and carbide former. Mn prevents hot-shortness which results due to the presence of sulphur. The solute strengthening effect of Mn is also appreciable. Mn lowers the critical temperature and helps in formation of fine pearlite structure. It increases the hardenability markedly without a reduction in toughness. The ductile-brittle transition temperature (DBTT) of a steel decreases in the presence of manganese.

Silicon is known as a ferrite strengthener. It increases the tensile strength with a marginal loss in ductility and increases impact transition temperature [47]. *Nitrogen* beyond certain amount is not a desirable element in steel. *Aluminium* is added in steel as a nitrogen and oxygen scavenger. As Al forms fine aluminium nitride, it contributes in forming finer grained steel [48]. Micro alloying elements like *titanium*, *niobium* combines with nitrogen and form nitrides and/or carbonitrides. They act as grain refiner and precipitation hardener and increases the strength of the steel. Low nitrogen content in the range of 30-60 ppm is desirable to minimise loss of effective nitrogen [49]. *Sulphur* and *phosphorus* have detrimental effects on properties of steel. Sulphur causes hot shortness in steel, i.e., brittleness at high temperatures, whereas phosphorus drastically lowers the ductility and is said to induce cold shortness in steel. Sulphur and phosphorus should be less than 0.02 wt% for HSLA steels and it is necessary to have Mn of at least five times the weight of S to ensure the formation of MnS. Titanium has a high affinity for sulphur and

forms (TiMn)S and $Ti_4C_2S_2$ inclusions [50]. It is also very important to keep S low to minimise the loss of titanium.

Chromium, *nickel*, and *molybdenum* affect the hardenability of steel strongly, besides imparting solid solution strengthening. It is reported that Ni up to 3.5 wt% alone or in combination with Cr was initially used to develop HSLA steels [45,47,51]. Cr increases the yield strength and improves corrosion resistance property. The effect of Cr on transition temperature depends on the rolling condition [52]. Cr depresses the austenite transformation temperature and is used in place of Mo as hardenability agent. Mo is used for its effect on continuous cooling transformation characteristics [53]. The amount of Mo addition is dependent on the plate thickness and cooling rate [46]. An increase in Cu addition requires a higher amount of Ni addition. Ni prevents grain boundary segregation of Cu and thus reduces the chances of hot shortness [31,41].

Titanium, vanadium and *niobium* are added as microalloying elements in HSLA steel and act as grain refiners and precipitation hardeners. These microalloying elements increase strength, ductility and toughness of these steels. Ti, V and Nb are strong carbide and nitride forming elements even at very low concentrations [54]. These carbides and nitrides prevent austenite grain growth through pinning of grain boundaries during reheating, and retard recrystallisation during rolling of the steel. The basis of strengthening mechanism imparted by Ti, V and Nb is contributed by precipitation hardening, grain refinement, dislocation hardening and texture hardening [55]. It is observed that Nb affects grain refinement significantly with moderate precipitation hardening, whereas V imparts moderate strengthening with relatively weak grain refinement and Ti imparts strength through precipitation hardening and moderate grain refinement. Mishra et al. [10] studied the precipitation behaviour of HSLA-80 and HSLA-100 steels on quenching from different austenitising temperatures in the range of 950 to 1200^{o}C. They observed that Nb rich precipitates, that dissolved during reheating above 1150^{o}C, are present in the form of carbonitride in the steel. In another study, it was observed that TiN and TiCN formed during casting, remained undissolved during reheating at 1200^{o}C [56]. Xiaogong et al. observed that TiN and TiCN particles are formed in the liquid melt or during solidification [57]. Many factors are operative to control the size of TiN particle formed in the liquid state or during solidification. Ti/N ratio is one of them. It has been reported that the optimum Ti/N ratio is approximately 2 to 3.5 to produce fine TiN precipitate [58]. The

shape, size and distribution of precipitates are also important parameters, which regulate the mobility of dislocations and in turn the work hardening rate. Prikryl et al. has reported that the effective size range for precipitation hardening is approximately 5 to 20 nm [59]. Inter-particle spacing is very important for precipitation hardening. A model for the mechanism and kinetics of strain-induced precipitation of Nb(CN) in austenite has been developed by Dutta et al [60].

Copper draws attention as an alloying element because its effects in steel are manifold. Cu can be used as grain refiner, solid solution and precipitation strengthener [27]. Cu increases the strength in Cu-bearing steels through age hardening and it can increase the toughness as well as corrosion resistance. Therefore, research on Cu precipitation in steel has been essential for understanding as well as development of newer grades of Cu-containing HSLA steels. Precipitation of Cu in iron base systems has been studied by several investigators [61–76].

Russel and Brown [64] found a linear relationship between the yield strength increase and the square root of the Cu content in Fe-Cu binary alloys during thermal ageing experiment. The Russel-Brown modulus-hardening model explains hardening by treating Cu precipitates as soft spots in a harder iron matrix. In Cu bearing steels, Cu-rich clusters form first during ageing and they are coherent with the matrix and induce elastic strains within it. The cluster formation occurs by short-range diffusion of Cu in the solid solution formed on quenching. As the ageing temperature increases, the clusters disappear and intermediate phases form that are redistributed in the matrix. The hardness reaches a maximum value when the precipitates are semi-coherent and has a critical size [64].

However, Harry and Bacon [66] suggested a very different mechanism of hardening due to copper. They studied the dislocation-precipitate interaction and simulation of the strengthening effect originating from the core structure of the <111> screw dislocation in α-iron containing Cu precipitates. Their results indicate that the hardening observed in experiments is due to the effect of screw dislocation core on the BCC copper structure, which is a new precipitation strengthening mechanism, rather than elastic interaction.

Nakashima et al. [68] highlighted the strengthening mechanism due to Cu particles in terms of interaction between dislocation and Cu particles in aged Fe-Cu alloys. They observed that the dislocations moving during deformation cut Cu particles and pass through

them before the bowing angle of dislocation reaches $\pi/2$ when the size of Cu particles are less than 70 nm.

The maximum solubility of Cu in γ-iron is 2.1 wt% at 850^{o}C and solubility decreases with decreasing temperature [69]. Cu lowers the transformation temperature of martensite (M_S) or of bainite (B_S) upon quenching from austenite (γ) at 900^{o}C. Okada et al. reported that higher amount of Cu (>1.5 wt%) together with Mn lowers the transformation temperature of austenite in HSLA steels [70]. Cu precipitates retard recovery and recrystallisation of the quenched matrix. In another study, Garcia et al. [71] observed precipitation of ε-Cu particles in controlled rolled HSLA steel. Bhagat et al. [75] studied the ageing behaviour and precipitation of copper in HSLA steel by measurement of electrical resistivity continuously as a function of temperature and time which is an effective means of studying the kinetics of Cu precipitation in steel. The ageing kinetics of a low carbon Cu-bearing (1.86 wt%) steel has also been studied by Krishnadev et al. [76]. They observed that peak hardness and the time to reach the peak increases with decrease in ageing temperature.

2.2.3 Thermomechanical and Ageing Treatments

The heat treatment of Cu containing HSLA steels involves austenitisation or solution treatment followed by quenching and ageing. The processing technology of the steel comprises thermomechanical controlled processing (TMCP) followed by tempering or ageing [77,78,79]. TMCP optimises the grain size of the microstructure through controlled rolling (CR) at high temperature (>900^{o}C) followed by accelerated controlled cooling (ACC). The amount and nature of microalloying elements influence the controlled rolling. Controlled rolling can be divided into three stages [77,79]:

(a) deformation around 1080^{o}C; i.e. in austenite recrystallisation region where coarse austenite is refined through repeated recrystallisation due to continuous deformation

(b) deformation between 950^{o}C-870^{o}C in austenite non-recrystallisation region where formation of deformation bands in non-recrystallised austenite provides additional nucleation sites for transformation

(c) deformation in the two phase austenite-ferrite region.

One important stage in TMCP is accelerated cooling (ACC) or direct quenching (DQ). The grain growth is suppressed by rapid cooling from finish rolling temperature. Air cooling after accelerated cooling to room temperature provides self-ageing unlike direct quenching. The direct quenching results in formation of martensite and acicular ferrite or bainite at room temperature and ageing of the steel is necessary to obtain suitable combination of microstructure and properties. The accelerated cooling and DQ processing are illustrated schematically in Fig. 2.2. The cooling rate, plate thickness and steel composition together optimise the properties of these steels [77]. DQ and ACC control the austenite transformation and cooling begin at such a temperature that the third stage of TMCP can be omitted [80]. Controlled rolling followed by direct quenching or accelerated cooling leads to a uniform fine-grained structure [81].

A few literatures are available concerning the influence of ageing on mechanical properties of HSLA steel [7,78,82] and some results are shown in Fig. 2.3 to Fig. 2.5. The ageing behaviour of this steel can be divided into different stages [78]. Stage I is associated with exhibition of highest strength when ageing temperature is up to 450^{o}C. Stage II is associated with a continuous decrease in strength up to 640^{o}C. Stage III is associated with secondary hardening at 708^{o}C. Stage IV is again associated with a decrease in strength above 708^{o}C. The toughness of these steels increase significantly above ageing temperatures of 600^{o}C [7]. Several other investigators reported that the best combination of strength and toughness is obtained when the steel is aged between 620^{o}C-690^{o}C [22,78,83]. It is also reported that the ageing time to develop optimum toughness and mechanical properties may vary with plate thickness [78, 84-88].

2.2.4 Strengthening Mechanisms

The alloying elements and process variables play an important role in imparting high strength and toughness without impairing formability and weldability of HSLA steels [89]. Based on the work of Pickering [90] and Massip et al. [91], the following strengthening mechanisms are thought to contribute in enhancing mechanical properties of HSLA steels:

a) *Grain refinement* significantly increases the yield strength and toughness, and lowers impact transition temperature (ITT) of steels. The quantitative relationship between

yield strength and grain size has been established by Hall [92] and Petch [93]. The expression is as follows:

$$\sigma_{LYS} = \sigma_o + K.d^{-1/2} \quad \text{.... (2.1)}$$

where, σ_{LYS} is the lower yield stress; σ_o is the friction stress; K is a constant and d is the ferrite grain size.

Non-recrystallised austenite grains can produce fine grain ferrite where ferrite nucleation rate at the strained austenite grain boundaries are very high but growth rate is low due to space congestion [94]. Starting with a smaller austenite grain size, refinement of ferrite grain size can also be achieved [95].

b) *Solid solution strengthening* is dependent on the atomic size differences between solute and solvent. Potent interstitial solutes cannot be used for strengthening to a great extent due to their limited solubility. The influence of the solutes towards strengthening has been studied by Leslie [42]. At small concentrations, the solute has little effect on ductility and the variation in impact transition temperature [1].

c) *Precipitation strengthening* is responsible for decrease in impact transition temperature (ITT) [1]. It is also reported that a balance in precipitation strengthening and grain refinement increases the strength, toughness and ITT of HSLA steels [96]. The stress required to move dislocations in a slip plane has to be higher than the stress needed to generate dislocations from a source in precipitation strengthened alloys. Therefore, the yield strength associated with the stress required for dislocations to sweep out in the slip planes are large compared with dispersion strengthening.

d) *Dislocation strengthening* can effectively increase the yield stress of metals. A network of dislocations is produced due to deformation of metals below recrystallisation temperature. The interface of such networks restricts the movement of dislocations to a great extent. The following expression has been proposed by Baeley et al. [97] and Keh [98] for strengthening by dislocation interactions:

$$\sigma_d = \alpha \,.\, G \,.\, b \,.\, \rho^{1/2} \quad \text{.... (2.2)}$$

where α is a const., G is the shear modulus, b is the Burgers vector, ρ is the dislocation density.

Baker observed that dislocation density of a low C, Nb containing steel at room temperature is very high and depends on the finish rolling temperature [99]. He further observed that with lowering of finish rolling temperature, dislocation strengthening is enhanced. The limitation of dislocation strengthening is its influence towards the increase in ITT of the steel, despite the significant increase in strength.

e) *Substructural Strengthening* is another important strengthening mechanism for improving strength of metallic material. The ferrite and austenite grains are deformed and lead to an increase in dislocation density during thermomechanical treatment at a lower temperature between Ar_3 and Ar_1. Ferrite sub-grains can be formed by recovery if the temperature is favourable and sufficient. An additional increase in yield strength with a less detrimental effect on ITT can be imparted through the formation of ferrite subgrains.

The various strengthening mechanisms in microalloyed cold worked steel have been studied by Gawne et al. [100]. In their study, they observed that precipitation strengthening depends on volume fraction as well as direction of the precipitates, and not significantly on the composition of the precipitates. Manganese has a significant effect when combining with Nb and V in depressing austenite-ferrite transformation temperature, and increases the influence of controlled rolling. However, it acts as a weak solid solution strengthener. All the strengthening mechanisms that are often operative in HSLA steels can be combined and Baker has estimated the following relative contribution of individual mechanism [99]:

$$\sigma_{YS} = \sigma_o + \sigma_s + \sigma_p + \sigma_d + \sigma_t + K.d^{-1/2} + \sigma \qquad \ldots.(2.3)$$

in which σ_o is the lattice friction stress, σ_s is solid solution strengthening, σ_p is precipitation strengthening, σ_d is dislocation strengthening, σ_t is the strengthening due to texture, σ is strengthening due to subgrain effect, and $K.d^{-1/2}$ is strengthening due to grain refinement.

It may be noted that all strengthening mechanisms may not play a significant role in strengthening HSLA steels, and their relative contributions is an important consideration for optimisation of composition and processing parameters of the steel.

2.2.5 Microstructural Evolution

The alloying elements and thermo-mechanical processes control the microstructures of Cu-strengthened HSLA steels. It is from this premise that the concept of microstructural engineering arise. The formation of different phases in HSLA steel like acicular ferrite, bainitic-ferrite, martensite, martensite-austenite (MA) constituents depend on the mechanism of the transformation kinetics of austenite that in turn is dependent on several factors like transformation temperature, time, amount of deformation etc. Austenite, the initial phase by allotropic transformation, may produce a variety of microstructural constituents in solid-state reactions. Roberts et al. reported the kinetics of austenite transformation from ferrite/pearlite and ferrite/carbide aggregates [101]. They observed that cementite precipitates in ferrite matrix aid in the nucleation of austenite. The effect of composition and coherency of carbide on the rate of austenite nucleation and growth has also been reported [102].

The morphology of ferrite is dependent on the transformation temperature, austenite composition and hardenability. In most steels, proeutectoid ferrite is the initial transformation product, which forms over a wide range of temperature and composition [103]. The formation of polygonal ferrite in carbon-manganese steel contributes a small amount of transformation strain resulting in a lower quantity of dislocations [104]. It is also reported [105] that the volume fraction of fine-grained polygonal ferrite increases at the expense of acicular ferrite with an increase in the amount of deformation in non-recrystallisation regions [105]. Acicular ferrite forms on continuous cooling at a temperature range, which is slightly higher than the bainitic transformation temperature range [106,107]. The microstructure of acicular ferrite consists of non-equiaxed ferrite with a little amount of dispersed carbide. Acicular ferrite is intragranularly nucleated in bainite, so that it is possible to control these two morphologies by controlling the nucleation site [108]. Acicular ferrite contains considerable quantities of mobile dislocations and no carbide or occasional carbide precipitation is visible within the ferritic lath [109]. When austenite is transformed, another transformation product, such as pearlite may form by nucleation and growth. Conventional pearlite differs from pseudo-pearlite in respect of carbide arrangement as proposed by Lee et al. [104]. Bainite forms between the temperature range of martensite and ferrite-pearlite transformation. It consists of an aggregate of acicular ferrite and carbides. There are various forms of bainite like granular bainite,

inverse bainite, columnar bainite, pearlitic bainite, lower bainite and upper bainite described in details by Bhadeshia [108].

Martensite is formed by shear mode of transformation of austenite, which is an athermal reaction product. Its transformation is dependent on carbon partitioning in austenite [109]. The martensite reaction begins over a wide range of temperature from 500^{o}C to below room temperature depending on the austenite stabilizer concentration. The Kurdjumov-Sachs (K-S) orientation relationship persists between the austenite and martensite [110], i.e.

$\{111\}_{\gamma}$ // $\{110\}_{\alpha'}$ $\{111\}_{\gamma}$ habit plane

$<011>_{\gamma}$ // $<111>_{\alpha'}$, where α'- martensite

This relationship persists when the habit plane changes to {225}, but when new habit plane {259} appears, a new relationship is found to occur [111] that is given by

$\{111\}_{\gamma}$ // $\{110\}_{\alpha'}$ $\{259\}_{\gamma}$ habit plane

$<011>_{\gamma}$ // $<111>_{\alpha'}$, where α'- martensite

However, neither of these relationships is accurate and habit planes show a scatter of several degrees from the ideal orientation.

A variety of microstructural constituents like acicular and polygonal ferrite, lower and granular bainite, low carbon lath matensite, martensite-austenite (MA) constituents, retained austenite (RA), Cu-precipitates, carbides, carbonitrides and nitrides have been observed in HSLA steels by several investigators [11,112,113]. The presence of acicular ferrite in thin plate and polygonal ferrite in thicker plate has been reported [7,77,83,114,115]. HSLA-100 steel exhibits low carbon lath martensite in thin plate and granular bainite in thicker plate. The average prior austenite grain size of the steel after TMCP is found to be of ASTM No. 9 i.e. ~10 μm [7,77,83]. It is also reported that the size of Nb(CN) precipitates which form during hot rolling above 1000^{o}C varies with variation in the heat treatment [78,116].

Wenpu et al. in a TEM study showed that the microstructure of as quenched HSLA-100 steel consists of a lath matensite, acicular ferrite, retained austenite and twinned

martensite [117]. They observed microstructural changes like tempering of lath martensite and twinned martensite, recovery of acicular ferrite during ageing. Retained austenite was found to be stable and was not decomposed even on ageing at 650^{o}C for $1^{1}/_{2}$ hr. The precipitates observed in their study include ε-Cu, Mo_2C, $M_{23}C_6$, TiN and Nb(CN).

Besides copper precipitation, the formation of reverted austenite at prior martensite lath boundaries while ageing at 640^{o}C is also reported in HSLA steel [78]. The presence of fine copper precipitates has been reported by several investigators [21,78,116]. Cu-precipitates are generally found to be uniformly distributed throughout the matrix associated with dislocations. The size of Cu-precipitates has been observed to vary between 10nm and 30nm. The coarsening behaviour of copper precipitates has been studied by investigators [21,78]. The studies have revealed that clusters of Cu particle form initially at relatively lower temperatures and time of ageing. Spherical shaped coherent ε-Cu precipitates form at somewhat higher ageing temperatures and time. Rod like Cu-precipitates are formed due to coarsening on ageing and loose coherency faster on ageing at higher temperatures. The size variation of Cu-precipitates with ageing temperature in a repeat quenched and tempered (RQT) and direct quenched and tempered (DQT) Cu-strengthened HSLA steel is shown in the Fig. 2.6 [21].

2.2.6 Mechanical Properties

The mechanical properties of HSLA steels are dependent on the chemistry of materials, process parameters, rolling condition, ageing or heat-treated condition etc that influences the resultant microstructure. Some reports are available as shown in Fig. 2.3 to Fig. 2.5 that shows the variation of hardness, yield strength, notch toughness with variation in tempering temperature of HSLA-100 steel [7]. With reference to figures, it may be noticed that maximum hardness and maximum yield strength were achieved on ageing at around 450^{o}C, which is due to the formation of Cu-rich clusters. Above 500^{o}C, a continuous decrease in strength and hardness was observed. The transformation of reverted austenite to martensite around 650^{o}C while ageing and appearance of a secondary peak has also been reported [7]. On further ageing the steel above 700^{o}C, the material was softened due to the formation of bainitic microstructure. The reverted austenite has a strong influence on the mechanical properties of HSLA-100 steels. Fig. 2.7 shows a schematic illustration of the variation of

yield strength as a function of the formation of microstructural constituents of HSLA-100 steel with change in ageing temperature. Reports are available on the comparison of mechanical properties of Cu-strengthened HSLA-steel with those of other steels of similar strength [77,88].

2.3 Indirect Assessment of Microstructural Evolution

2.3.1 Magnetic Techniques

Ferromagnetic material consists of sub-microscopic regions known as domains within which the majority of magnetic moments are aligned in one direction. In a demagnetised state, the domains are oriented randomly, so that the net magnetisation of the materials is zero (Fig. 2.8a). The region between the domains where the moments change their directions is called the domain wall and this is shown schematically in Fig. 2.8b. The change in orientation is spread over several hundred atom layers, which is called the domain wall width. Every domain is magnetised to saturation but unless a majority of them is aligned in particular direction, the vector sum of all domains will be zero and the material is considered macroscopically demagnetised. When a magnetic field is applied, domains are favourably aligned with the field, and tend to grow by domain wall movement at the expense of unfavourably aligned domains. The amount of growth or the distance that a domain wall travels depends on the strength and the direction of applied magnetic field, microstructure, composition and the stress state of the material. Domain wall can be classified into 180^o walls, in which the spins rotate by 180^o from one domain to another, and 90^o walls, in which the domain rotates by 90^o upon application of the magnetic field.

When a ferromagnetic material is subjected to a cyclic magnetic field of very low amplitude, reversible domain wall motion takes place and the material returns to its initial state after the magnetic field is withdrawn. Magnetic hysteresis loops (MHL) are formed when the amplitude of the applied cyclic field crosses a critical value at which the domain wall moves irreversibly. Fig. 2.9 shows the various magnetic hysteresis loop parameters when the test material is subjected to a high amplitude of cyclic magnetic field so that all the domains are oriented along the field direction, and the material is known to reach its saturation (B_S) level. MHL parameters represent the bulk properties of the test material. On

the microscopic scale, the hysteresis loop is not found to be a smooth function of magnetic induction (B) and field (H). The magnetic induction curve consists of discontinuous changes although the field is continuous. Particularly near the coercive point of the material, the magnetic induction curve shows a structure composed of many individual steps, which are caused by the sudden jumping of domain walls from one position to another during the process of magnetisation. These small steps, which are irreversible changes in magnetisation, are known as magnetic Barkhausen emissions (MBE). The irreversible motions of 180^{o} domains are mainly responsible for MBE signals. Fig. 2.10 shows how one MBE burst is created for a magnetising half cycle. MBE signal can be quantified in terms of peak amplitude, rms voltage, number of pulse counts, pulse height distribution etc. Barkhausen emissions are electromagnetic signal of radio frequency range and hence, due to eddy current limitation, MBE presents the surface properties of materials.

Most of the materials used for structural purposes in pipeline, railroads, and bridges are made of steel, which is ferromagnetic. It is found that magnetic parameters like coercivity decreases with an increase in tensile stress and grain size [118,119]. A good correlation has been found to exist between hardness and magnetic properties [120]. A considerable change in magnetic properties is also found during plastic or elastic deformation [121]. In view of these observed changes in magnetic properties with the structural modification, attempts are now being made to utilise the inherent ferromagnetic properties of steel for evaluation of integrity of in-service components. Different magnetic NDE techniques was reviewed by Jiles [122] and out of all the available techniques, *magnetic hysteresis loop* (MHL) and *magnetic Barkhausen emissions* (MBE) are found to be very promising as non-destructive testing (NDT) tools.

MHL parameters may be divided into two categories. These are structure sensitive properties, such as coercivity, permeability, remanence and hysteresis loss, and structure insensitive properties, such as saturation induction, saturation magnetostriction and Curie temperature. The variation of some structure sensitive properties of AISI 1000 series carbon steel with two different microstructures is shown in Table-2.1 [123].

MBE are also found to be sensitive to the microstructure of structural materials [124]. Coercivity is normally found to be an inverse function of grain size [125]. In

addition to the inverse relationship, a Hall-Petch type relationship has also been proposed [126].

$$Hc = K_1 + K_2 d^{-1/2} \quad \ldots. (2.4)$$

where, K_1, K_2 is constant and d is the grain size. This equation indicates analogous behaviour of domain walls and dislocations at pinning points [126,127]. As grain boundary is the source of nucleating sites for irreversible magnetic flux motion, which corresponds to Barkhausen jumps, MBE activity is also influenced by the grain size. Barkhausen activity has been modelled in ferritic steel by the following equation [128].

$$V_{rms} = C_g d_g^{1/2} \quad \ldots. (2.5)$$

where, C_g is a constant and d_g is ferrite grain size.

Thermal ageing of ferritic steel may occur in components operating at higher temperatures, and dislocation density, size and distribution of laths/grains and second phase precipitates may vary in a systematic manner due to thermal ageing. Using MBE parameters, a two stage magnetisation process has been proposed in sufficiently tempered microstructure, considering the grain boundaries and the carbide precipitates as the two major types of obstacles to the domain wall movement, to characterise such thermally aged microstructures [129]. Studies have been carried out in an annealed and a thermally aged 0.3% carbon steel to establish the effect of lamellar and spheroidised cementite structures on MBE behaviour [130]. The effect of microstructural change during isothermal heat treatment on structure sensitive magnetic properties has been investigated for low alloy steel [131,132]. It was observed that magnetic permeability increased while coercive force and Vickers hardness decreased with increased ageing time. During isothermal heat-treatment, $M_{23}C_6$ and $(Cr_{2.5}Fe_{4.3}Mo_{0.1})C_3$ carbides were found at grain boundaries. These carbides were formed by C, Cr, Mo and Mn which migrated from the matrix to the grain boundary. The decrease of C in matrix resulted in decrease of Vickers hardness and coercive force and in the increase in permeability. The correlation between mechanical and magnetic properties indicates that hardness and microstructural changes could well be evaluated in a non-destructive fashion by measuring permeability or coercive force.

2.3.2 Differential Scanning Calorimetric Study

The theory of operation of differential scanning calorimeter is based on principle in which energy absorbed or evolved by the sample is compensated by adding or subtracting an equivalent amount of electrical energy to a heater located in the sample holder. Platinum resistance heaters and thermometers are used in the DSC to accomplish the temperature and energy measurements. The continuous and automatic adjustment of heater power is necessary to keep the sample holder temperature identical to that of the reference holder provides a varying electrical signal equivalent to the varying thermal behaviour of the sample. This measurement is made directly in energy units and providing true electrical energy measurement of peak areas. DSC measures time, temperature, heat flow and by integration of the heat flow, enthalpy. The most common DSC application is the precise measurement of transition temperature. DSC provides the information quickly and easily on a minimum amount of sample. In DSC specific heat-temperature (c_p-T) curves can be rapidly determined using only milligram quantities of solids or liquids over a temperature range of 25^{o}C-750^{o}C. If a particular thermal event (phase change, annealing, chemical reaction, etc.) is encountered, the calorimeter can be thought of as treating it as unusual c_p requirement so that by integration, overall enthalpy changes can be found and these in turn yield heats of fusion, transition, reaction etc.

DSC is capable of distinguishing random temperature variations and those are caused by actual phase evolution. The absorption energy for the phase transformation is generally calculated by using Kissinger Plot [133].

2.4 Fracture Behaviour

Fracture of materials is an inevitable consequence of continued stress and deformation of materials. Fracture behaviour of materials can be studied and quantified using various phenomenological aspects. In recent times, the area of fracture mechanics has been especially developed for understanding fracture mechanisms and characterisaton of fracture resistance. Fracture mechanics has been extensively used for this purpose in this work

The following fracture mechanics parameters are generally used for characterising fracture behaviour of material:

(i) fracture toughness in the linear-elastic and elastic-plastic fracture mechanics regime, based on the stress intensity factor, K, and the energy parameter J-integral respectively,

(ii) the pre-exponent and exponent of the Paris curve that is used to describe fatigue crack growth rates (FCGR),

(iii) the tearing modulus, T, defined as the slope of the J-resistance curve for ductile fracture.

The blunting-line slope, B, and the related fractographic manifestation of the stretch zone have also drawn considerable interest as ductile fracture parameters. These parameters are also influenced through a variation of microstructure.

The fracture mechanics parameters stated above are known to be influenced by microstructure, environment, stress triaxiality and the geometry of components. The parameters other than the microstructure can be quantified, or specified, unequivocally. Considering the complexities involved in defining microstructures, they are often indexed using basic mechanical properties like hardness or tensile strength that reflect the overall performance of a microstructure. The indirect appreciation of the effect of microstructure provides an engineering leverage in comparative assessments. However, they are somewhat empirical in nature.

Fracture mechanics parameters, like the ones listed above, essentially characterise the propensity of a crack to extend. These parameters represent crack extension force or energy, and their critical values are known as materials properties. The procedure for making an estimate of crack driving force lies in the domain of linear elastic fracture mechanics (LEFM) in the case of materials behaving “globally” in a linear elastic manner. The elastic–plastic fracture mechanics (EPFM) is adopted where extensive plastic deformation is experienced prior to fracture. For Cu-strengthened HSLA-100 steel, the EPFM regime is applicable for many of the microstructural conditions that are being studied in this investigation.

Principle of LEFM is based on the distribution of stress ahead of a crack in a body under load. The amplitude of the stress distribution is characterised by the stress intensity

factor K that has been shown as a characteristic parameter representing the driving force for existing cracks to propagate. The solution of the stress field in front of a crack using linear elasticity can be written as:

$$\sigma_{ij} = \frac{K}{\sqrt{(2\pi r)}} f_{ij}(\theta) \quad \text{…. (2.6)}$$

where, (r,θ) represent polar coordinates around the crack tip and f_{ij} are characteristic functions of θ.

The elastic stress field solution indicates the presence of a stress singularity at the crack tip. However most materials exhibit a yield stress above which they deform plastically, and therefore there exists a region around the crack tip, known as the plastic zone (PZ), within which the material is yielded plastically. As long as the size of the PZ is insignificantly small in comparison to significant dimensions of the crack geometry, the employment of LEFM remains valid. Fracture conditions are controlled by EPFM in materials where the size of PZ is relatively large. EPFM often uses the concept of non-linear elasticity to obtain solutions for equivalent plastic problems. EPFM is based on a detailed understanding of crack tip plasticity. There are three established procedures for obtaining characteristic fracture parameter under EPFM applicability: those based on (i) crack tip opening displacement (CTOD) (ii) *J*-integral and (iii) *R*-curve concept.

A larger plastic zone (PZ) means that the displacement field is higher than that calculated by elasticity theory. The presence of a plastic zone makes a crack to behave like a crack that is longer than its original size and lowers the stiffness of the component the crack is contained in. Irwin [134] first estimated such plastic zones and observed this phenomenon. Of late, a series of refined calculations have been developed for predicting the shape and size of plastic zones associated with crack tips [135-141]. The size and shape of a plastic zone depends on (i) the yield criterion, (ii) the mode of loading (with respect to the crack orientation) and (iii) the strain hardening behaviour of the material. Etching techniques can reveal plastic zones perhaps in a better and more convincing way than theoretical descriptions of PZ [142,143].

The concept of crack tip opening displacement (CTOD) as a fracture criterion was proposed by Wells [144] and was improved upon by other investigators [145,146]. Based on this, Dugdale [135] formulation for plastic zone size can be written as

$$\frac{a}{C} = \cos\left(\frac{\pi\sigma}{2\sigma_Y}\right) \quad \text{....(2.7)}$$

where, a is the half crack length, and $C = a+d$, where, d being the plastic zone length at the crack tip. The expression for CTOD (δ) then becomes [144-146]

$$\delta = \frac{8a}{\pi\sigma_Y}\log\left(\sec\frac{\pi\sigma}{2\sigma_Y}\right) \quad \text{.... (2.8)}$$

After simplification the equation can be written as for $\sigma << \sigma_Y$ as,

$$\delta = \frac{K^2}{E\sigma_Y} \quad \text{.... (2.9)}$$

The equation (2.9) can be written for constrained yielding as,

$$\delta = \frac{K^2}{m_1 E\sigma_Y} \quad \text{.... (2.10)}$$

where, m_1 is a constant and it value lies between 1 and 2.

As equations (2.9) and (2.10) indicate $K \rightarrow K_C$ and $\delta \rightarrow \delta_C$, therefore the critical value of CTOD (δ_C) is a material property which depends on the microstructure of material, temperature and loading rate used for testing. If, the size of plastic zone is significantly small, then $K \rightarrow K_{1C}$ and $\delta \rightarrow \delta_{1C}$. Hence, CTOD is applicable for both LEFM and EPFM regimes. Among the various procedures like optical method, extraction replica, paddle device, infiltration technique, clip gauge technique [147-154] for determining CTOD, the method based on the work of Dawes [155] is popular and can be written as,

$$CTOD = \frac{K^2}{2E'\sigma_Y} + \frac{V_p}{1+2.5\left(\frac{a+z}{W-a}\right)} \quad \text{.... (2.11)}$$

where, V_p is the plastic component of clip gauge displacement measured at a distance z from the specimen surface or loading line, and $E' = E/(1-\nu^2)$.

The elastic-plastic stress field near the crack tip is characterised by the *J-integral* in the same way as *K* describes the crack tip elastic stress field. Several investigators provide a description of the crack tip mechanical environment for the elastic plastic situation [140,156-159]. It has been shown [156] that the *J*-integral is the change in potential energy for a virtual crack extension of ∂a and *J* can be simply defined as

$$J = -\frac{\partial V}{\partial a} \qquad \text{…. (2.12)}$$

where, *V* is the potential energy.

The potential energy term is no longer available for crack propagation as a portion of energy is dissipated in incremental plastic deformation. There has no physical meaning of *J* as energy release rate given by equation (2.12) is lost in real materials [160,161]. For an elastic plastic situation equation (2.12) is written as [156]-

$$J = -\frac{1}{B}\frac{\partial U}{\partial a} \qquad \text{…. (2.13)}$$

where, *U* is the strain energy, *B* is the thickness of the component and $\partial U/\partial a$ is elastic and plastic work done per unit crack growth.

Equation (2.13) does not rely on energy balance but depends on path independence and the degree to which the value of *J* is related to stress or strain singularity near the crack tip. The value of *J* as a dissipative energy rate based on elastic plastic work done from the load line displacement curve can be determined by [162-164]-

$$J = \frac{\eta U}{B(W-a)} \qquad \text{…. (2.14)}$$

where, *U* is the total work done depends on the configuration and extent of plastic flow, η is 2 have been taken for deep notched bend specimen [163,165] and equation (2.14) can be expanded as [161,165,166]

$$J = \frac{\eta_e U_e}{B(W-a)} + \frac{\eta_p U_p}{B(W-a)} = \frac{K^2}{E'} + \frac{\eta_p U_p}{B(W-a)} \qquad \text{…. (2.15)}$$

where, U_e and U_p are the elastic and plastic parts of the area under load-displacement plot of *J*-integral test as shown in Fig. 2.11. The η_e factor simplifies the determination of *J* and allow the stability of the growth. η_e *and* η_p factors can be computed as given by the investigators [167,168].

Dawes [169] proposed the following relationship to obtain *J* from the load-COD diagram –

$$J = \frac{K^2}{E'} + \frac{P_1+P_2}{B(W-a)}\left(\frac{WV_p}{a+z+r_p(W-a)}\right) \quad \text{.... (2.16)}$$

where, P_1 and P_2 are defined in Fig. 2.11, V_p is the plastic component of clip gauge displacement, r_p is the plastic rotational factor and r_p is 0.4, when $a/W > 0.45$ and r_p is 0.45, when $a/W < 0.45$.

The standard method for determining *J*-integral has been given in ASTM-E-813 [164]. J_C and $J_{1C,}$ represent characteristic failure criteria in situations where fracture is preceded by substantial amount of yielding. J_C and J_{1C} also depend on temperature, strain rate, microstructure like K_C and K_{1C}. The dimensional requirement for the measurement of J_{1C} is given by [163]-

$$a, B \text{ and } (W-a) \geq 25\left(\frac{J_{1C}}{\sigma_o}\right) \quad \text{.... (2.17)}$$

where, σ_o is the flow stress.

The above dimensional requirement is much smaller than $K_{1C.}$

R-curve analysis is an alternative technique for determining the fracture resistance of a material in the EPFM domain in addition to *J*-integral and CTOD criteria. The *R*-curve technique is based on an extension of LEFM concept to the EPFM domain. There is a continuous balance between the released and the consumed energy during slow crack growth as proposed by Irwin and the failure occurs when the rate of the change in the elastic energy release rate, $\partial G/\partial a$, equals the rate of change in the material resistance to such crack growth, $\partial R/\partial a$ [170]. It is possible to determine G_C or $K_{C,}$ by knowing the *R*-

curve of the material and using the correct stress and crack length dependence of G for a given specimen configuration.

The fracture behaviour of a material including crack initiation and propagation can be described by R-curve. This method provided an alternative way to analyze fracture behaviour of an elastic–plastic material where determination of J_{1C} is not possible. The ASTM [171] procedure for J-R analysis divides J-resistance of a material into elastic and plastic components:

$$J_R = J_C + J_{p1} \quad \text{.... (2.18)}$$

the elastic component is-

$$Jc = \frac{K^2\left(1-\nu^2\right)}{E} \quad \text{.... (2.19)}$$

where, K is constant, computed in a similar fashion to the stress intensity factor calculation procedure described in the ASTM standard E-399 [172]. The plastic component of J is-

$$J_{p1} = \frac{2A}{Bb} \quad \text{.... (2.20)}$$

[For triple point bend (TPB) specimen.]

where, A is the area under load-displacement curve during the J-integral test.

The construction of J-R and δ-R curves is possible by using multiple or single specimen technique [164,171,173]. The construction of R-curve or evaluation of δ_{1C} and J_{1C} requires measurement of crack growth during loading.

The construction of J-R or δ-R curve requires the continuous measurement of the growth of ductile crack extension from crack tip. Various techniques based on optical, compliance and electrical potential drop measurements can be adopted for monitoring of the crack length. The optical measurement technique of crack length measurements in multiple specimens is recommended by ASTM E-813 [164]. But this technique may increase the scatter in data points for J_{1C} determination [174]. Therefore, single specimen technique is recommended for evaluating J_{1C} or δ_{1C} or constructing R-curve to establish a confident lower bound toughness. The compliance method is often used for crack length

calculation using crack opening displacements measured at crack mouth. Investigators [175,176] proposed the relationship between the crack length and normalised compliance U that can be written as-

$$\frac{a}{W} = C_0 + C_1 U + C_2 U^2 + C_3 U^3 + C_4 U^4 + C_5 U^5 \qquad \text{…. (2.21)}$$

where, C_0 to C_5 are the coefficients experimentally or numerically derived and U is given as-

$$U = \frac{1}{\sqrt{\frac{E'BV}{P}+1}} \qquad \text{…. (2.22)}$$

where, E' is the effective modulus, being equal to the Young's modulus E in plane stress and $E/(1-\nu^2)$ in plane strain, ν is Poisson's ratio, B is specimen thickness and V/P is measured compliance.

The crack growth measurements by electrical potential drop estimations are used when the displacement measurement for compliance calculations is difficult [177-179]. In this technique, the crack length causes perturbations in the equi-potential lines surrounding the crack and the potential drop is measured across the crack mouth that changes, as the crack grows in a constant current.

The critical conditions for fracture can be described by parameters like *tearing modulus* other than conventional fracture toughness parameters like CTOD, J and R-curve [180-181]. The tearing modulus (T_J) as described by Paris et al. [180].

$$T_J = \frac{dJ}{da}\frac{E}{\sigma_Y^2} \qquad \text{…. (2.23)}$$

where, dJ/da is the slope of the J-Δa curve in stable crack growth domain.

An equivalent measurement of the material's resistance to crack growth in terms of equivalent to that of tearing modulus based on crack tip opening angle (CTOA) can be written as [182] –

$$T_\partial = \frac{Ed\partial}{\sigma_Y da} \qquad \text{…. (2.24)}$$

To understand the relationship between the crack initiation and crack growth toughness parameters, several attempts have been made based on the tearing modulus [181,183,184].

2.5 Fatigue Behaviour

There are many literatures available on fatigue behaviour of materials. Nevertheless, fatigue is still most common cause of the failure of any components. Conventionally the design against fatigue is based on tests and the results of the tests are presented as S-N curves. These curves relate cyclic stress to number of cycles to failure. However, this conventional approach for design against fatigue is inadequate and it cannot differentiate between the initiation and propagation of crack growth, which accounts for the majority of failure. The conventional approach does not provide a link between the micromechanism of fatigue crack propagation and the fatigue failure of materials. Therefore, fracture mechanics is used as a tool for quantifying the effect of fatigue and design against fatigue failures. Paris et al. propose the fracture mechanics parameters for characterising fatigue are- stress intensity factor range, reversed plastic zone and Paris plot [185].

The *stress intensity factor* (K) is a function of the applied force and the geometry of the cracked body and the crack driving force in fatigue can be represented in terms of the stress intensity factor. The local stress at the crack tip is described by the stress intensity factor. In a fatigue situation, a stress intensity range ΔK which is comparable to a cyclic stress range $\Delta\sigma$, is used and given by-

$$\Delta K = K_{max} - K_{min} \quad \text{…. (2.25)}$$

where, K_{max} and K_{min} are stress intensity factors associated with the maxima and minima of the loading cycles, σ_{max} and σ_{min} respectively.

In order to describe the stress–state fully, the R-ratio is given by-

$$R = \frac{\sigma_{min}}{\sigma_{max}} = \frac{K_{min}}{K_{max}} \quad \text{…. (2.26)}$$

The *R*-ratio indicates the mean stress level that is represented by-

$$K_{mean} = \frac{K_{\max} + K_{\min}}{2} \quad \text{…. (2.27)}$$

ΔK, K_{max}, K_{min}, K_{mean} and R are inter-related through the above equations and any two can be used to describe a fatigue loading situation.

The plastic zone at crack tip consists of a *reversed plastic zone (RPZ)* embedded in a larger monotonic plastic zone due to cyclic nature of loading in fatigue. The monotonic zone results from the maximum stress σ_{max} in loading cycle and can be written as-

$$r_p = \alpha\left(\frac{K_{\max}}{\sigma_Y}\right)^2 \quad \text{…. (2.28)}$$

where, α is a constant.

The RPZ size can be estimated and can be written as-

$$r_{rpz} = \alpha\left(\frac{\Delta K}{2\sigma_Y}\right)^2 \quad \text{…. (2.29)}$$

Knott has explained the use of $2\sigma_Y$ in calculating RPZ. σ_Y must be replaced by the cyclic yield strength in equations (2.28 and 2.29) in order to model the real cyclic situation [186].

Crack initiation and crack propagation are responsible for fatigue failure. Quantification of fatigue crack propagation is necessary as it plays an important role in controlling fatigue failures. Crack growth laws for this are available [185,187-192]. The most widely used crack growth was proposed by Paris et al. based on fracture mechanics [185]. This law is popularly known as *Paris Law* and the equation is given by-

$$\frac{da}{dN} = C\Delta K^m \quad \text{…. (2.30)}$$

where, $m = 4$ (empirically found), C is a constant (independent of material).

There are number of experimental investigations [193-196] to provide evidence to prove the value of *m*. However, Ritchie and Knott indicate that the exponent *m* can assume a number of values [197].

Figure 2.12 shows a sigmoidal curve obtained when the crack growth rate (*da/dN*) is plotted against ΔK for a full range of growth rates as suggested by Paris et al. [185]. This plot can be divided into three regions as shown in the Fig. 2.12. The Paris equation (eqn. 2.30) is applicable to region *B* only, which is linear on logarithmic plot. The crack growth rates in *B* region are less sensitive to limited variations in frequency, environment, mean stress and microstructure. However, crack growth rates are very sensitive to the variations of above factors in region *C* and in the threshold region *A*, where as crack extension in region *C* is aided by non-fatigue fracture mechanisms [198].

Fatigue crack propagation is affected by various factors such as *R*-ratio, the frequency of test, environment, microstructure, materials properties etc. as described briefly below.

The effect of *R-ratio* or mean stress on fatigue crack growth rate (FCGR) arises from two sources. Higher *R*-ratio means higher mean stress, which results in attainment of a higher K_{max} for a given ΔK, where the growth rate is dependent on K_{max}. This will result in a higher growth rate. Secondly, a higher mean stress can result in reduction of crack closure stress. This increases the driving force at the crack tip, which ultimately increases the growth rate. The empirical modelling has been done on the effect of *R*-ratio on FCGR [199] and can be written as-

$$\frac{da}{dN} = \frac{C\Delta K^m}{(1-R)K_c - \Delta K} \quad \text{.... (2.31)}$$

where, K_c is the cyclic fracture toughness.

The ASTM task group E24.04.04 [200] has recommended a standard procedure for determination of the stress intensity factor, K_{C1} at which the crack faces come into contact. It has been shown in a investigation [201] that the use of ΔK_{eff} (where, $\Delta K_{eff} = K_{max} - K_{C1}$), instead of ΔK results in convergence of plots of experimental data by varying *R*-ratio and the effect of mean stress can be correlated with closure.

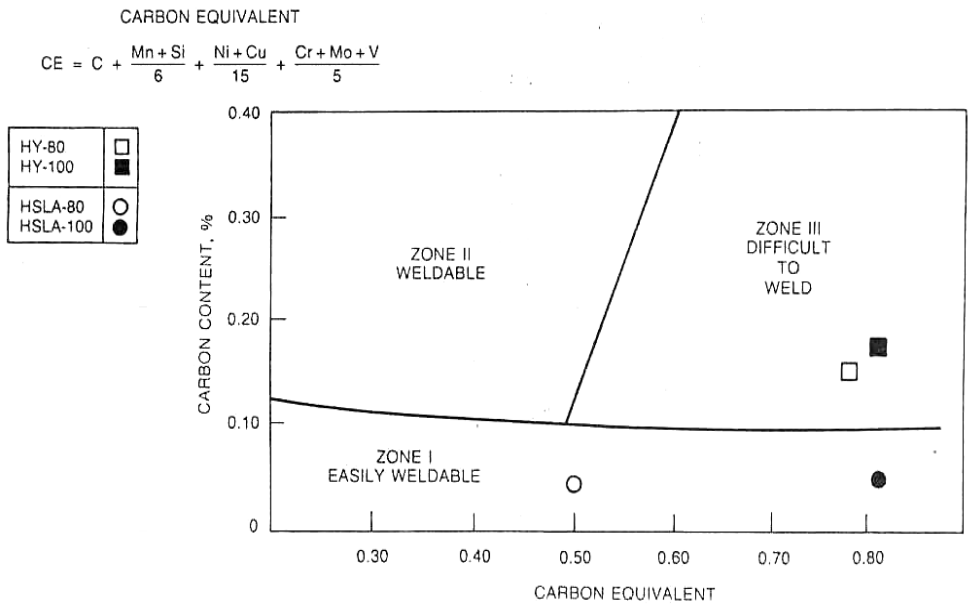

Figure 2.1: Graville diagram showing the influence of carbon level and carbon equivalent [C.E.] on weldability of different grades of steel [43].

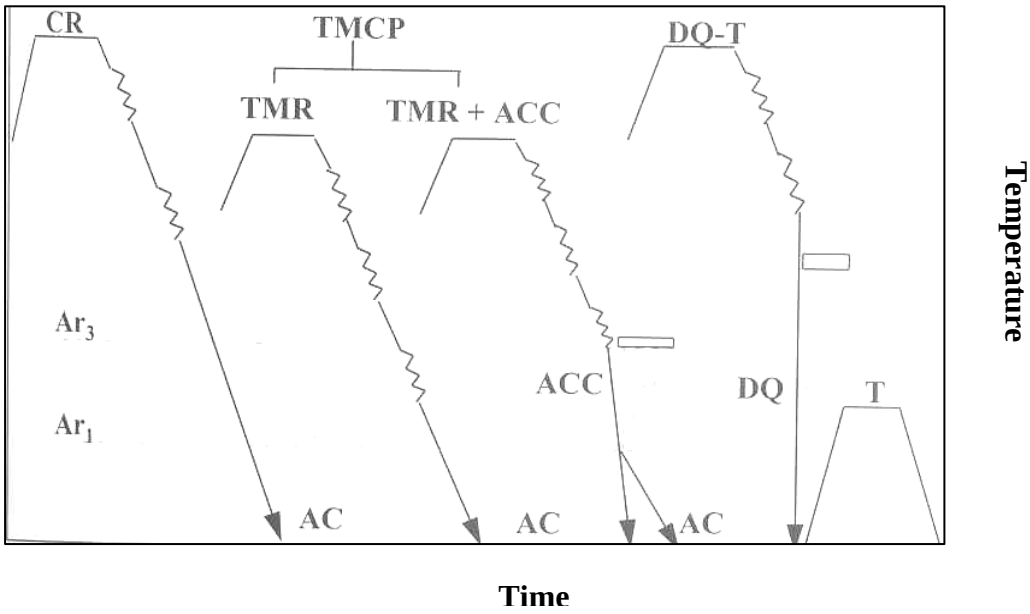

CR: Controlled Rolling; TMR: Thermo-Mechanical Rolling; ACC: Accelerated Cooling; DQ: Direct Quenching; T: Tempering; AC: Air Cooling

Figure 2.2: Schematic representation of different thermo mechanical and heat treatment processing of HSLA steel [77].

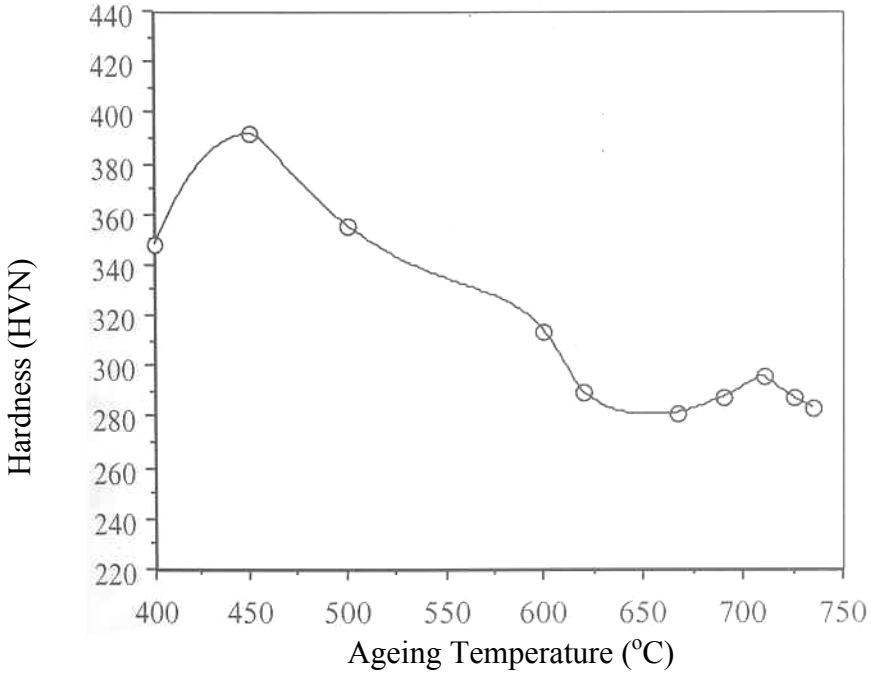

Figure 2.3: Variation of hardness in HSLA steel with ageing temperature [7].

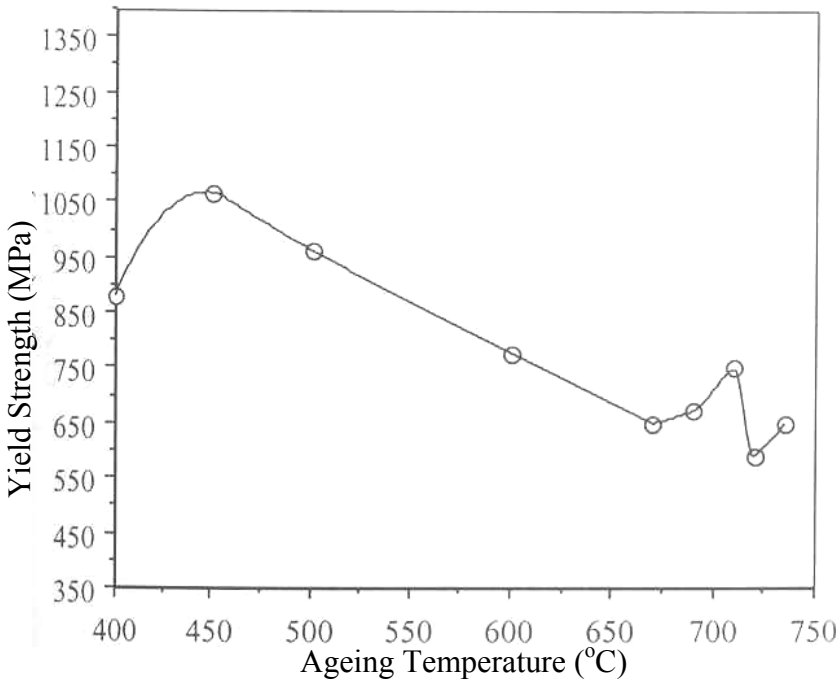

Figure 2.4: Variation of yield strength of HSLA steel with ageing temperature [7].

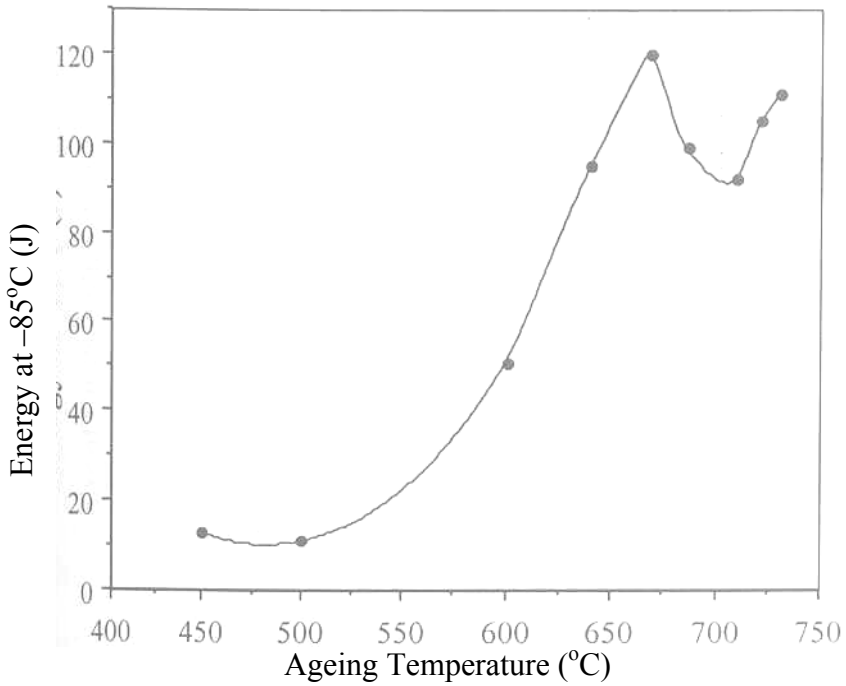

Figure 2.5: Variation of impact toughness at –85°Cwith ageing temperature [7].

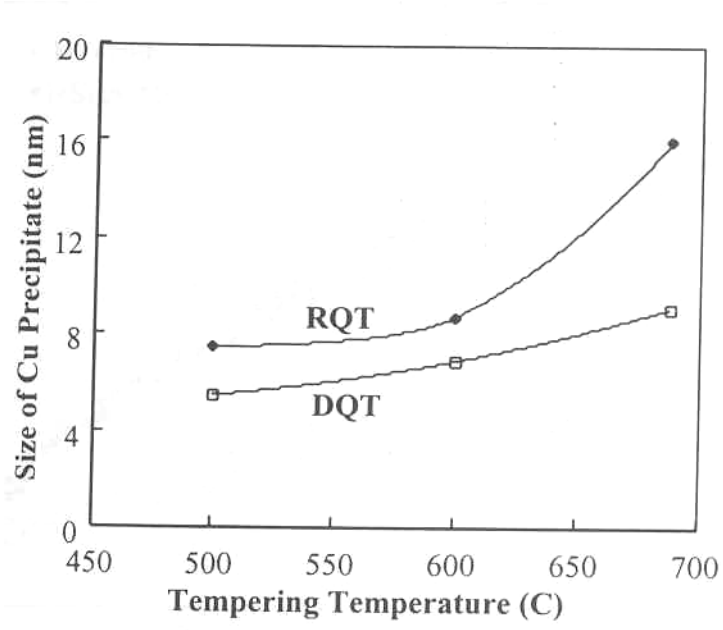

Figure 2.6: The size variation of Cu-precipitates with ageing temperature in a repeat quench and tempered (RQT) and direct quench and tempered (DQT) Cu-strengthened HSLA steel [21].

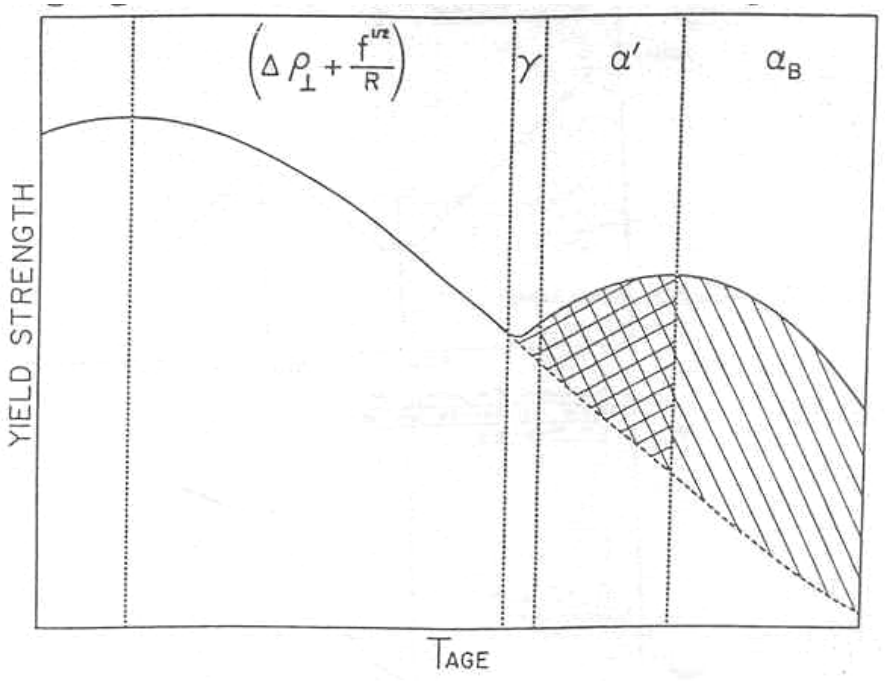

Figure 2.7: Schematic illustration of variation of yield strength as a function of formation of microstructural constituents with ageing temperature [7].

Table-2.1: Magnetic parameters for different AISI 1000 series carbon steel [123]

Sample with AISI Designation	Normalized lamellar pearlite microstructure			Spheroidized microstructure		
	Hc (A/m)	Br (T)	μ_{in}	Hc (A/m)	Br (T)	μ_{In}
1020	517	0.95	150	517	1.31	275
1045	835	0.88	100	597	1.34	200
1080	875	0.80	95	716	1.05	185
1095	875	0.88	100	637	1.20	170

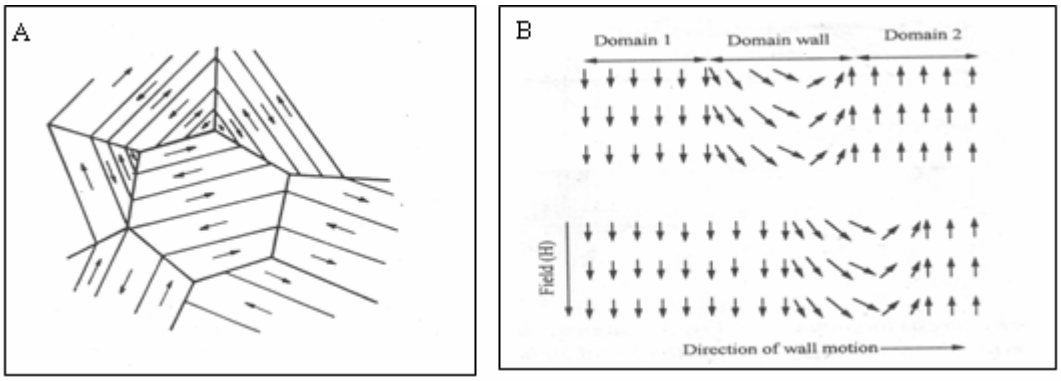

Figure 2.8: (a) Schematic representation of magnetic domain in polycrystalline materials like steel (b) the movement of the domain wall under applied magnetic field

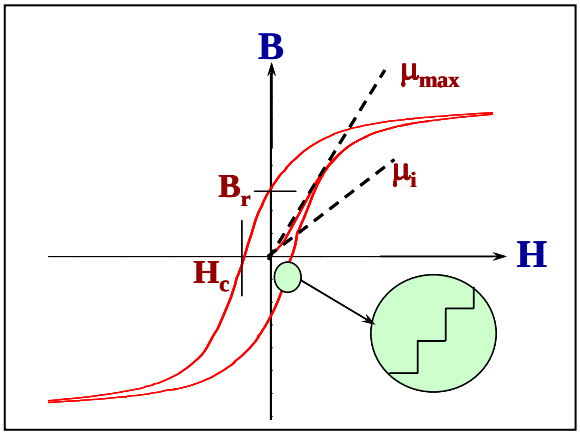

Figure 2.9: Magnetic hysteresis loop showing important properties, Remanence (Br), Coercivity (Hc), initial permeability (μ_i) and maximum differential permeability (μ_{max})

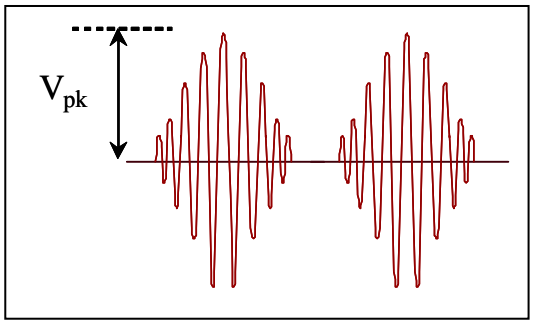

Figure 2.10: Magnetic Barkhausen emissions signal for full magnetizing cycle

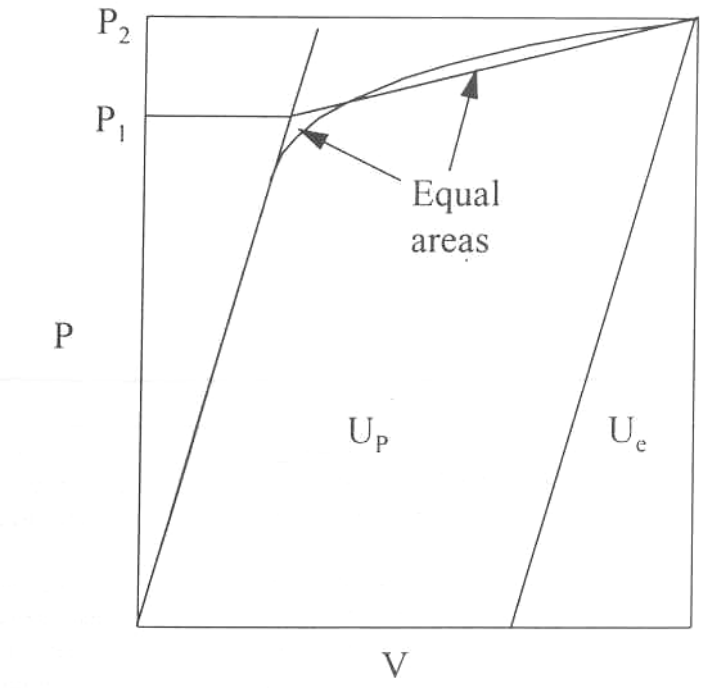

Figure 2.11: Schematic illustration of load (P), load-line displacement (V) diagram.

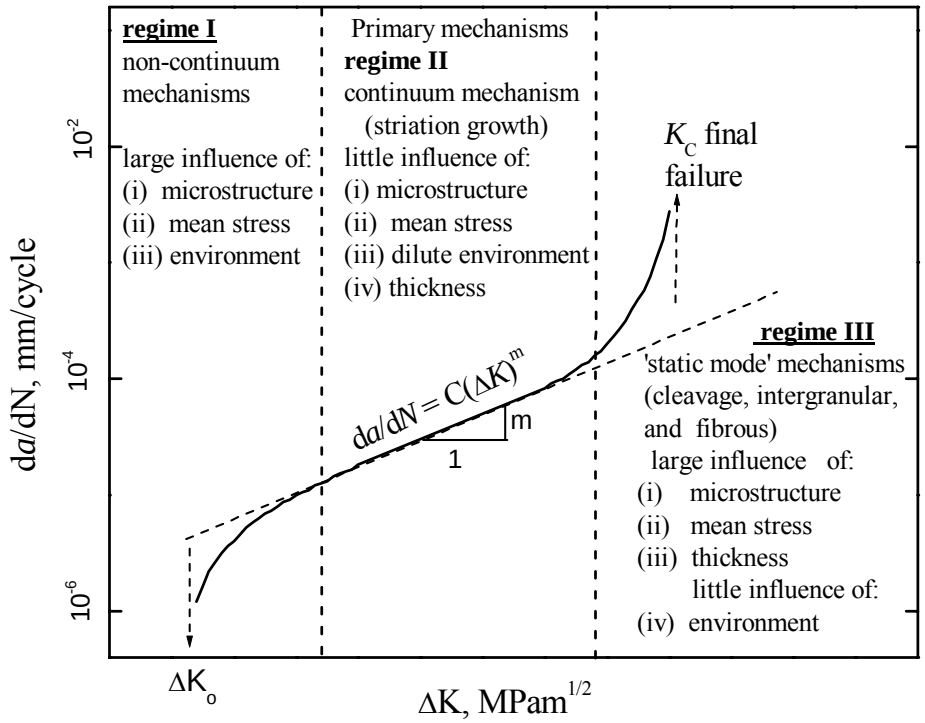

Figure 2.12: Schematic diagram of three regimes of fatigue crack growth.

Chapter 3.0

Heat-treatment and Characterisation of HSLA-100 Steel

3.0

Heat-treatment and Characterisation of HSLA-100 Steel

3.1 Introduction

The influence of process parameters and microstructure on the mechanical properties based on literatures have been reviewed in Chapter-2. There is an increasing demand for high strength steel with adequate toughness and weldability with properties like – (i) higher YS for greater load bearing capacity by thinner section (ii) high resistance to brittle fracture as also low impact transition temperature. HSLA-100, a low carbon copper bearing steel can provide various combinations of strength and toughness by judiciously engineering the microstructure through various processes like - rolling and ageing, normalising and ageing, quenching and ageing. This steel has been developed based on – (i) low carbon content (ii) sufficient alloying elements to get desired impact transition temperature and (iii) engineering the microstructure by micro alloying and thermo mechanical controlled processing (TMCP). Copper contributes significantly in increasing yield strength of HSLA-100 steel on ageing without impairing weldability.

Ageing behaviour of HSLA steel by electrical resistivity measurement technique has been studied by Bhagat et al. [75]. An attempt has also been made to study the ductile fracture behaviour of HSLA steel [9]. However, influence of Cu precipitation and microstructural constituents on tensile fracture behaviour of HSLA steel has not

been explored much. In this chapter, ageing behaviour and tensile fracture behaviour of the steel has been reported after engineering various microstructure by solution treatment, followed by water quenching and subsequently ageing at various temperatures. Microstructural and tensile properties were studied for all specimens on ageing. Scanning electron microscopy (SEM) and transmission electron microscopy (TEM) with energy dispersive X-ray microanalysis (EDS) were carried out for microstructural characterisation. The influence of precipitation and microstructural constituents on ageing behaviour and tensile fracture behaviour has been discussed in this chapter.

3.2 Experimental Work

3.2.1 Material

The material used in this study was Cu-strengthened HSLA-100 steel which was developed for use as naval structural material and this demands for high strength and high toughness along with good weldability [18,22]. The composition of the steel is given in Table-3.1. It may be noted that carbon is kept at a low level to improve weldability, and a high amount of nickel is added to increase hardenability and improve hot workability of the steel. Microalloying with Nb, Ti and V imparts strengthening through stable carbide and carbo-nitride precipitations. The high amount of copper in the steel is necessary for obtaining additional precipitation strengthening through quenching followed by ageing that can provide good combination of strength and toughness required for specific applications.

The material was available in the form of 50 mm thick plate from which specimens were machined with their axes oriented along the rolling direction for the fabrication of tensile and other specimens.

3.2.2 Microstructural Modification through Heat Treatment

The specimens of 200mmx50mmx30mm prepared from 50 mm thick steel plate were solutionised at 910^{o}C for 1 hour and subsequently water quenched (WQ). The quenched specimens were aged at different temperatures from 350^{o}C to 750^{o}C in steps of 50^{o}C for 1 hour and air-cooled to room temperature in order to produce different microstructure. Few additional specimens were aged at 675^{o}C. The temperature was controlled within ± 2^{o}C using a Eurotherm temperature controller. Specimens of appropriate dimensions were extracted from the steel plate for investigation. A few specimens were preserved after austenising treatment to investigate the as-quenched properties of the material.

3.2.3 Microstructural Characterisation

Microstructure of HSLA-100 steel like other structural materials controls the deformation of material which has a profound effect on the parameters that are used to characterise the fracture behaviour of materials. Microstructure include distribution of phases, chemistry of phases, size of particles and precipitates, chemistry of the particles and precipitates, grain size, preferred orientations of grains if any, degree and nature of banding etc. All of these features influence the effect of microstructure on deformation and fracture behaviour of materials. The complexities in microstructure, influence mechanical properties like hardness or tensile strength that reflect the overall performance of a microstructure, and these indices are further used to understand the influence of microstructure on fracture mechanics parameters.

3.2.3.1 Scanning Electron Microscopy

Metallographic samples were prepared by conventional grinding and polishing techniques for microstructural observation. Specimens for scanning electron microscopy (SEM) were etched with 4% nital. A high-resolution analytical scanning electron microscope (JEOL JSM 840A SEM) and Noran Quest energy dispersive spectroscopy (EDS) system was used for microstructural characterisation. Due to instrumental

limitation (spatial resolution limitation) of energy dispersive X-ray, only semi-quantitative X-ray microanalysis was carried out. Quantitative analysis of very small particle (< 1 μm) is not possible in conventional SEM-EDS. However, care was taken to achieve the best possible spatial resolution by optimising and adjusting instrumental parameters such as probe current, accelerating voltage, beam dia (spot size) etc.

3.2.3.2 Transmission Electron Microscopy

Thin foils were prepared for examination in a TEM. Thin slices of 0.2mm thickness were cut off by a slow speed precision diamond wheel cutter. Thickness of specimens were reduced to 0.1mm by careful manual grinding on silicon carbide emery papers of 800 grits with an intermittent cooling in running water to avoid any rise in temperature. Coupons of 3mm dia specimens were punched by a Gatan precision punching system. The specimens were finally thinned in a twin jet electropolishing unit (Tenupol – III) at 40V using a mixture of 10% per chloric acid and 90% acetic acid. Specimens were washed thoroughly in alcohol and dried properly. The electro-polished thin foils were examined in a TEM (Philips CM 200 with EDAX) at 200 kV operating voltage. The EDAX was used for determination of chemical composition of the precipitates.

3.2.4 Evaluation of Mechanical Properties

The heat treatment conditions and resultant microstructure influence the mechanical properties of HSLA-100 steel. Controlling microstructure through optimised ageing condition can impart best combination of strength and toughness in the steel. The evaluation of mechanical properties, like hardness and tensile properties of the steel with respect to different ageing conditions needs detailed information concerning microstructure.

3.2.4.1 Hardness

A computerised hardness-testing instrument (Leica-VMHT) was used for hardness measurement in Vickers scale at a 100 gm load. Hardness was measured on the polished surfaces of the specimens. The average hardness values in different heat-treated conditions have been reported based on 10 numbers of indentations on each specimen.

3.2.4.2 Tensile Properties

The tensile properties of various specimens were obtained by tensile test conducted as per ASTM standard E-8M [202] using a 100kN Instron servo hydraulic testing machine. At least, three specimens were tested for each ageing condition. Round specimens of 25 mm gauge length and 5 mm gauge diameter were prepared as per ASTM standard. A constant displacement rate of $3x10^{-3}$ mm/s, with a 25mm gauge length extensometer mounted over 5mm gauge diameter specimens was employed at room temperature ($28^{o}C$) to measure strain and this was continued until fracture.

3.2.4.3 Study of Fracture Surfaces

Fracture surfaces of tensile test specimens were examined in a SEM (JEOL JSM-840A). Suitable portion of both ends of fracture surfaces were cut and cleaned in an ultrasonic cleaner for 5 minutes before observation in a scanning electron microscope. SEM fractographs were recorded at different magnifications to study fracture surface of each specimen.

3.3 Results and Discussion

3.3.1 Variation in Microstructure of HSLA-100 Steel on Ageing

Secondary electron images (SEI) of different heat-treated conditions of Cu-strengthened HSLA-100 steel under investigation are shown in Fig. 3.1 to Fig. 3.3. The microstructure of the steel in water-quenched condition shows a mixture of acicular ferrite, bainite and lath martensite. In order to identify different microstuructural constituents and their variation on ageing in HSLA-100 steel, it was necessary to undertake detailed TEM-EDS studies. The findings are summarised in Table-3.2. Figure 3.4 is bright field electron image of water-quenched sample. Microstructure in quenched condition is primarily consisting of lath martensite, acicular ferrite and bainite. Acicular ferrite generally shows morphology of parallel lath similar to lath martensite, however the orientation difference between adjacent ferrite plates is greater and interfaces are not as straight as in lath martensite. Though morphological appearance of bainite and acicular ferrite are similar, carbides are mainly distributed in bainite. Figure 3.5 is the TEM micrograph of water quenched (WQ) sample showing carbides ($M_{23}C_6$) in bainite matrix. A few occasional carbides and carbonitrides are distributed within ferrite laths. Though morphological appearance of bainite and acicular ferrite are similar to many extent, however carbides are seen to be distributed within ferritic laths as well as along lath boundaries in bainite. Figure 3.5(a) is bright field electron image of $M_{23}C_6$ carbide. The selected area diffraction pattern (SADP) from the above precipitate is shown in Fig. 3.5(b) and the schematic illustration is shown in Fig. 3.5(c). Figure 3.6 (a) shows the distribution of some fine carbides interacting with dislocations with in the ferritic lath. Figure 3.6(b) is the selected area diffraction pattern (SADP) from MO_2C as shown by arrow in Fig. 3.6 (a). The schematic illustration of the SADP is shown in Fig. 3.6(c). This confirms the carbide as MO_2C. Figure 3.7(a) shows bright field image of fine precipitates within ferrite at a higher magnification. Figure 3.7(b) shows SADP taken from a precipitate shown by arrow in Fig. 3.7(a). Schematic illustration of the SADP of Fig. 3.7(b) is shown in Fig. 3.7(c). This confirms the fine precipitate as Nb(CN).

The lath martensite is gradually tempered on ageing. Microstructures in Fig. 3.1 to Fig. 3.3 reveal a gradual decrease in substructure in the samples aged up to 700^{o}C. Formation of small martensite island is occurred when the steel is aged above

675°C. The entire range of ageing temperatures can be divided into four regimes as it has been observed that microstructural changes follow a definite pattern in each regime.

With reference to Table-3.2, TEM micrographs (Fig. 3.4 to Fig. 3.16) reveal the evolution of various microstructural constituents of the steel on ageing. Water quenched microstructure consisting of lath martensite and acicular ferrite are stable up to 500°C during ageing. Beyond this temperature, martensite gets progressively tempered and the recovery of ferrite occurred vide Fig. 3.11. A small amount of austenite is retained in the quenched microstructure that continues to be stable and persist throughout the ageing temperature range, which is shown in Fig. 3.8 and Fig. 3.13(b) respectively. Above 675°C, as the ageing temperature exceeds A_{C1} temperature, a few ferrites transform to reverted austenite and subsequently on cooling, a part of reverted austenite converts to small martensite islands as shown in Fig. 3.15. The size of these newly formed martensite islands varies from 1μm to 3 μm in the specimen aged at 700°C as observed in TEM. Fine microalloying carbides (Fig. 3.12) and carbonitrides are also stable up to 700°C ageing temperature.

Low carbon lath martensite along with acicular ferrite and bainite are formed after solution treatment of the steel at 910°C followed by quenching. The maximum solubility of copper in iron is 2.11wt% [69]. A super saturated solid solution of iron with copper is formed on quenching of the steel. Higher copper content (1.6wt%) together with manganese in the steel reduces transformation temperature and shifts the nose of the CCT curve to the right [70]. Retained austenite is found in between martensite laths, and it is found to be very stable due to the presence of γ-iron stabilisers like Cu, Ni, and Mn in the system. $M_{23}C_6$, Mo_2C and Nb(CN) are also found in water-quenched specimen (Fig. 3.5 to Fig. 3.7). These stable carbides and carbo-nitrides are formed during solidification and thermo-mechanical processing of the steel at higher temperature at around 1100°C [56]. Ageing in the temperature range of 350°C-675°C for 1 hour does not change the morphology and composition of these stable carbides and carbonitrides. During ageing, copper precipitate comes out from the super-saturated solution and causes the increase in hardness and strength through precipitation hardening.

Copper goes in solid solution as a super saturated solute in the quenched state and precipitates as nano scale coherent particles on ageing upto 500^{o}C as revealed in Fig. 3.9, subsequently coarsen and loose coherency at higher temperatures of ageing as shown in Fig. 3.14. Very fine ε- Cu precipitates accompanying by strain contrasts and cluster of copper rich particles have been observed in the specimens when aged between 400^{o}C- 500^{o}C as shown in Figures 3.9 and 3.10. Size of these copper precipitates is less than 20 nm. Strain field surrounding precipitates and fringes indicate the possibility of coherency with matrix and TEM- EDS result shows an increase in copper concentration. On ageing above 500^{o}C, Cu precipitates loose the coherency and spherical tiny copper particles grow into larger road shaped fcc Cu precipitates vide Figures 3.14 and 3.16. This has also been reported by earlier workers [63,64,203-205].

Such rod shaped fcc copper precipitate is formed by a shear transformation as reported by B. Soylu and R.W.K. Honeycombe [206]. In the present study, Cu rich particles with strain field are observed in the initial stage of ageing and were analysed in TEM-EDS. Hornbogen and Glenn mentioned that bcc Cu rich clusters readily transform to fcc Cu at a small size and the strain contrast of coherent precipitates is difficult to observe [61]. Other researchers also suggested that bcc copper rich clusters precipitate first form from the supersaturated solution of iron and then transformed to fcc phase and loose coherency with the matrix when they grow into a critical size [65,207]. In this study, rod shaped Cu- precipitates are found in the specimens when aged above 550^{o}C. The tempering of martensite laths, recovery of acicular ferrite to polygonal ferrite and coarsening of Cu precipitates occur with the increase of ageing temperature above 600^{o}C. The transformation temperature Ac_1 of the steel is lowered down to around 675^{o}C due to presence of alloying elements like Cu and Mn. Therefore, around 675^{o}C small amount of fresh austenite is formed which is not as stable as the earlier retained austenite due to presence of austenite stabilisers in lesser amount. It was found that this newly formed reverted austenite readily transform to new small martensite island during cooling from 700^{o}C. Ageing above 700^{o}C (fourth stage), causes formation of granular bainite, recovery of martensitic laths and acicular ferrite as well as coarsening of carbides and Cu precipitates.

3.3.2 Variation in Mechanical Properties of HSLA-100 Steel on Ageing

Vickers hardness-testing instrument (100 gm load) was used for determination of hardness values of water quenched and aged specimens. The results show ageing behaviour of the steel. There is a change in the hardness value with a change in ageing temperature. Figure 3.17 is the graphical representation of the hardness as a function of ageing temperature. From the plot, ageing behaviour of the steel can be classified into four stages. In the first stage, hardness increases with an increase in ageing temperature. Maximum hardness value of 343 Hv is obtained in the first stage at 500^{o}C. In the second stage, hardness value decreases with increase in the ageing temperature above 550^{o}C and lowest hardness value of 252 Hv is obtained at 675^{o}C. Third stage is associated with a rise in hardness value and at 700^{o}C, a second peak in hardness value of 280 Hv is recorded. Subsequently hardness value decreases at 750^{o}C, which is considered as fourth stage.

The variation in YS, UTS and hardness of HSLA-100 steel with change in ageing temperature are also shown in Fig. 3.17. The mechanical properties obtained in tensile testing are tabulated in the Table-3.3. During the 1st stage or initial stage of ageing, YS and UTS increase with a rise in ageing temperature up to 500^{o}C and then Y.S and UTS gradually decrease in the 2nd stage of ageing. The lowest value of strength is obtained around 675^{o}C. Third stage is associated with a rise in strength and at 700^{o}C, a second peak is obtained. Steel is softened and strength decreases above 700^{o}C (fourth stage) due to formation of granular bainite, recovery of martensitic laths and acicular ferrite as well as coarsening of carbides and Cu precipitates. Though the amount of carbon in the steel is 0.04 wt%, a high carbon equivalent of 0.81wt% with desirable amount of Cu facilitates HSLA-100 steel to retain a good strength through ageing.

It can be seen from the Table-3.3, that maximum value of 1121 MPa UTS is obtained at 500^{o}C and minimum value of 921 MPa UTS is obtained at 675^{o}C. Similarly, maximum value of 1034 MPa YS is obtained at 500^{o}C and minimum value of 640 MPa YS is recorded at 675^{o}C. Maximum percent elongation of 19.84 and minimum percent elongation of 5.9 are obtained in the samples aged at 675^{o}C and 500^{o}C respectively. The relative increasing & decreasing trend in YS and UTS can be seen in Fig. 3.17.

The stress-uniform strain plots of the steel specimens have been drawn to see the deformation or flow pattern as shown in Fig. 3.18. From the plot, it is observed that YS of the material increases and plastic flow of the material is restricted at the initial stage of ageing. However, plastic flow of the material increases and YS decreases in the 2nd stage of ageing. Reverse trend has been observed in percentage reduction in area (%RA) and percentage elongation (%EL) as shown in Fig. 3.19. There is a decreasing trend of percentage RA in the samples on ageing up to 500^{o}C and again this increases in the sample when they are aged beyond 550^{o}C.

Fracture surfaces of all tensile specimens were examined in SEM. A change has been observed with respect to shape, size and depth of microvoids or dimples. Small shallow equiaxed microvoids are pre-dominant in water-quenched specimen. However, specimens aged at temperature between 400^{o}C–500^{o}C, exhibited mixed mode-having quasi-cleavage fracture with smaller size micro-voids. The increase in size of the micro-voids and disappearance of quasi-cleavage are observed in the specimens when aged above 550^{o}C. The detailed features like microvoids, quasi-cleavage are shown in Fig. 3.20 to Fig. 3.22.

Maximum values of hardness and strength are obtained when the steel is aged at 500^{o}C. Hardness and tensile properties of steels are generally very much dependent on the carbon content of the system. As the amount of carbon content in this system is very low, precipitation of very fine ε-Cu particles during ageing causes an increase in hardness as well as strength. Hardness and strength decrease when ε-Cu precipitates coarsen during ageing above 550^{o}C. The increase in hardness, UTS and YS is due to resistance of the material to plastic flow, as the movement of dislocations is reduced and more stress is required to move dislocations. This may be because of the presence of very fine coherent copper precipitates and strain field associated with it, which restricted the movement of dislocations movement. Plastic flow of the material is increased and hardness, YS, UTS decreased in the second stage of ageing above 550^{o}C. Copper precipitates became coarsened and transformed to incoherent rod shaped precipitate in this stage of ageing.

In the third stage (700^{o}C) of ageing, strength is again increased due to formation of new martensite from reverted austenite. Theoretically, the formation of reverted

austenite and new martensite islands might have started below 675^{o}C, but it was not observed in TEM. The increase in strength/hardness above 675^{o}C is the net effect of all microstructural changes, i.e. the effect of formation of new martensite islands overbalancing the negative influence of matrix softening and coarsening of Cu precipitates.

Reverse trend in %RA & %El can be co-related with decrease in plastic flow of the material initially and then plastic flow of the material increases. Strength and hardness decrease above 700^{o}C in the fourth stage due to softening of the matrix, which has also been reported by other researchers [72]. Therefore, specimens aged beyond 700^{o}C were not used for FCGR tests, fracture toughness and magnetic characterisation in this investigation.

Any ductile fracture involves nucleation, growth and coalescence of microscopic voids that initiate at second phase particles and inclusions whereas cleavage fracture involves separation along specific crystallographic planes. Cleavage may be brittle, but it can be preceded by large-scale plasticity and ductile crack growth [208]. Restriction in plastic flow causes cleavage. Fractographic study of the tensile fracture in this investigation revealed that there are two kind of micromechanisms of fracture which are playing role in the steel - (i) mixed fracture i.e. quasi-cleavage along with small shallow dimples which are dominant in specimens aged between 400^{o}C–500^{o}C and (ii) ductile fracture i.e. initiation, growth and coalescence of microvoids which are predominant in the specimens aged above 550^{o}C. The carbides, nitrides and inclusions like stable second phase particles, which are responsible for initiation microvoids during ductile fracture and remain unchanged throughout the ageing process. However precipitation of nanosize coherent Cu particles, are gradually coarsened and loose coherency on ageing at higher temperatures. Therefore, the appearance of quasi-cleavages may be due to the precipitation of coherent copper particles. On the other hand incoherent copper precipitates facilitate microvoid initiation and hence, increases ductility. The presence of larger microvoids and disappearance of quasi-cleavages in later stages of ageing support this argument. Ductility is further increased due to the recovery of martensite and acicular ferrite.

3.4 Conclusions

Microstructure of HSLA-100 steel used in this study consists of lath martensite, acicular ferrite and bainite in water-quenched condition. Small amount of retained austenite are also found in WQ specimen, besides a few carbides [$M_{23}C_6$ and Mo_2C] and carbo-nitrides [Nb (CN)]. During ageing, acicular ferrite is transformed to polygonal ferrite and recovery of martensite lath occurs. Precipitation of coherent Cu rich particles started manifesting its effect from 400^0C. Nano-size coherent Cu precipitates gradually coarsened and loose coherency with over ageing above 550^0C due to growth of fcc copper precipitates. There was no change in shape and size of the carbides and carbo-nitrides due to ageing below 700^0C for one hour.

Here, two types of micromechanism of fracture are playing role during tensile fracture- (i) micro-cleavages are dominant in specimens aged between 400^oC–500^oC and (ii) initiation, growth and coalescence of microvoids are predominant for rest of the specimens aged above 550^oC. The plastic flow of the material is restricted in the initial stage of ageing due to precipitation of very fine coherent Cu-rich particles leading to an increase in brittleness, strength and hardness at the expense of the ductility of the material. At a later stage of ageing (above 550^oC), these precipitates coarsened and loose their coherency and promote the increase in ductility and flow of the material. Hardness and strength decreases in this stage. Around 700^oC, the hardness and strength increases due to the formation of new martensite islands from reverted austenite. Above 700^oC, due to softening of the matrix and coarsening of the precipitates, hardness and strength of the material decreases.

Table-3.1: Chemical composition of HSLA steels in weight percent

Steel	*C*	*Mn*	*P*	*S*	*N*	*Si*	*Cr*	*Mo*	*Ti*	*V*	*Nb*	*Ni*	*Cu*
HSLA-100	0.04	0.90	0.01	0.005	0.015	0.25	0.6	0.60	0.02	0.03	0.03	3.50	1.60

Table-3.2: Evolution of microstructural constituents with ageing in HSLA-100 steel

Water quenched	Aged between 350^{o}C-500^{o}C	Aged between 550^{o}C-650^{o}C	Aged between 675^{o}C-700^{o}C
Lath martensite	No change in morphology/content of lath martensite	Break-up of martensite laths and transformation into tempered martensite	Recovery of martensitic laths
Acicular ferrite	No change in morphology/content of Acicular ferrite and	Recovery of acicular ferrite and formation of polygonal ferrite	Formation of polygonal ferrite
Retained austenite	No change in morphology/content of Retained austenite	No change in retained austenite	Formation of austenite
Carbides and Carbonitrides	Stable population of Carbides and Carbonitrides	Stable population of Carbides and Carbonitrides	Stable population of Carbides and Carbonitrides
Cu in solution in super saturated condition	Coherent precipitation of nanoscale Cu, increasing in amount with increasing ageing temperature	Loss of coherency due to growth of fcc copper precipitates	Coarsening of Cu precipitate
			Appearance of small martensite islands from *fresh* reverted austenite

Table-3.3: Mechanical properties of the WQ & aged HSLA-100 steel

Heat-treated condition	Hardness (Hv)	E (GPa)	YS (MPa)	UTS (MPa)	% El	%RA
WQ	296	195.0	818	1004	9.38	69.54
350^{o}C	300	203.3	886	1056	8.49	67.88
400^{o}C	321	191.5	957	1076	7.70	62.56
450^{o}C	331	195.7	968	1098	6.46	61.26
500^{o}C	343	200.0	1034	1121	5.9	61.75
550^{o}C	312	192.7	927	1011	14.69	65.09
600^{o}C	271	187.7	698	955	15.92	69.63
650^{o}C	263	192.5	643	934	17.71	70.11
675^{o}C	252	175.4	640	921	19.84	73.27
700^{o}C	280	203.6	831	983	19.12	73.90
750^{o}C	265	194.0	810	931	19.58	73.45

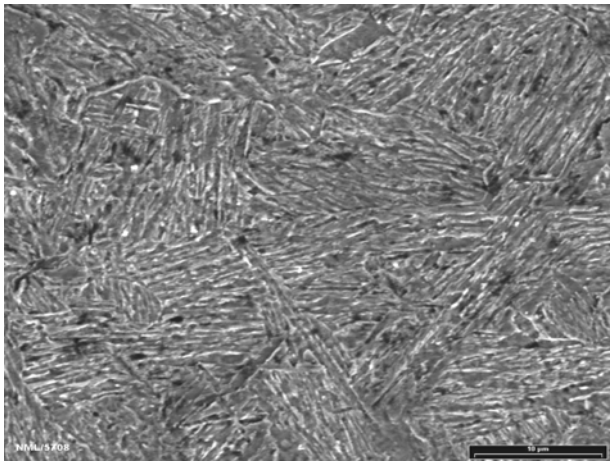

(a)

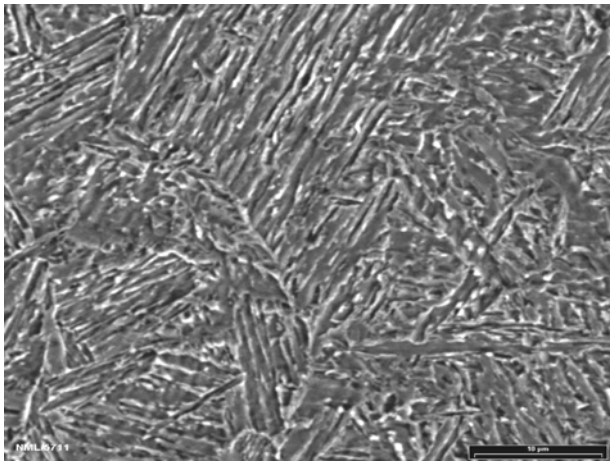

(b)

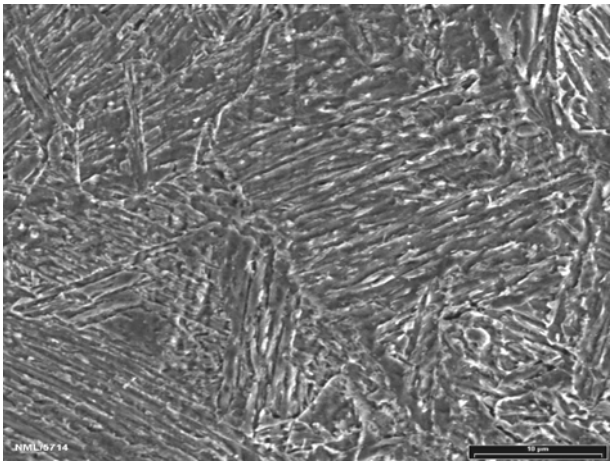

(c)

Figure 3.1: SEM micrographs of WQ and heat treated conditions of Cu-strengthened HSLA-100 steel (a) WQ (b) WQ and aged at 350^{o}C and (c) WQ and aged at 400^{o}C.

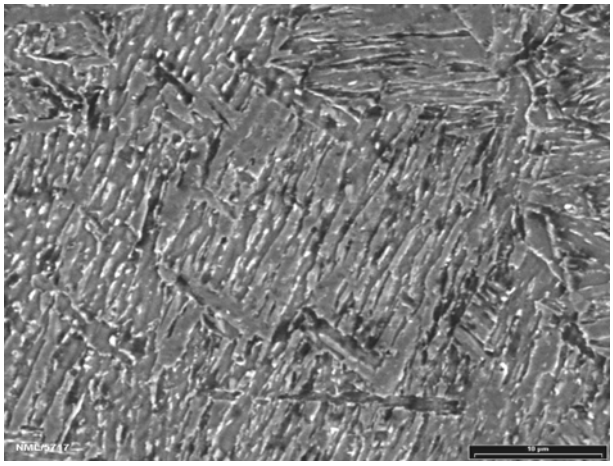

(a)

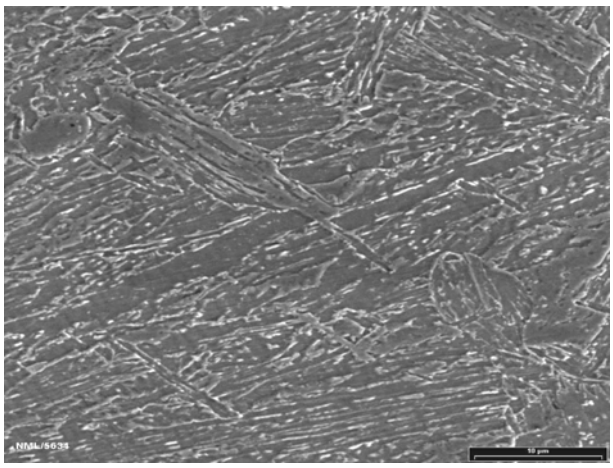

(b)

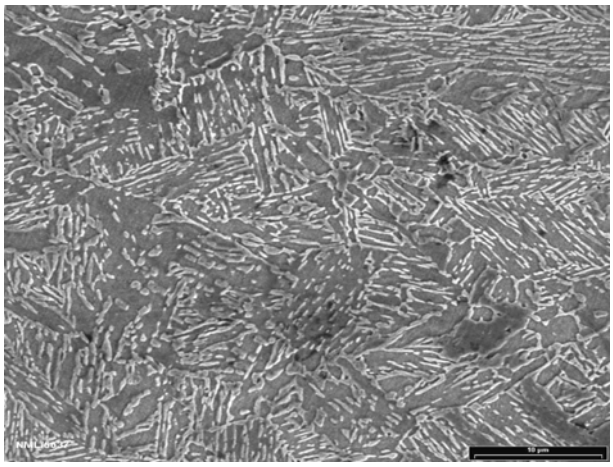

(c)

Figure 3.2: SEM micrographs of different heat treated conditions of Cu-strengthened HSLA-100 steel (a) WQ and aged at 450^{o}C (b) WQ and aged at 500^{o}C and (c) WQ and aged at 600^{o}C.

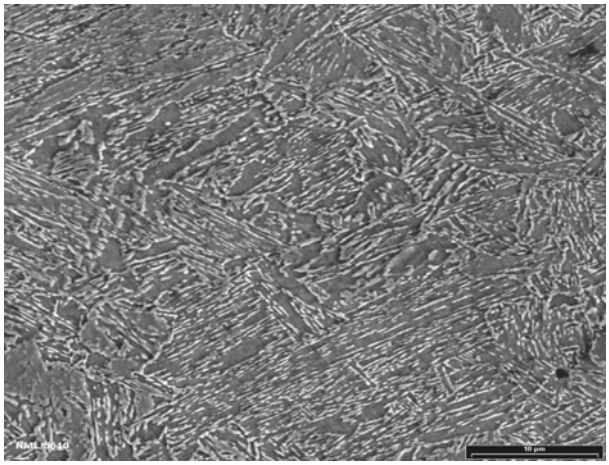

(a)

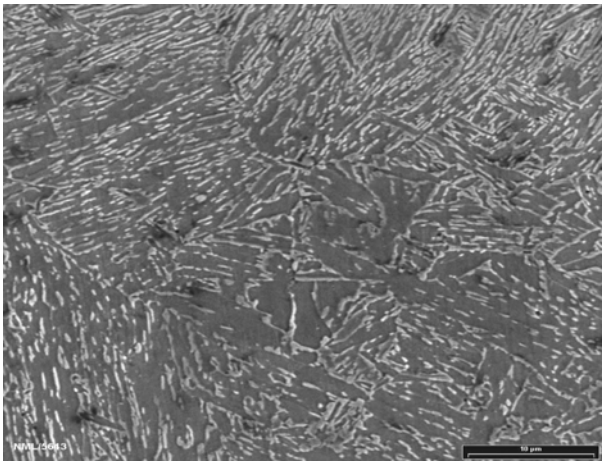

(b)

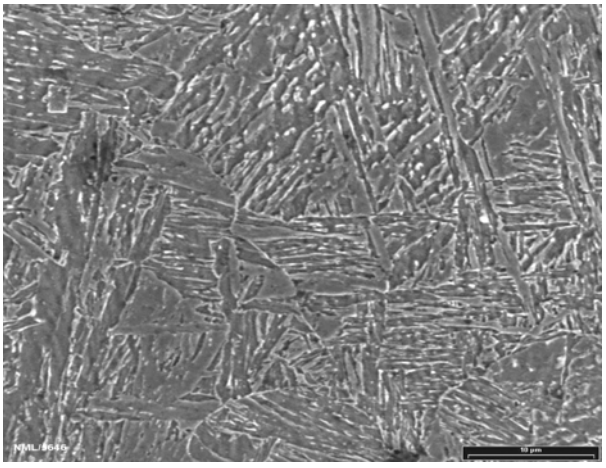

(c)

Figure 3.3: SEM micrographs of various heat treated conditions of Cu-strengthened HSLA-100 steel (a) WQ and aged at 650^{o}C (b) WQ and aged at 675^{o}C and (c) WQ and aged at 700^{o}C.

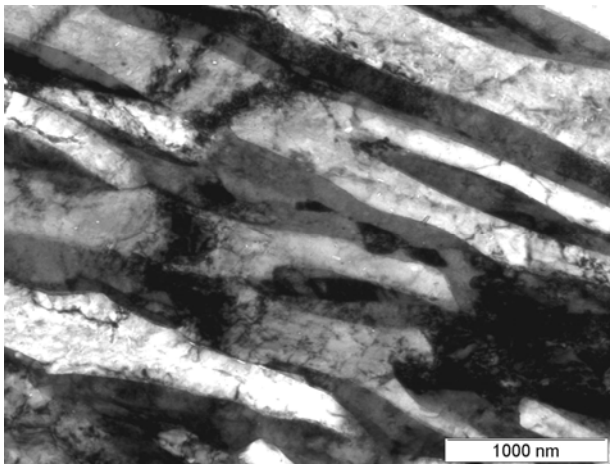

Figure 3.4: Bright field TEM image of WQ HSLA-100 steels showing lath martensite and acicular ferrite.

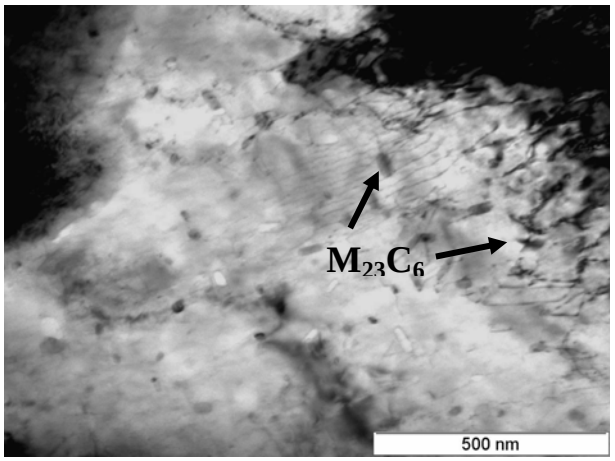

(a)

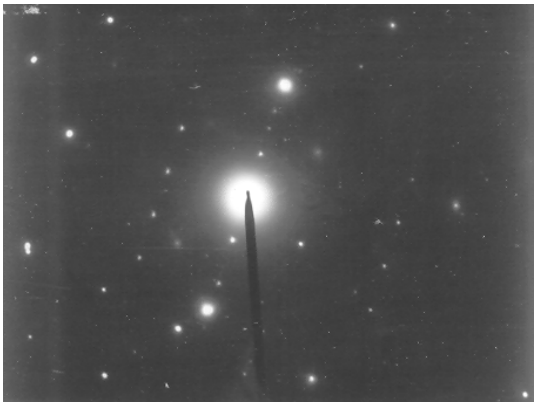

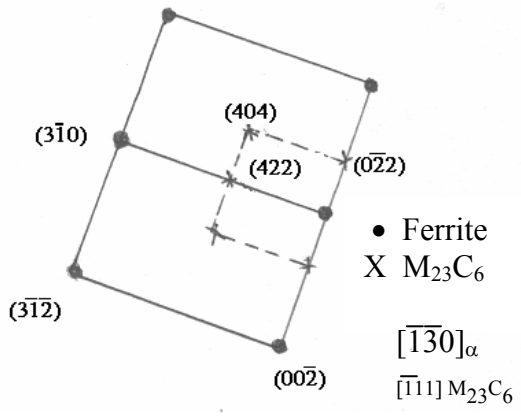

(b) (c)

Figure 3.5: (a) Bright field TEM image of WQ HSLA-100 steel showing $M_{23}C_6$ carbides (b) selected area diffraction pattern (SADP) taken from the carbide and (c) schematic illustration of b.

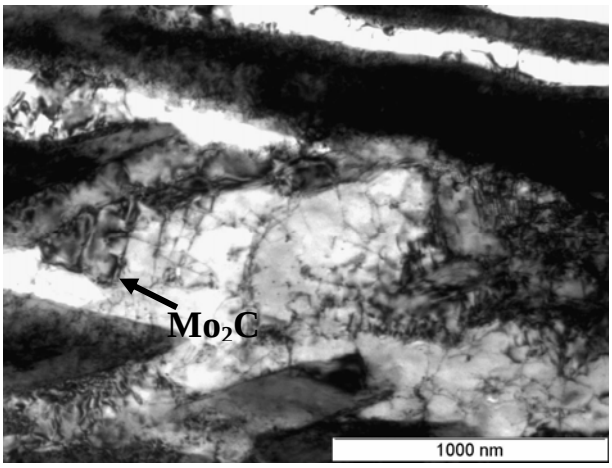

(a)

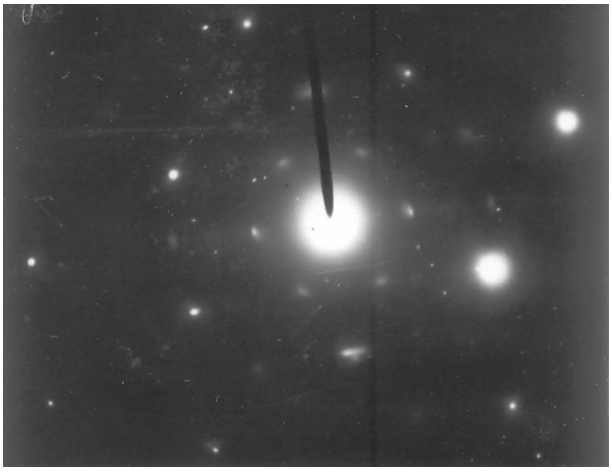

(b)

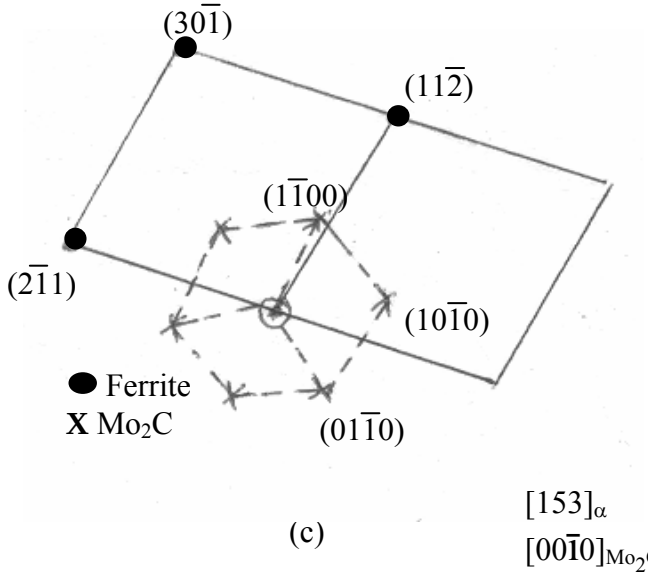

(c)

Figure 3.6: (a) Bright field TEM image of WQ HSLA-100 steel showing Mo_2C carbides in the ferrite matrix (b) selected area diffraction pattern (SADP) taken from the carbide and (c) schematic illustration of b.

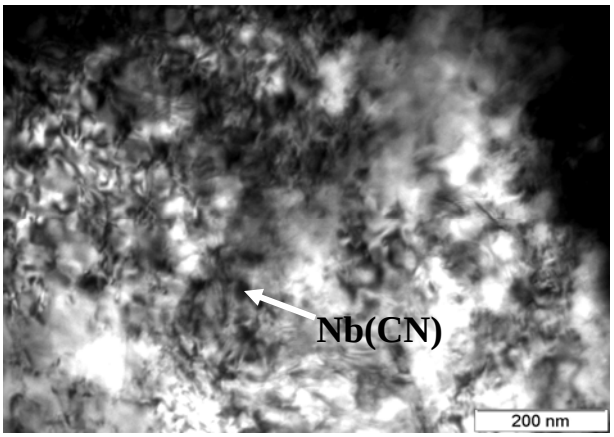

(a)

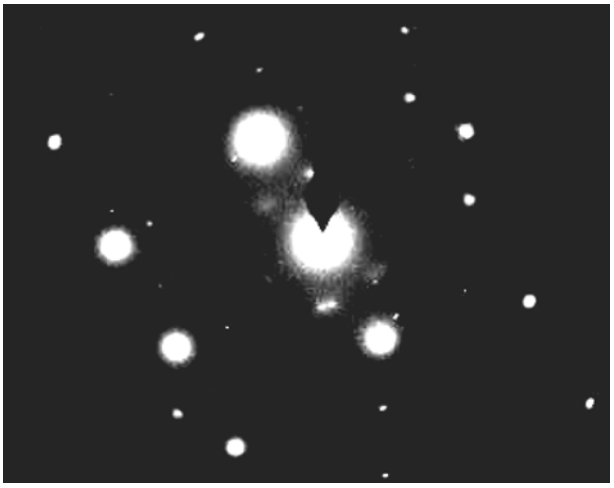

(b)

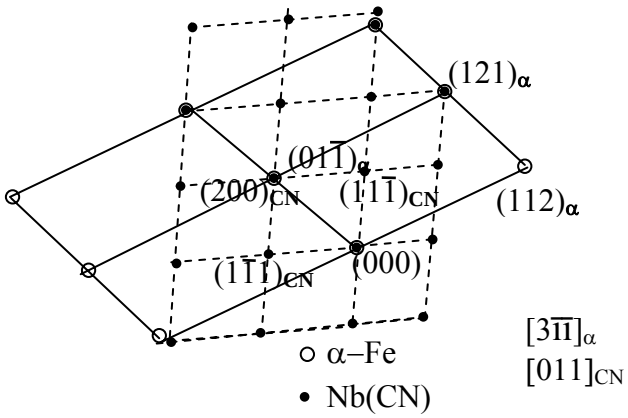

(c)

Figure 3.7: (a) Bright field TEM image of WQ HSLA-100 steel showing Nb(CN) precipitate in the ferrite matrix (b) selected area diffraction pattern (SADP) taken from the precipitate and (c) schematic illustration of b.

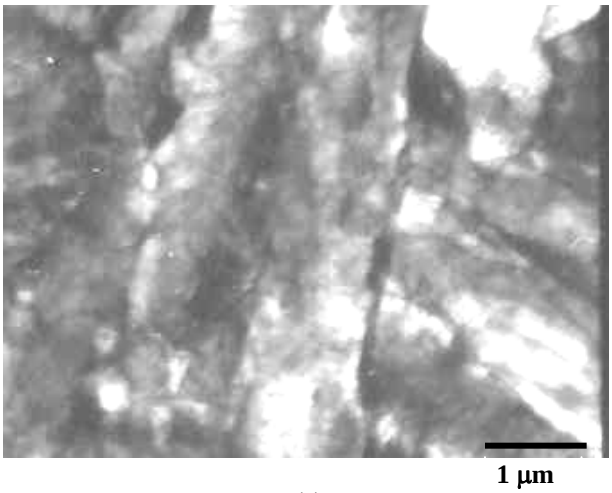

(a)

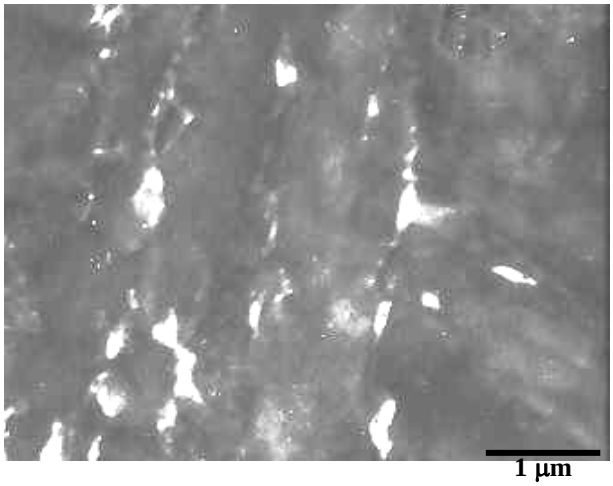

(b)

(c)

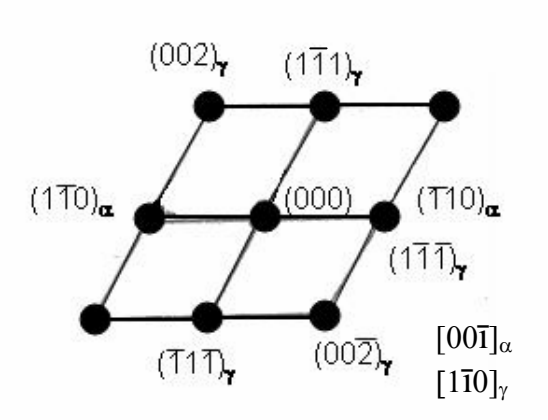

(d)

Figure 3.8: TEM micrographs of water quenched HSLA-100 steel showing retained austenite in between lath martensite (a) Bright Field (BF) image and (b) Centred Dark Field (CDF) image (c) selected area diffraction pattern (SADP) taken from the retained austenite (RA) and (d) schematic illustration of c.

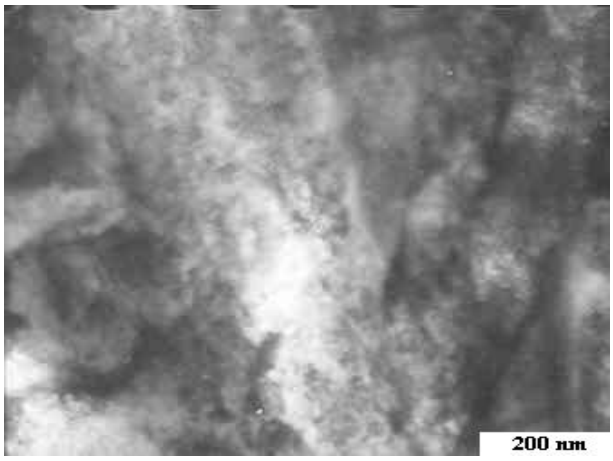

(a)

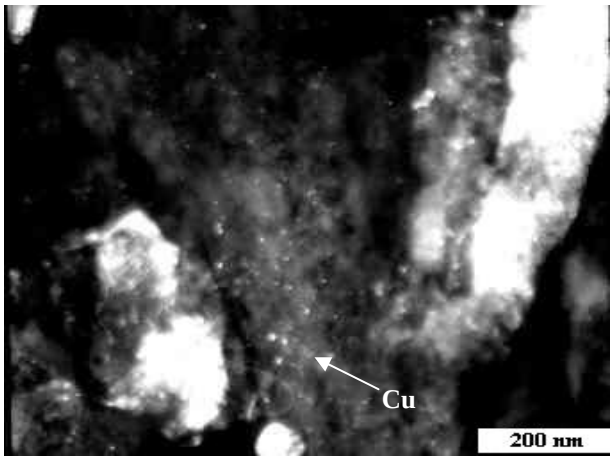

(b)

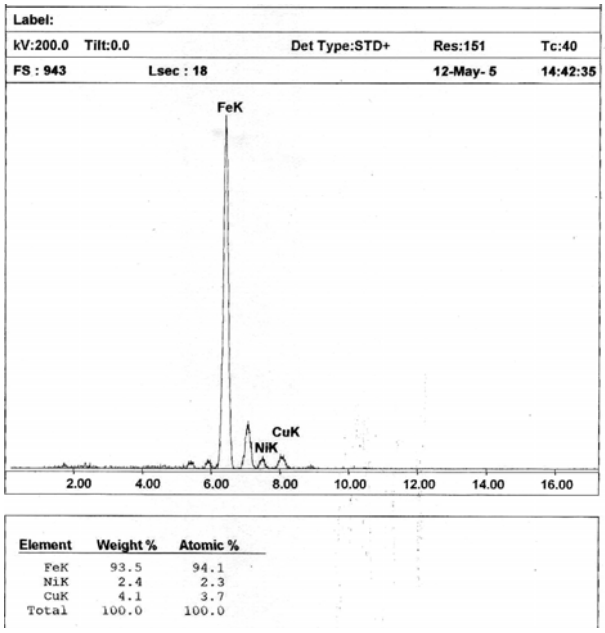

(c)

Figure 3.9: The microstructure of aged (450^{o}C) specimen showing (a) Bright field image of the coherent precipitates of copper cluster (b) corresponding centred dark field (CDF) image and (c) EDS analysis of the Cu cluster.

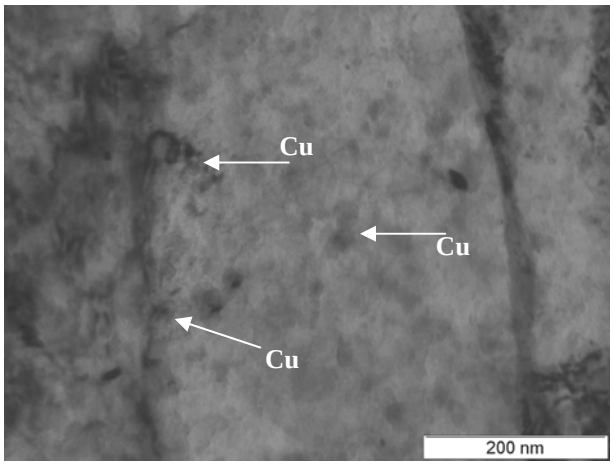

(a)

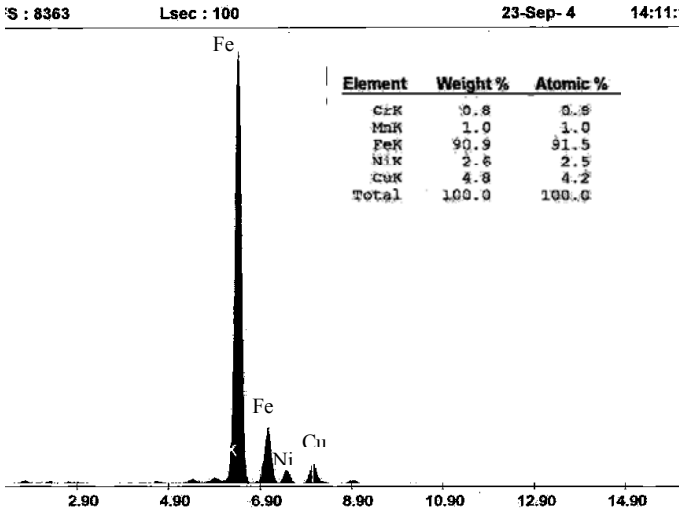

(b)

Figure 3.10: TEM bright field image of aged (500^{o}C) specimen showing (a) very fine coherent Cu precipitates associated with strain field and (b) EDS analysis of Cu precipitate.

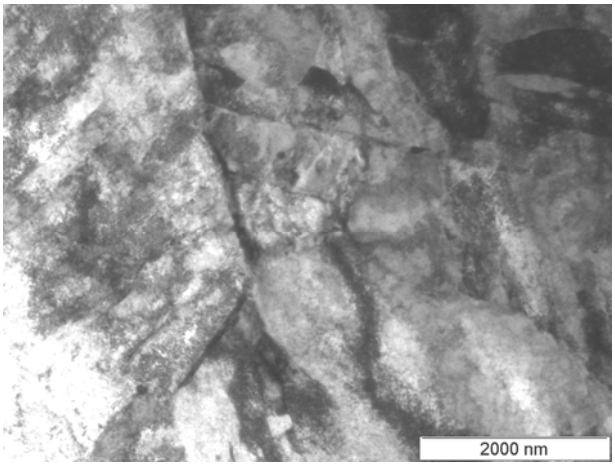

(a)

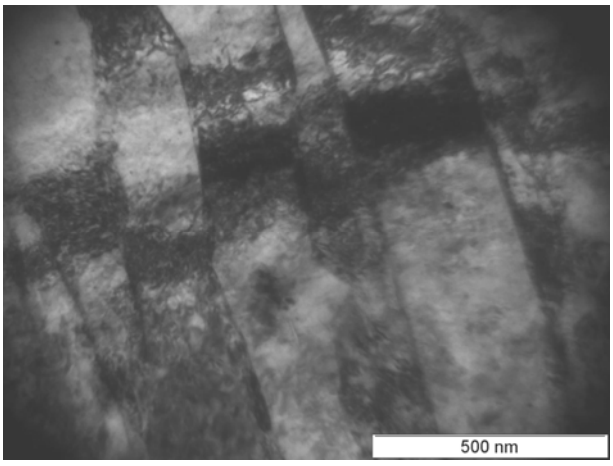

(b)

Figure 3.11: Bright field TEM image of aged (600^{o}C) specimen showing (a) polygonal ferrite and (b) tempered martensite

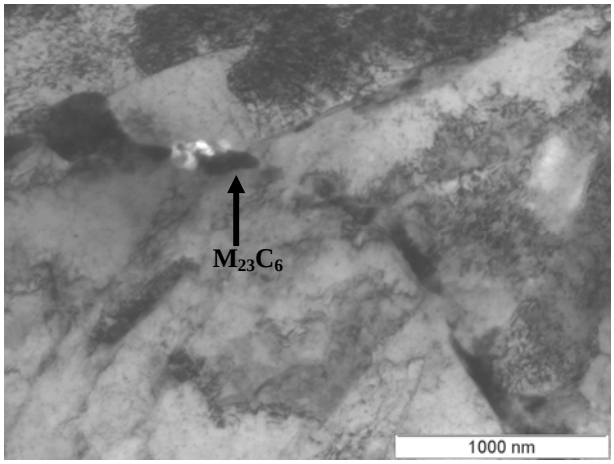

(a)

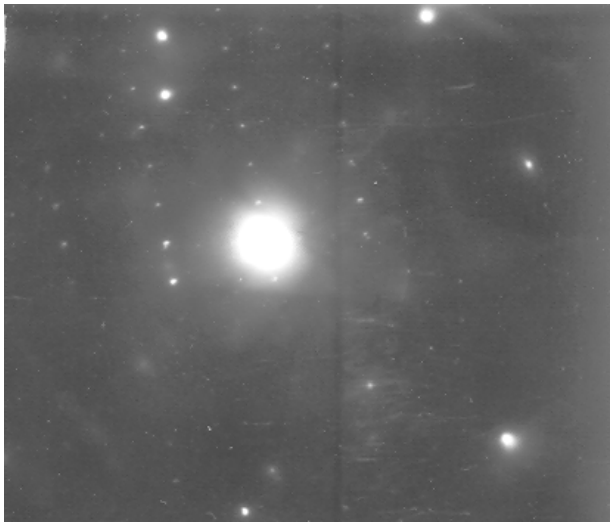

(b)

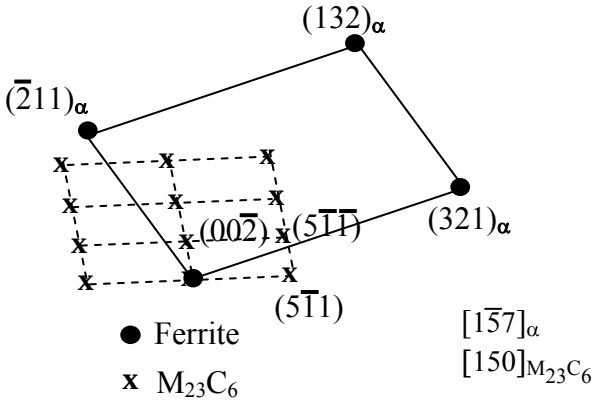

(c)

Figure 3.12: (a) Bright field TEM image of aged (650^{o}C) showing $M_{23}C_6$ carbide (b) selected area diffraction pattern (SADP) taken from the carbide and (c) schematic illustration of b.

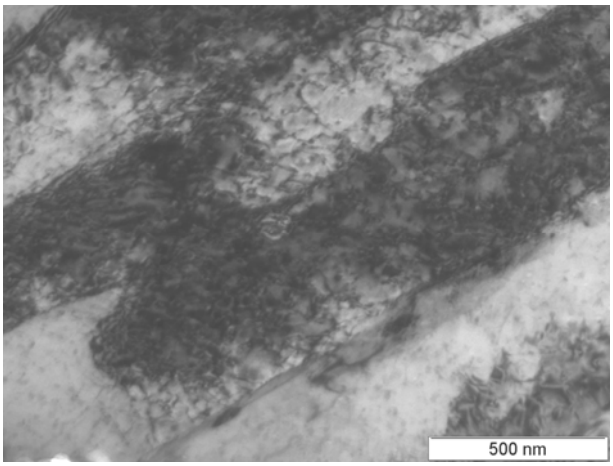

(a)

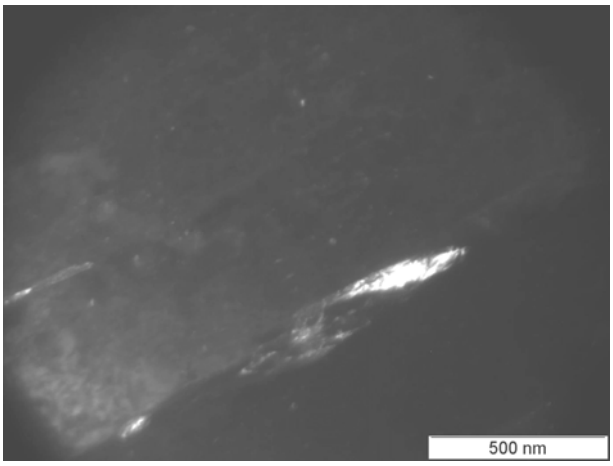

(b)

(c)

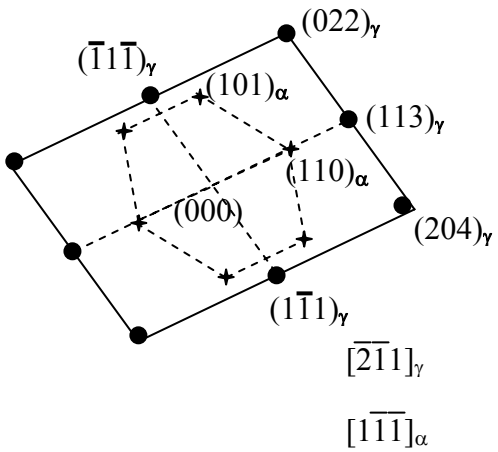

(d)

Figure 3.13: TEM of aged (650^{o}C) specimen (a) bright field image showing tempered martensite (b) centred dark field image showing retained austenite (c) selected area diffraction pattern taken from retained austenite and (d) schematic illustration of (c).

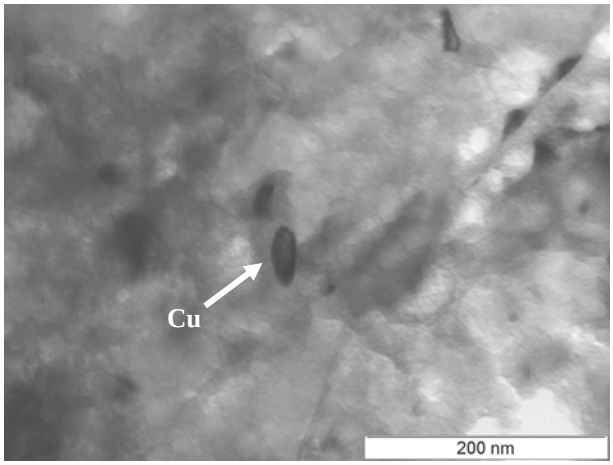

(a)

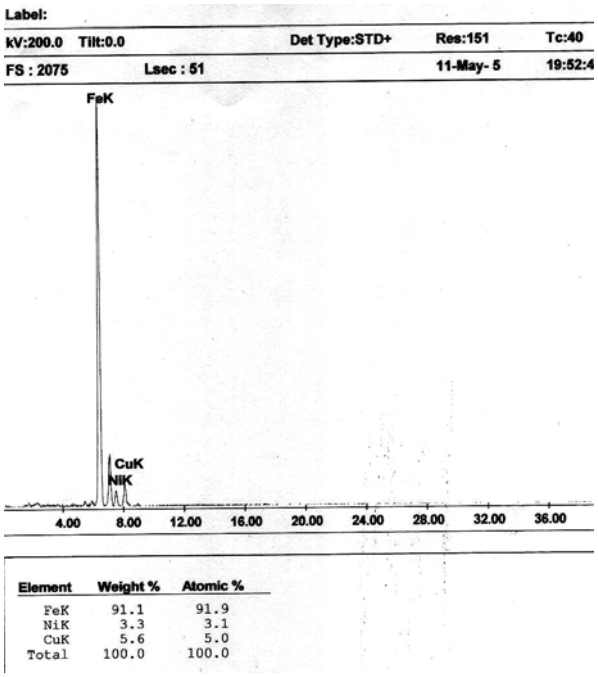

(b)

Figure 3.14: (a) Bright field TEM image of specimen aged at 675^{o}C showing rod-shaped Cu precipitate and (b) EDS analysis of the Cu precipitate

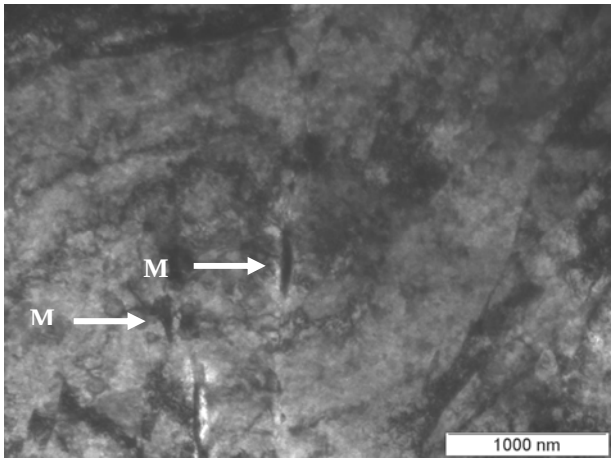

(a)

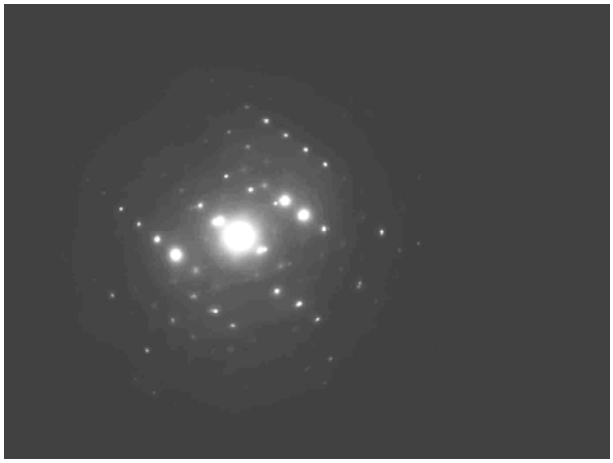

(b)

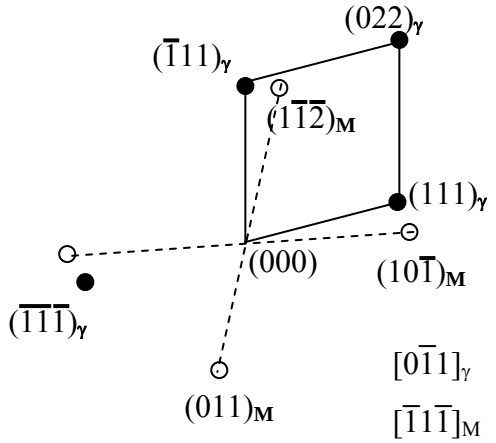

(c)

Figure 3.15: (a) Bright field TEM image of aged (700^{o}C) specimen showing formation of fresh martensite (marked as 'M') from reverted austenite (b) the selected area diffraction pattern (SADP) taken from the martensite and (c) the schematic illustration of (b).

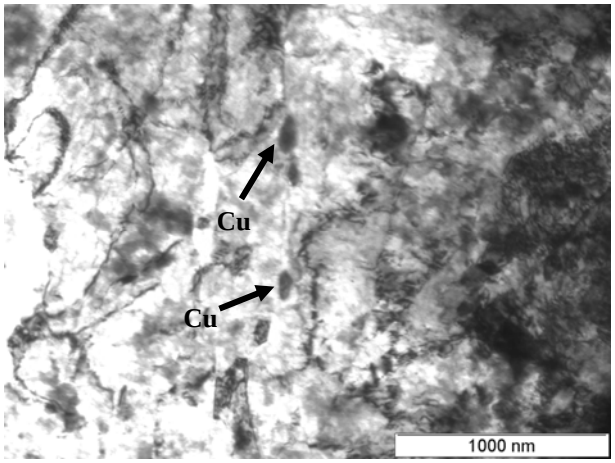

(a)

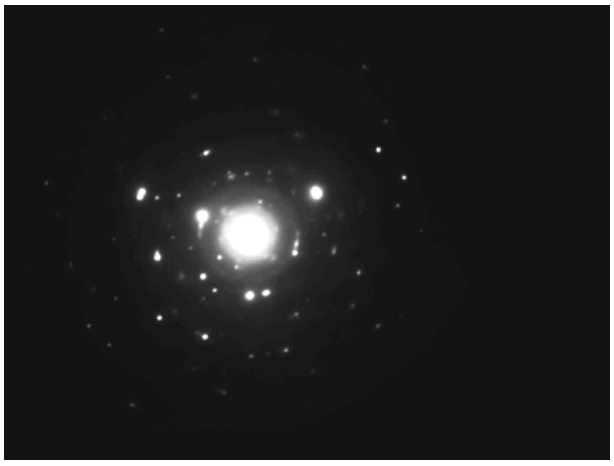

(b)

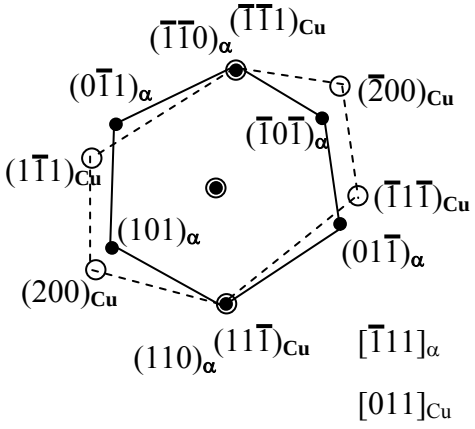

(c)

Figure 3.16: (a) Bright field TEM image of aged (700^{o}C) specimen showing rod shape incoherent Cu precipitate (b) the selected area diffraction pattern (SADP) taken from the precipitate and (c) the schematic illustration of (b).

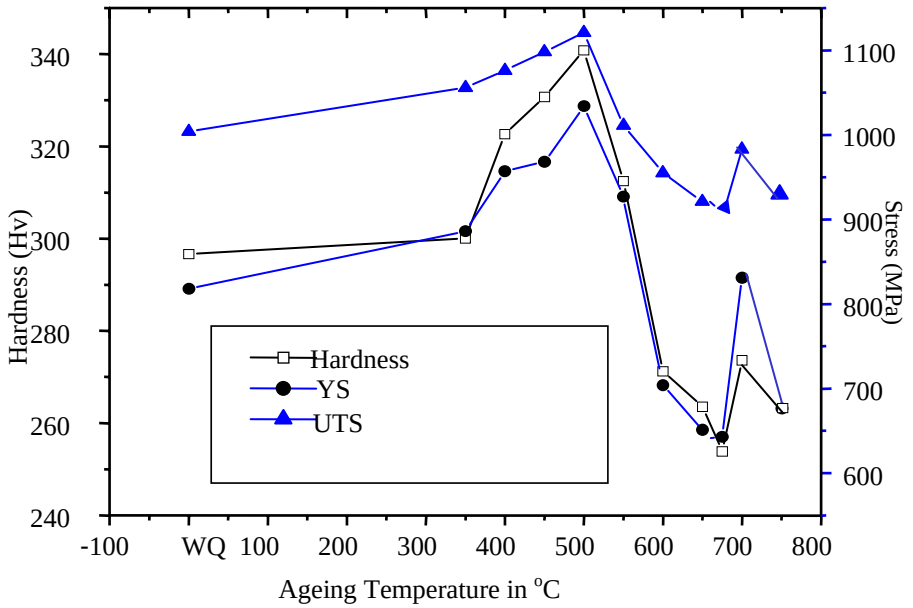

Figure 3.17: Hardness, YS and UTS vs. Ageing temperature

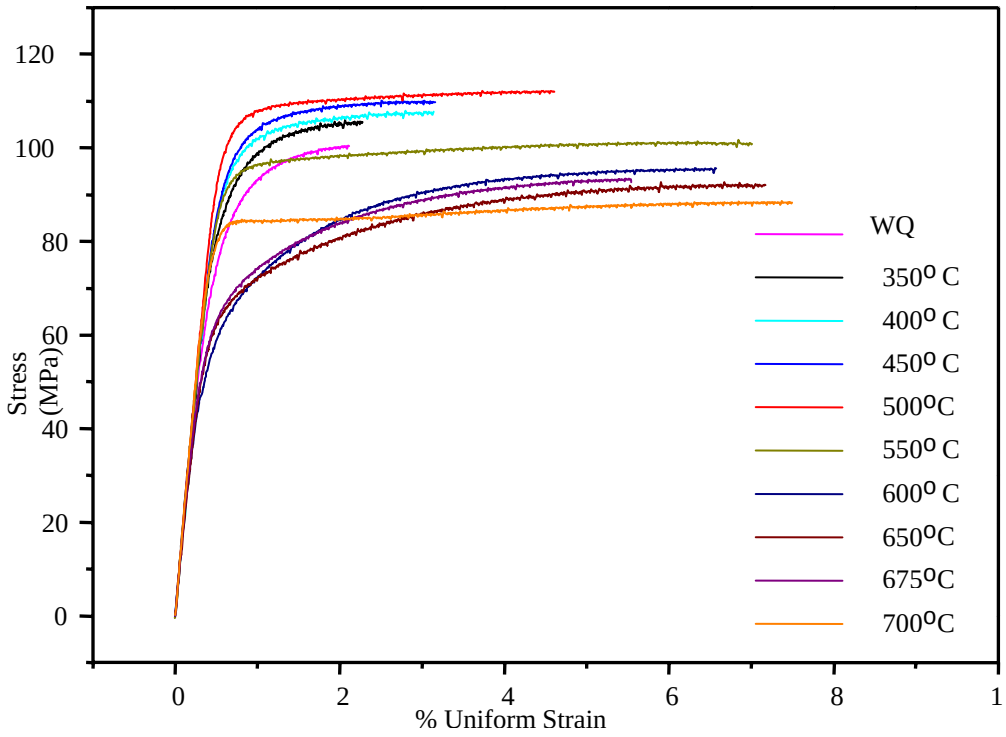

Figure 3.18: Stress as a function of uniform strain

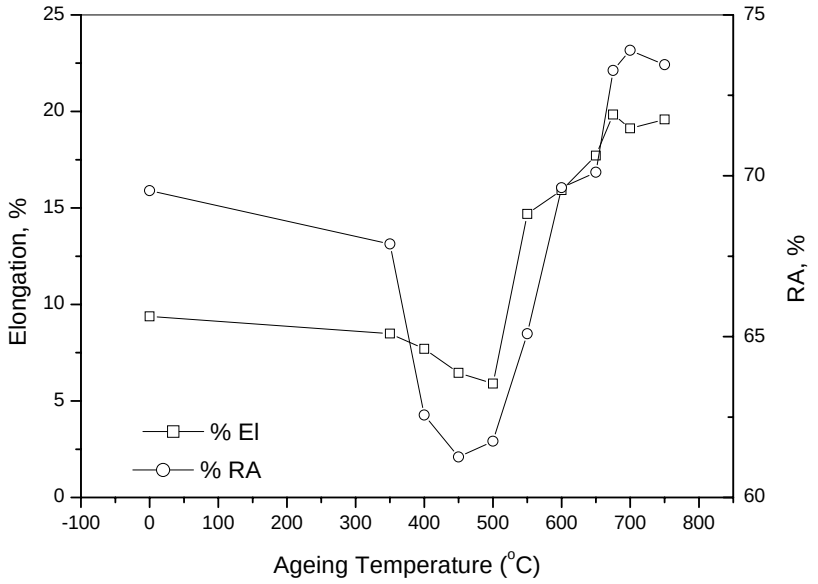

Figure 3.19: % RA and %EL as a function of ageing temperature

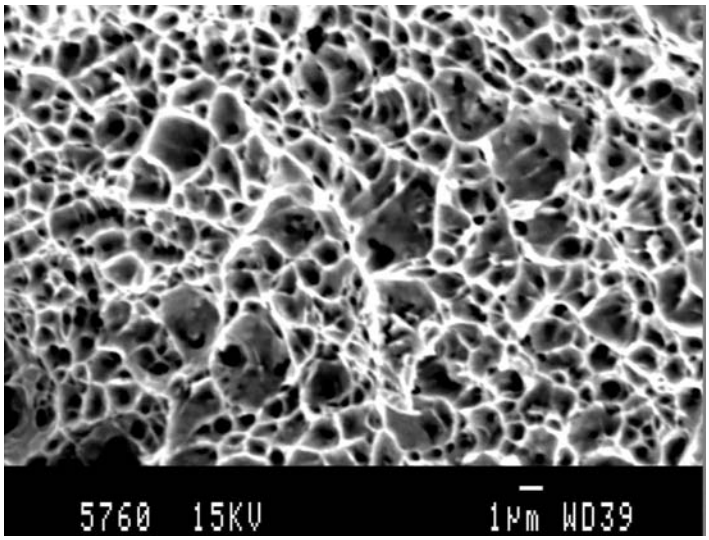

(a)

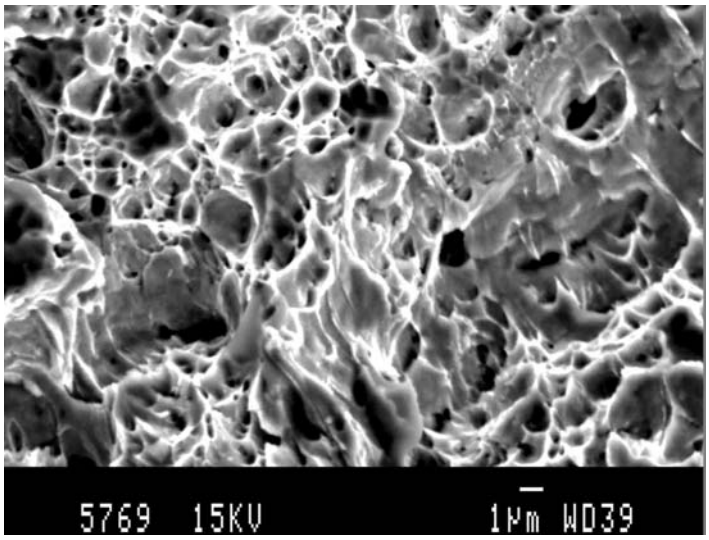

(b)

Figure 3.20: SEM fractographs of tensile tested HSLA-100 steel specimens (a) WQ and (b) aged at 450^{o}C.

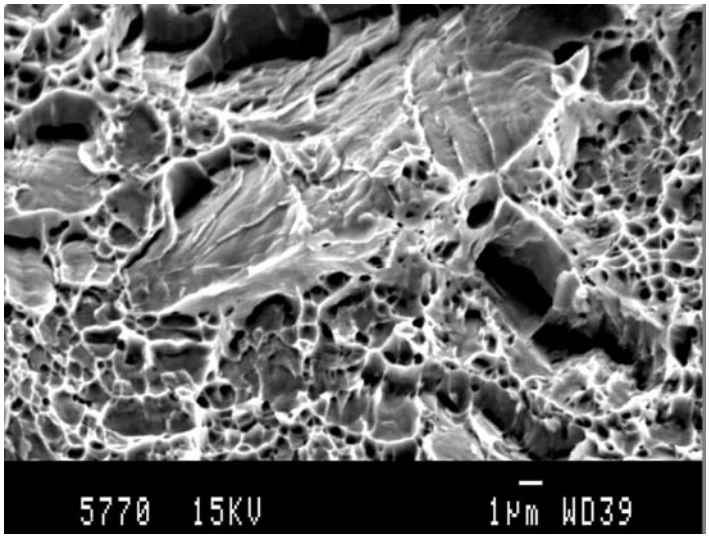

(a)

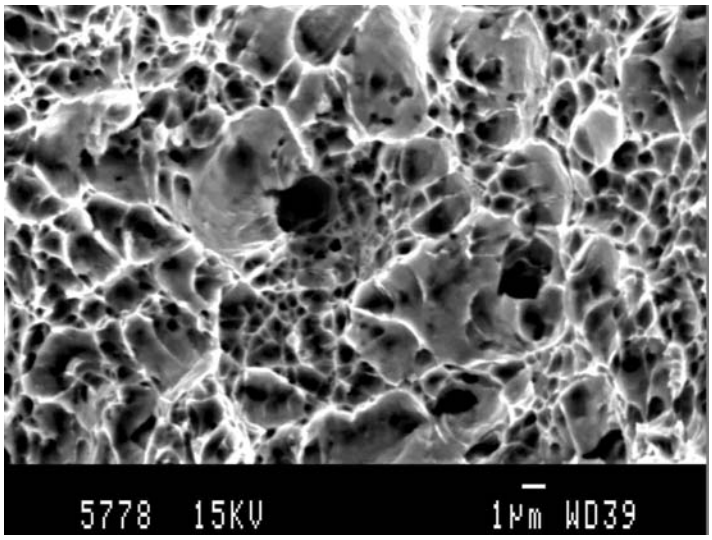

(b)

Figure 3.21: SEM fractographs of tensile tested HSLA-100 steel specimens in different aged condition (a) 500^{o}C and (b) 600^{o}C.

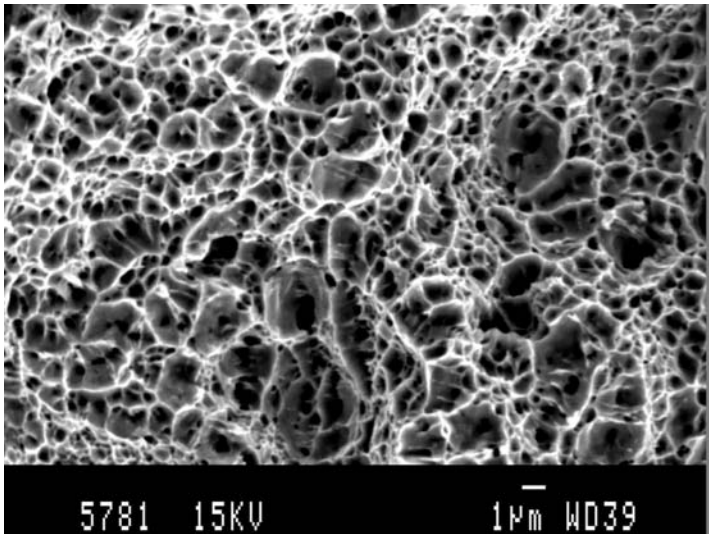

(a)

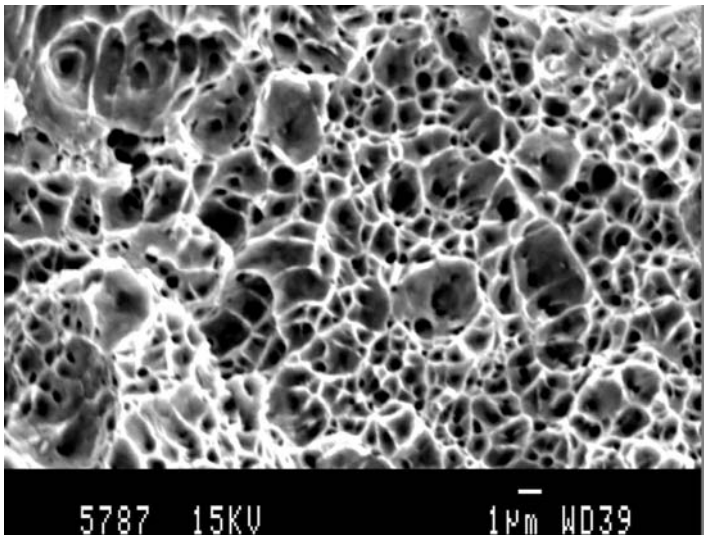

(b)

Figure 3.22: SEM fractographs of tensile tested HSLA-100 steel in different aged condition (a) 650^{o}C and (b) 700^{o}C.

Chapter 4.0

Indirect Assessment of Microstructural Evolution of HSLA-100 Steel

4.0

Indirect Assessment of Microstructural Evolution of HSLA-100 Steel

4.1 Introduction

Steels, which are used as structural materials in various applications like pipe line, rails, bridges etc., is ferromagnetic in nature. HSLA-100 steel posses low carbon and high strength and it is also potential candidate as soft magnetic material for high strength application like in motors etc. Moreover, as magnetic properties change with hardness and microstructure, which are usually altered in a component during extended period of service, magnetic techniques can be used for damage assessment of structural component by non-invasive way. In view of the changes in magnetic properties with structural modification, attempts are now being made to utilise the inherent ferromagnetic properties of steel for evaluation of in-service component's integrity. It is thus necessary to understand the effect of precipitation of the alloying elements on the magnetic properties of HSLA steel to use it either as soft magnetic material or to assess the condition of microstructure of the structural component. Out of all available techniques, Magnetic hysteresis loop (MHL) and Magnetic Barkhausen emissions (MBE) are found to be very promising NDT tools. Magnetic hysteresis loops (MHL) are formed when the amplitude of applied cyclic field crosses a critical value at which the domain wall moves irreversibly. MHL parameters represent the bulk properties of the test material. The magnetic induction curve consists of discontinuous changes

although the field is continuous. Particularly near the coercive point of the material, the magnetic induction curve shows a structure composed of many individual steps, which are caused by the sudden jumping of domain walls from one position to another during magnetisation process. These small steps, which are irreversible changes in magnetisation, are known as Magnetic Barkhausen emission (MBE). MBE signal can be quantified in terms of peak amplitude, rms voltage, number of pulse counts, pulse height distribution etc. Barkhausen emissions are the electromagnetic signal of radio frequency range and hence due to eddy current limitation, MBE represents the surface properties of materials.

In this chapter, the effect of precipitation of Cu in HSLA-100 steel on the magnetic properties has been evaluated and the kinetics of the copper precipitation process has been highlighted using differential scanning calorimeter.

4.2 Experimental Work

4.2.1 Characterisation of HSLA-100 Steel by Magnetic Techniques

Magnetic techniques were used for characterisation of microstructurally engineered HSLA-100 steel. After austenitising at 910^{o}C for one hour followed by water quenching, the material was aged at different temperatures (350^{o}C -700^{o}C) as discussed in Chapter-3. The material softened when aged above 700^{o}C and excluded from magnetic characterisation.

Magnetic hysteresis loop (MHL) and Magnetic Barkhausen emission (MBE) techniques were used to characterise the material. Magnetic hysteresis and Barkhausen emission were carried out using surface magnetising probe. Magnetic hysteresis loop was measured at a quasi-dc (50 mHz) magnetising field whereas the Barkhausen emissions were measured at 40 Hz using a 30kHz-300kHz band pass filter.

4.2.2 Differential Scanning Calorimetric Study

The Cu precipitation behaviour of the steel under study was carried out using differential scanning calorimeter (Perkin-Elmer, DSC-7). The DSC was calibrated using Zinc and Indium sample prior to the experimental run for the specimen. The heating was done in an inert atmosphere at a heating rate of 10^{o}C/min. However, various heating rates were used for activation energy calculation. The broad exothermic peak indicated the formation of nanocrystalline particle. Activation energy for this phase transformation was calculated using Kissinger plot [133].

4.3 Results and Discussion

4.3.1 Variation in Magnetic Properties of HSLA-100 Steel on Ageing

The magnetic hysteresis loop and Barkhausen emission were measured using a surface probe for different heat-treated materials. The coercivity of the materials was plotted in Fig. 4.1a. To see the changes of other magnetic properties, the Barkhausen emission signal has been studied in details for the materials aged at different temperatures. Fig-4.2 shows the Magnetic Barkhausen emission (MBE) waveforms at different ageing temperatures. MBE waveform did not change monotonically and signal became maximum at the intermediate temperature, which was an indication of magnetic softness of the materials. To quantify the Barkhausen signal, the rms voltage of the different samples aged at different temperatures was calculated and plotted in Fig. 4.1b.

Power spectrum of material of various aged conditions showed significant changes when compared to the materials aged at 400^{o}C. The results are shown in Fig. 4.3a to Fig. 4.3g. At the initial stage, i.e. on ageing at 400^{o}C the amplitudes of lower frequency pulses were smaller than the sample aged at 350^{o}C. As the ageing temperature was raised to 500^{o}C (Fig. 4.3b) the amplitude of the lower frequency pulses increased. With further increase in ageing temperature i.e. 550^{o}C and 600^{o}C, considerable increase in amplitude for low as well as high frequency pulses were observed.

The magnetic hysteresis loop and Barkhausen emission study revealed that the material became magnetically softer at the initial stage of ageing as the coercivity decreased. However, when ageing temperature was above 600^{o}C which was above peak temperature (550^{o}C) of the exothermic heat flow for Cu precipitation as observed from DSC curve (Fig. 4.4b), rapid increase in coercivity was observed leading to magnetically harder material. It is to be noted that the initial trend in magnetic softness with ageing in Cu-strengthened HSLA-100 steel contradicted the usual nature of ferritic steel where magnetic hardness increased with the increasing hardness of the materials [123].

To see the changes of other magnetic properties, the Barkhausen emission signal has been studied in details for the different aged materials. MBE waveform didn't change monotonically and signal became maximum at the intermediate temperature, which is an indication of magnetic softness of the materials. To quantify the Barkhausen signal the rms voltage of the different aged samples is calculated. A slow increase in rms voltage is observed upto ageing temperature of 600^{o}C where the coercivity became minimum indicating the magnetic softness of materials. At a higher ageing temperature i.e. above 600^{o}C, rms voltage decreased rapidly showing a decrease in magnetic hardness.

The soft magnetic behaviour observed from coercivity rms voltage of Barkhausen emissions at initial stage of ageing (below 600^{o}C) and the hard magnetic behaviour above 600^{o}C does not obey the usual relationship of soft magnetic and hardness of materials. Usually coercivity increased (rms voltage decreased) with an increase in hardness of materials. In the present case, the hardness increased due to coherent precipitation of nano-sized copper particles. This precipitate size became much smaller than the magnetic domain wall width, which was usually of the order of 30-50 nm depending upon the anisotropic energy and the exchange length of the materials. Hence, domain wall motion was not hindered by the presence of non-magnetic nano-sized Cu-precipitation, which was responsible for increase in hardness (Hv). However, tempering of martensite laths and recovery of acicular ferrite on ageing smoothen the domain wall motion resulting in magnetic softness at the initial stage of ageing. As soon as the size of Cu-precipitate increased and was comparable to domain wall size, the material became magnetically harder as these Cu precipitates started hindering the domain wall motion. The change in MBE voltage around 675^{o}C is due to the formation

of new martensite from reverted austenite, which was also the cause of increase in mechanical hardness of the materials. However, such effect was not observed in coercivity measurement.

Power spectrum of different aged materials showed significant changes when compared to the materials aged at 350^{o}C. The results of power spectrum can be explained by the influence of eddy current generated by Barkhausen signal which are in the radio frequency range. In the present case it is within the range of 30 kHz to 300 kHz which is the frequency of the broad band filter used in the present study. The coherent Cu-precipitation which increased hardness also changed the electrical resistivity of materials. It is expected that the electrical resistivity increased with coherent scattering from the Cu precipitation and decreased when the precipitation become incoherent.

Due to generation of eddy current, the high frequency rf-Barkhausen signal would be heavily damped and was restricted only at the surface region whereas the low frequency pulses could penetrate deeper inside. The scattering of electron from the coherent precipitation of nano-sized Cu particles increased the resistivity of the material in the same fashion as in case of the hardness. The resitivity decreased as precipitation started in an incoherent fashion. The increase of resitivity reduced the eddy current at the initial stage of ageing which increased the amplitude of low and high frequency rf signal of Barkhausen emissions at initial stage (400^{o}C and 450^{o}C) and at the intermediate stage (550^{o}C and 600^{o}C) of ageing respectively. As soon as the precipitate became incoherent at higher ageing temperature, the resistivity as well as hardness started decreasing. Lowering of resistivity increased eddy current formation and hence rf-signal of Barkhausen emissions were damped at high ageing period resulting in a decrease of pulse amplitude at different frequencies. The damping would be more at high frequency compared to the low frequency, which was reflected at the power spectrum of 600^{o}C (Fig. 4.3d). Moreover, size of the precipitate became bigger with ageing period, which restricted the domain wall motion and further reduced the Barkhausen pulse amplitude.

4.3.2 Copper Precipitation - DSC Study

To understand the Cu precipitation kinetics differential scanning calorimetric (DSC) study was carried out with water-quenched sample and exothermic heat flow as a function of temperature has been plotted as shown in Fig. 4.4 together with hardness data**.** Broad exothermic peak with an onset at 400^{o}C was observed. The broad exothermic peak is the characteristics of precipitation of nano-sized particles [209]. The kinetics of the precipitation process has been analysed using modified Kissinger expression. Kissinger plot of Cu-precipitation process is shown in Fig. 4.5a. The time constant of the process was also measured from the Kissinger analysis. The result is shown in Fig. 4.5b.

During initial solution-treatment at 910^{o}C for one hour Cu present within the material is solutionised and α-iron is supersaturated with Cu in water quenched condition. During ageing, precipitation of Cu occurred due to its low solubility (0.2%) in α-iron. Such copper precipitate was observed in TEM study.

The kinetics of the precipitation process has been analysed using modified Kissinger expression relating to the peak temperature (*Tp*), scan rate *(S)* and calculated from equation 4.1:

$$ln(T_p^2/S) = E_{act}/(RT_p)+ln\ (E_{act}/Rk_0) \quad ...(4.1)$$

where, E_{act} is the effective activation energy of the process associated with the peak, R is the gas constant and k_0 is the pre-exponential factor in the Arhenious equation for the rate constant k:

$$k=k_0\ exp\ (-E_{act}/RT) \quad \ldots(4.2)$$

or, the time constant,

$$\tau = 1/k = \tau_0\ exp\ (E_{act}/RT) \quad \ldots(4.3)$$

Combining equations (4.1), (4.2) and (4.3), the simple expression for the rate constant k_p (or time constant τ_p) at a temperature T_p can be obtained as

$$k_p = -(E_{act}/R)\ x\ (S/Tp^2) \quad ...(4.4)$$

or,

$$\tau_p = (R/E_{act})\ x\ (Tp^2/S) \quad \ldots(4.5)$$

The activation energy of the process was calculated using equation (4.1) and found to be 68 kCal/mole. The time constant of the process was also measured from the Kissinger analysis. The result is shown in Fig. 4.5b. Good linear fit (correlation factor, $<r> = 0.9$) with the following expression is observed.

$$ln\ \tau = 34.39x10^3\ 1/T - 37.58 \quad ...(4.6)$$

The stability of the precipitation process at any desired temperature could be obtained using the above equation.

4.4 Conclusions

The coherent precipitation of nano-size Cu took place during ageing (400^{o}C- 550^{o}C) of water quenched HSLA-100 steel after austenitising at 910^{o}C. The hardness and strength of the materials increased due to coherent Cu precipitation. The kinetics of Cu-precipitation was studied using a differential scanning calorimeter and the activation energy was found to be 68 kCal/mol. The magnetic coercivity did not response in the same manner as that of strength and hardness, in contrast to what is usually expected. This may be an advantage for the use of this steel for soft magnetic applications. The material became magnetically softer at the initial stage of ageing which was due to the tempering of lath microstructure. The Cu precipitation did not have much influence on the magnetic softness because of the smaller size of the precipitate compare to the domain wall width. However, the materials became magnetically harder when the size of the Cu-precipitates increased, which hindered the domain wall movement. Barkhausen signal was analysed in the frequency domain and the results were explained by the change of eddy current within the materials due to Cu precipitation.

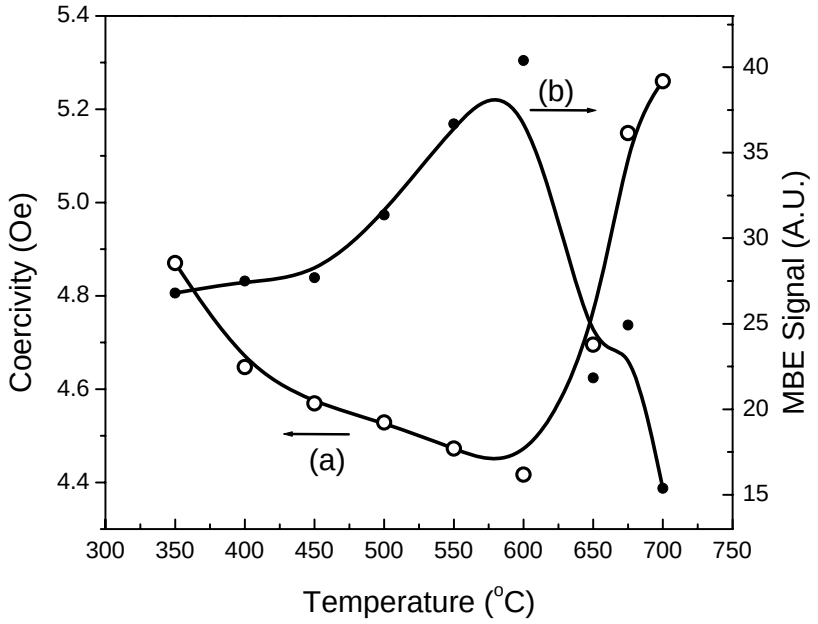

Figure 4.1: Variation of (a) Coercivity and (b) RMS voltage of HSLA-100 steel samples in WQ and aged condition

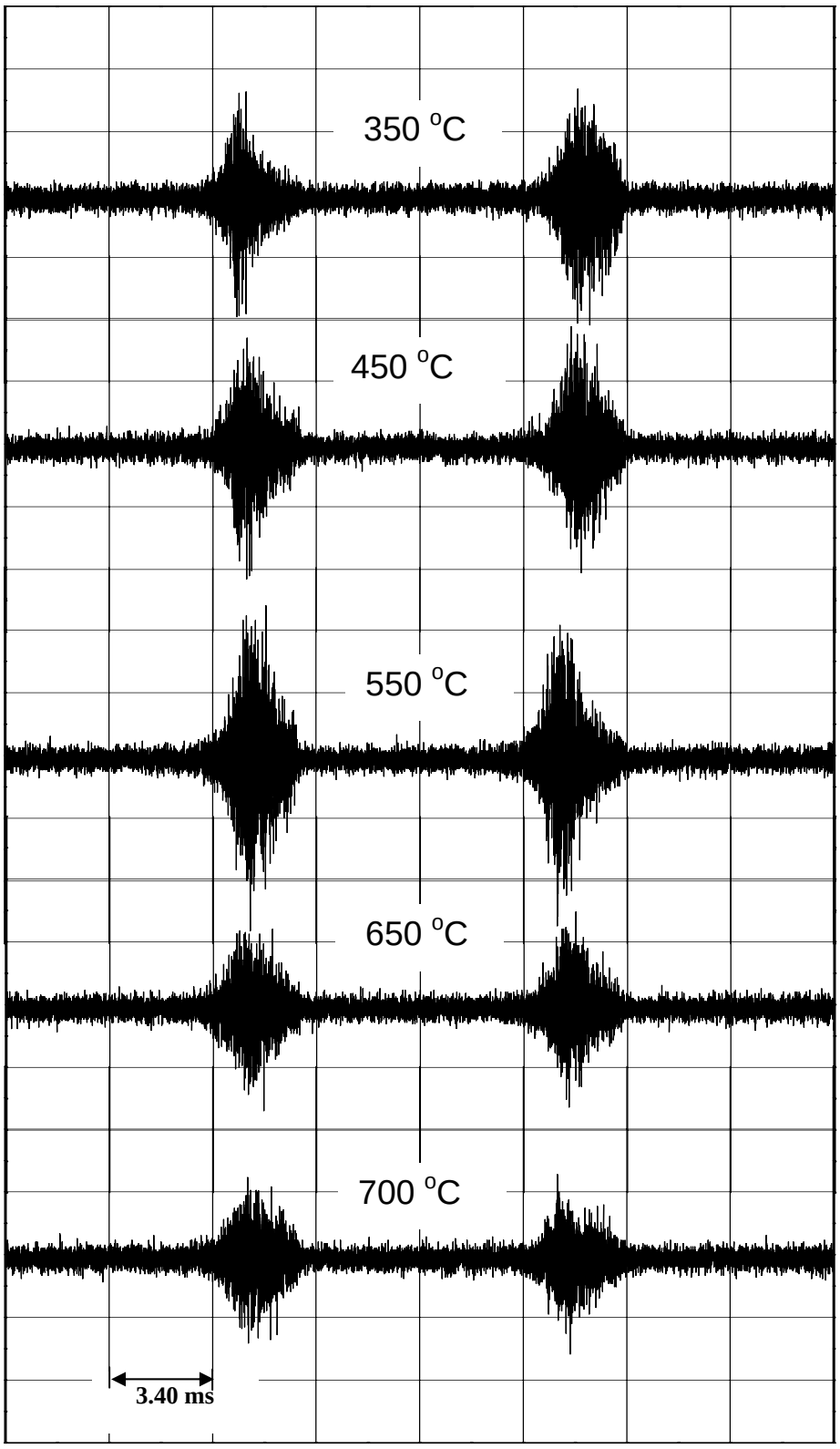

Figure 4.2: Magnetic Barkhausen emission (MBE) waveforms at different ageing temperature

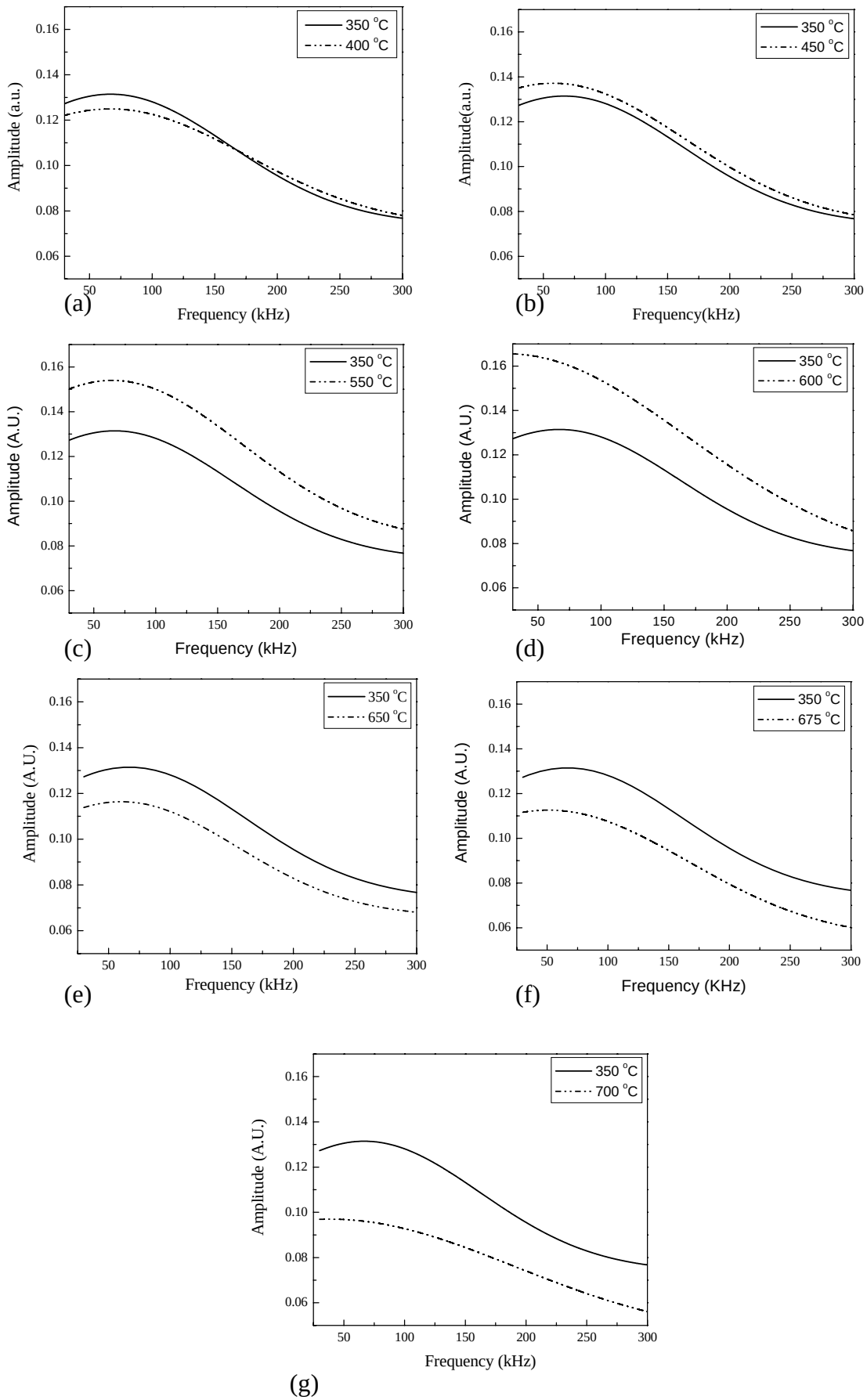

Figure 4.3 a-g: Power spectrum of different aged and WQ samples

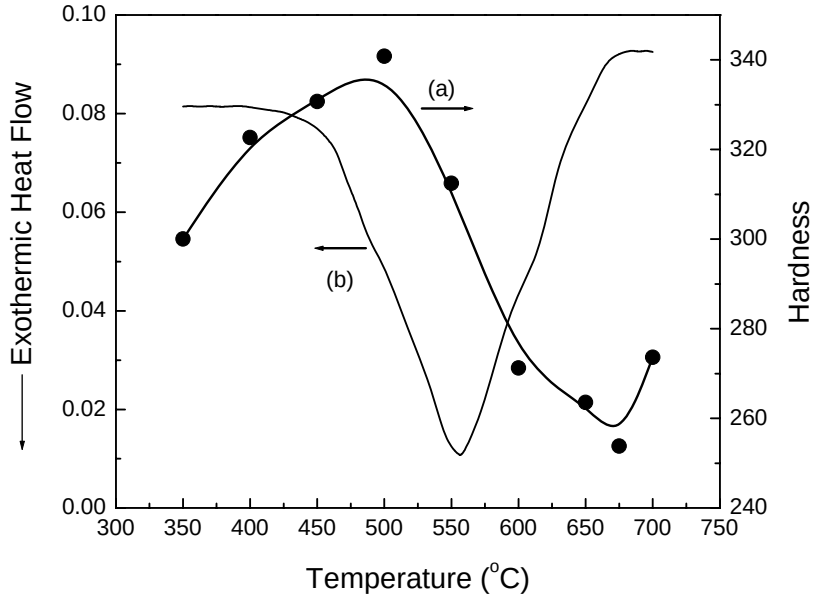

Figure 4.4: (a) Hardness of WQ and aged samples and (b) DSC plot of WQ sample

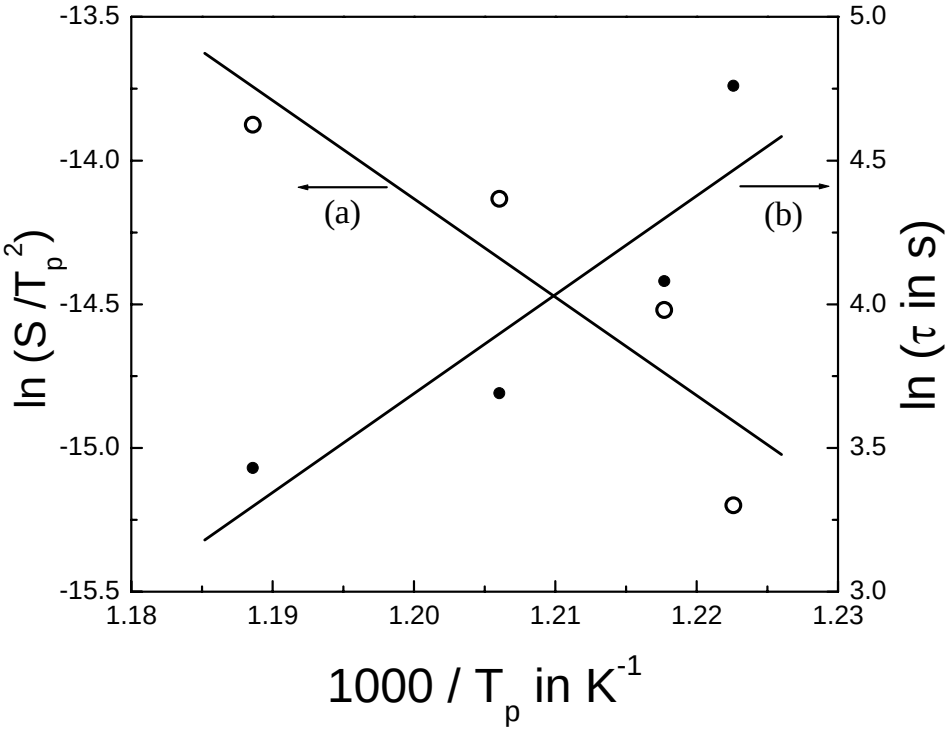

Figure 4.5: (a) Kissinger plot of Cu-precipitation process and (b) time constant of the process.

Chapter 5.0

Fatigue Behaviour of Heat-treated HSLA-100 Steel

5.0

Fatigue Behaviour of heat-treated HSLA-100 Steel

5.1 Introduction

The influence of process parameters and microstructure on the mechanical properties has been discussed in Chapter 2 and Chapter 3. Most literature is confined to characterisation of microstructure and variation in tensile and impact strength [7]. Often evaluation of these mechanical properties is insufficient to characterise the in-depth mechanical behaviour of materials. Characterisation of material behaviour based on fracture mechanics is required for modern engineering design. Sivaprasad et al. [12] have studied fracture and fatigue crack growth behaviour of Cu-strengthened HSLA steels employing the fracture mechanics based approach. However, their study does not include any variation in the microstructural condition. The influence of Cu precipitation and microstructural constituents on fatigue crack growth behaviour of Cu-strengthened HSLA steels has not been explored.

In the present investigation, the influence of various ageing treatment on the fatigue crack growth rate (FCGR) behaviour of Cu-strengthened HSLA-100 steel has been investigated. The microstructure of HSLA-100 steel was engineered through solutionising, followed by water quenching and ageing treatments. The resultant changes in microstructure has been characterised through scanning and transmission

electron microscopy. The variation in the FCGR behaviour has been related to changes in microstructure resulting from ageing treatment.

5.2. Experimental Work

5.2.1 Specimen Preparation

Specimens of 200mm x 50mm x 30mm dimension were cut from the steel plate such that length of the blank is parallel to rolling direction of the plate. These specimens were austenitised for 1 hour at 910^{o}C and water quenched (WQ). The quenched specimens were then aged at various temperatures between 350^{o}C to 700^{o}C in steps of 50^{o}C for 1 hour except a few samples were aged at 675^{o}C. Some specimens were preserved after austenitising treatment to investigate as quenched properties. Single-edge notched bend (SENB) specimens of 150mm (L) x 30mm (W) x 20mm (B) nominal dimensions, were machined from heat-treated samples with the notch in L-T orientation. The specimens were fabricated with integral knife-edges at the notch mouth on which a crack opening displacement (COD) gauge could be fixed for crack length measurement using compliance method.

5.2.2 Fatigue Crack Growth Rate (FCGR)

Fatigue crack growth rate (FCGR) tests were conducted on these specimens in air employing a decreasing ΔK envelope following ASTM standard E-647 [210]. All FCGR tests were carried out at room temperature (28^{o}C) at a load ratio (R) of 0.1. A cyclic frequency of 15 Hz was employed. Duplicate tests were carried for each heat treatment condition and results of two tests were found to be similar.

All tests were conducted in a 100 kN closed loop servo-hydraulic testing machine. The machine was equipped with a digital controller interfaced to a computer for test control and data acquisition. Crack lengths were monitored using compliance technique. Crack mouth displacements for computing compliance were measured using a 5mm length crack opening displacement (COD) gauge fixed on integral knife-edges

machined across the crack mouth. Compliance crack length relation proposed in ASTM standard [210] was used for calculating crack length. The test control software performed on-line crack closure measurements following recommendations of ASTM standard [210]. During FCGR tests, ΔK continuously decreased with crack growth such that ΔK envelope of the tests follows

$$\Delta K = \Delta K_0 \, e^{C(a-a_0)} \qquad \ldots.(5.1)$$

Where ΔK_0 and a_0 are stress intensity factor range and crack length respectively with which test started and C is a constant. The value of which has been standardized at -0.08 mm^{-1}, so that there are no delay effects originating from progressive unloading.

The crack lengths were measured by compliance technique using a COD gauge fitted to load line of the specimen. The software permitted on-line monitoring of the crack length (a), stress intensity factor range (ΔK), effective ΔK (ΔK_{eff}) and crack growth rate per cycle (da/dN). The software used for fatigue crack growth rate (FCGR) testing stored all relevant data like ΔK, da/dN, ΔK_{eff} etc. for further analysis. All specimens were fractured by over-load at the end of the test and the fracture surfaces were examined in a SEM.

5.3 Results and Discussion

5.3.1 Effect of Microstructural Variation on FCGR of HSLA-100 Steel

The fatigue crack growth behaviour of water quenched and aged specimens for entire regime of ΔK studied is shown in Fig. 5.1. The FCGR curves at only a few selected temperatures of ageing are shown in figure for clarity. It may be noted that as the ageing temperature was increased, the crack growth rate of HSLA-100 steel initially increased up to ageing temperature of 500^{o}C. Beyond 500^{o}C, the FCGR gradually decreased up to 650^{o}C. On further ageing, FCGR once again showed an increasing trend. In order to clearly reveal this trend, the Paris slope and Paris coefficient, m and C, were determined from the crack growth data, and in turn they were used to calculate the crack growth rate at any given ΔK (say 20 MPa$\sqrt{m}$) using the relation-

$$\frac{da}{dN} = C\ \Delta K^{\ m} \qquad \text{…. (5.2)}$$

The results are shown in Fig. 5.2 along with variation of strength properties. It may be noted that the variation of fatigue crack growth resistance of HSLA-100 steel follows a variation with temperature of ageing as the mechanical properties.

It is instructive to observe the variation of *m* and *C* with temperature of ageing, as shown in Fig. 5.3. It may be noted that variations in *m* and *C* are inversely related to each other. Peak values are found in the neighbourhood of 500^{o}C, as observed for mechanical properties. However, a reversal of trend beyond 650^{o}C is not exhibited in case of Paris parameters, in contrast to trends observed in the FCGR at a particular value of ΔK and the mechanical properties discussed earlier.

It is interesting to note the correlation between Paris slope *m* and Paris coefficient *C*. As shown in Fig. 5.4, two parameters seem to follow a first order exponential decay relationship. Such direct relationships between constants derived from Paris law is often noticed for tests on the same system which has been varied systematically or where test conditions have been varied systematically [211]. There is merit in consideration that such relationships can be interpolated or extrapolated for determination of fatigue crack growth parameters for any condition of a given system for which limited data are available.

Representative fatigue fracture features of some of microstructural conditions are given in Fig. 5.5. It may be noted that fracture features at WQ and 650^{o}C were observed to be similar. The specimens tested at 700^{o}C showed evidences of secondary modes of failure at local regions. At 500^{o}C, such secondary cracks were found to be more frequent, together with tendencies towards quasi-cleavage modes of failure at isolated regions.

The changes in microstructural constituents and observed fatigue crack growth behaviour appear to have a direct relation. Even though crack initiation resistance of a material would increase with increase in strength, a material with higher strength would provide a poor crack growth resistance. The increase in crack growth rate of HSLA-100 steel during early stages of ageing can thus be attributed to increase in strength of the steel due to formation of coherent copper precipitates. Increase in strength might have

imparted more brittleness and thereby decreasing the propagation resistance of the steel. In the second stage of ageing, loss in strength of the steel due to increasing incoherency of copper precipitates has offered higher resistance for growth of the fatigue crack. Formation of fresh martensite in the third stage of ageing and resulting increase in strength of HSLA-100 steel, once again offered inferior resistance to fatigue crack propagation in this regime. It may be noted that HSLA-100 steel in this investigation is intended for marine structural applications in an optimised heat-treated condition. It is obvious that a study on fatigue crack growth behaviour of this steel under corroding atmosphere is of great importance. Literature is available on corrosion fatigue crack growth behaviour of HSLA steel aged at 680^{o}C [212]. It may be pointed out that this ageing temperature offers a best combination of strength and toughness, which is required for engineering structural applications. The investigation revealed that HSLA-100 steel showed inferior crack growth resistance in 3.5% NaCl solution in comparison to that in air; the reason for this is attributed to repeated film formation and rupture that would expose the bare metal surface in every cycle thereby enhancing the crack growth rate. A reduction in the cyclic frequency is observed to further reduce the crack growth resistance with attendant changes in Paris slope.

A similar influence of microstructural changes on Paris regime FCGR behaviour is reported in Al alloys [213]. The FCGR behaviour of thermo-mechanically treated EN 36 steel weldment and Ti-alloy are also reported [214 - 216] to be affected by ageing treatment. The influence of quench and temper heat treatment on the fatigue crack growth behaviour of a multi phase microalloyed medium carbon steel also shows a strong dependency of FCGR on heat treatment [217]. All these investigations give an indication that the fatigue crack propagation behaviour of engineering structural materials can be affected by the microstructural changes due to heat treatment. The residual stresses that are stored due to heat treatment and the microstructural features that may induce specific slip modes can alter the intrinsic crack propagation behaviour. An in-depth understanding of the correlation between microstructural condition and fatigue crack growth behaviour can be employed for appropriate microstructural engineering for optimal fatigue resistance.

5.4 Conclusions

The microstructural changes due to ageing treatment affect the FCGR behaviour of HSLA-100 steel. Initial ageing treatment ($350^{o}C$-$500^{o}C$) caused a decrease in the fatigue crack growth resistance. This was due to the increase in the strength owing to the formation of coherent ε-copper precipitates. Ageing above $500^{o}C$, caused a recovery in the fatigue crack growth resistance. This was due to the loss of coherency and growth of Cu-precipitates. Ageing at $700^{o}C$, results in formation of fresh martensite islands occurred and this in turn caused a decrease in the fatigue crack growth resistance. The observed variation in the FCGR behaviour was similar to the nature of variation of strength properties with ageing treatment.

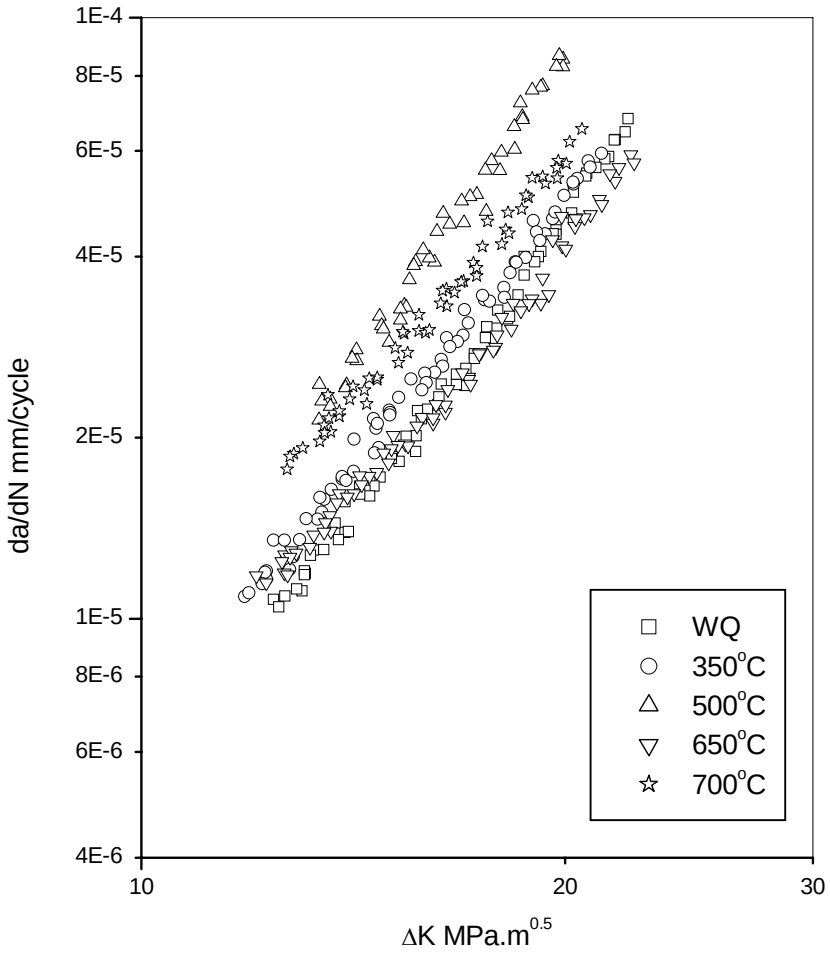

Figure 5.1: The *da/dN* vs. *ΔK* plots of steel showing the fatigue crack growth behaviour of water quenched and aged specimens

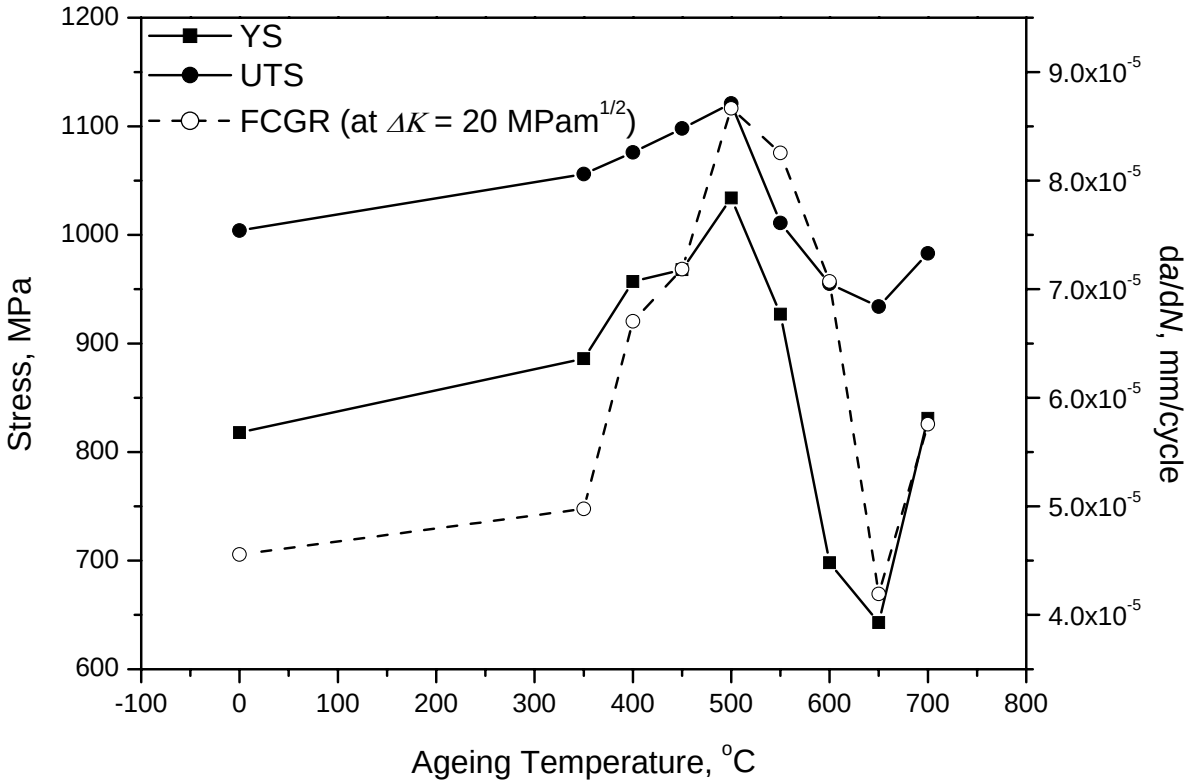

Figure 5.2: Variation of strength properties and fatigue crack growth resistance with ageing temperature in HSLA-100 steel

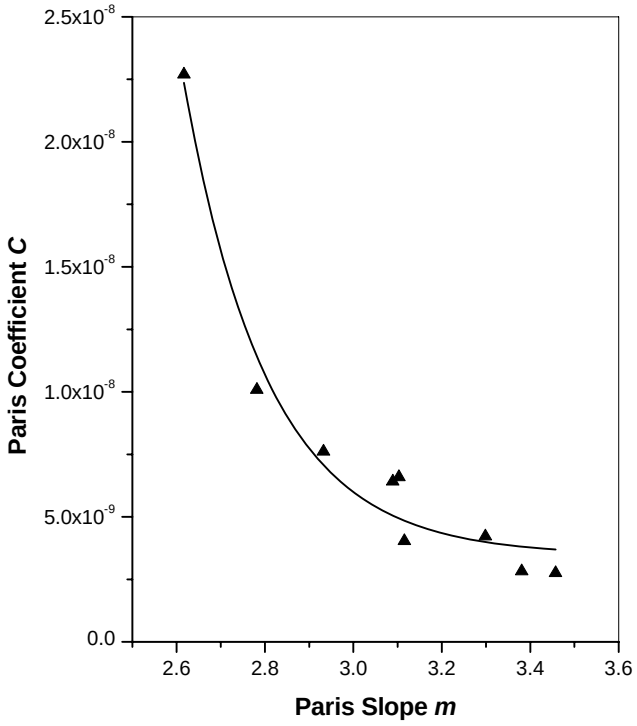

Figure 5.3: Variation of Paris parameters, obtained from the FCGR data, with temperature of ageing

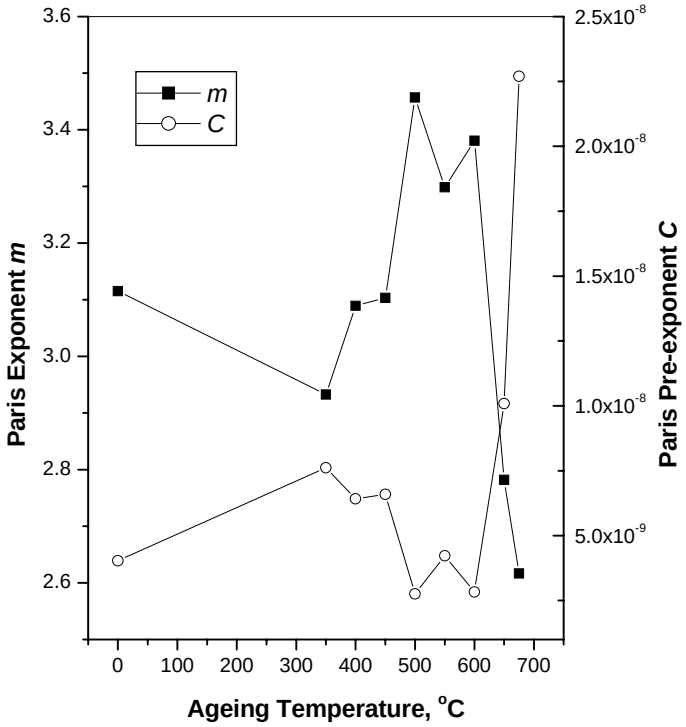

Figure 5.4: Correlation between *m* and *C* obtained from FCGR curves for various microstructural conditions

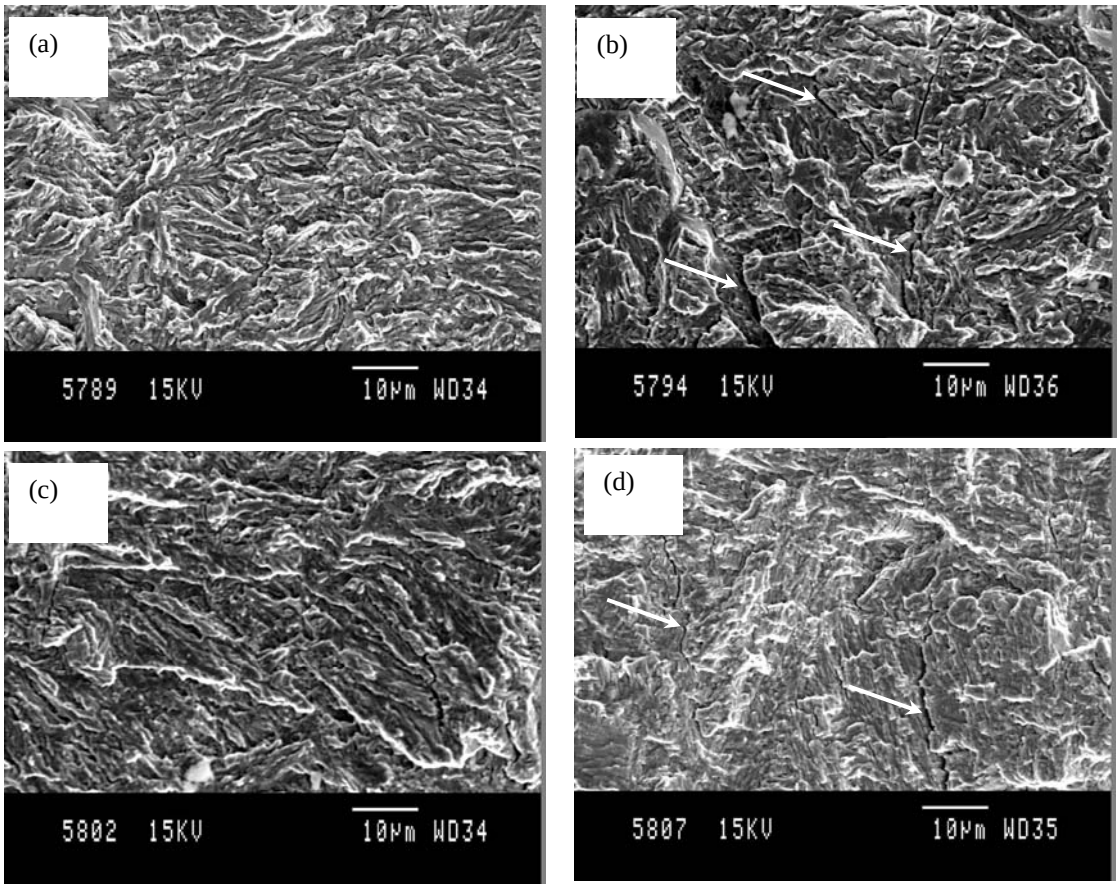

Figure 5.5: SEM fractographs of FCGR test specimens – (a) WQ condition (b) aged at 500^{o}C (c) aged at 650^{o}C and (d) aged at 700^{o}C. Secondary modes of failure are shown with arrows

Chapter 6.0

Effect of Microstructures of HSLA-100 Steel on Fracture Mechanics Parameters

6.0

Effect of Microstructures of HSLA-100 Steel on Fracture Mechanics Parameters

6.1 Introduction

The indirect appreciation of the effect of microstructure of HSLA-100 steel as described in earlier Chapter-3, although providing engineering leverage in comparative assessments, is somewhat empirical in nature. Microstructures exhibiting the same hardness may contain completely different combination of phases that in totality provides the same resistance to deformation by an indenter. However, they may not be the same resistance to fracture. It is therefore imperative to develop a deeper understanding of the effect of different microstructure and microstructural constituents, on fracture behaviour and the effect of microstructure on fracture mechanics parameters.

The important parameters used for characterising fracture behaviour that are derived within the framework of fracture mechanics include (i) pre-exponent and exponent of the Paris curve that is used to describe fatigue crack growth rates (FCGR) (ii) fracture toughness in the linear-elastic and elastic-plastic fracture mechanics regimes, based on the stress intensity factor, K, and the energy parameter J-integral respectively (iii) tearing modulus, T, defined as the slope of the J-resistance curve for ductile fracture (iv) blunting-line slope, M, and (v) related fractographic manifestation of the stretch zone. It would be interesting and instructive to study and understand how

these parameters are influenced through a variation of microstructure. It may be noted that the fracture mechanics parameters are known to be influenced by not only microstructure, but also the environment, the stress triaxiality and the geometry of engineering components. However, while other parameters can be quantified, or at least specified, unequivocally, the same is often not true for microstructure.

The effect of microstructural variation of HSLA-100 steel on FCGR has already been discussed in Chapter-5. In this chapter, variations in the *J-R* curve, blunting-line slope, tearing modulus and the stretch zone width (SZW) has been reported for systematic variation of microstructures in Cu-strengthened HSLA-100 steel. Variations in the microstructure of the steel have been incorporated through ageing at various temperatures after an initial quenching treatment. Descriptions of the various microstructures have been obtained through detailed scanning and transmission electron microscopy. These have been used to understand the variations in mechanical properties and in fracture mechanics parameters obtained through standard tests.

6.2 Experimental Work

6.2.1 Specimen Preparation

Single-edge notched three-point bend specimens, of 150mm (*L*) x 30mm (*W*) x 20mm (*B*) nominal dimensions, were employed for fracture toughness testing. Specimens were fabricated with integral knife-edges at the notch mouth on which a crack opening displacement (COD) gauge was fixed for crack length measurement using the compliance method. All tests were carried at room temperature (28^{o}C). Fractographic observations were carried out in JEOL JSM 840A SEM.

6.2.2 Fracture Toughness Evaluation

The single-specimen method was employed for carrying out fracture toughness tests as per ASTM standard E-1820 [218] with the primary objective of obtaining *J-R* curves. *J*-integral tests were carried out to study fracture behaviour of the microstructurally engineered HSLA-100 steel. Figure 6.1 is the schematic diagram of the three-point bend (TPB) specimen machined as per ASTM standard E-1820. All specimens were pre-cracked to a/W = 0.5 in a EMR machine at 75 Hz frequency. Tests were conducted in a 100 kN Instron servo hydraulic testing system equipped with a digital controller that was interfaced to a computer for test control and data acquisition. A displacement rate of $3x10^{-3}$ mm/s was used for imposing a loading scheme (Fig. 6.2) consisting of concatenated sequences of loading through 0.3 mm, followed by partial unloading through 0.15 mm and reloading through the same amount, repeated continuously till sufficient crack growth took place. A 10 mm COD gauge was used for Load-Line-Displacement (LLD). The load on specimens, crosshead displacement and crack opening displacements were constantly monitored throughout the test. Software was used for test control and data acquisition and the raw data was analysed off-line to get the load–load line displacement (P-LLD) and *J-R* curve as per ASTM E-1820.

6.2.3 Stretch Zone Imaging

The widths of stretch zones spanning the culmination of pre-fatigue cracks and the initiation of ductile fracture were quantified from SEM fractographs for correlation with ductile fracture behaviour. The specimens were post fatigue cracked at room temperature at the end of each *J*-integral test. Then fracture surface of the tested specimen was cleaned in a ultrasonic cleaner before examining them in a scanning electron microscope (JEOL JSM-840A). The mode of failure and prominent features were recorded in digital electronic format. Fractographs were also recorded for each specimen at the location of initiation of ductile crack and were recorded at different tilt angles to analyse the nature and dimensions of the stretch zones.

6.3 Results and Discussion

6.3.1 Effect of Microstructural Variation on *J-R* Curve of HSLA-100 Steel

The different load-load line displacement curves were obtained from the *J*-integral test for differently aged & WQ specimens. A typical load-COD displacement curve for WQ specimen is shown in Fig. 6.3.

From the load-load line displacement plots, different *J-R* curves were obtained for specimens at differently aged conditions. To get the ductile fracture toughness value from the curve, a best-fit line is constructed to the initial linear region of the data as per the equation:

$$J = M\,\Delta a\,\sigma_0. \qquad \ldots.(6.1)$$

Where, J = *fracture toughness*, M = blunting line slope, Δa = crack extension, σ_0 = flow stress

A cubic fit line is constructed to the rest of the data to get the intersection point which is the initiation fracture toughness (J_i).as per the equation:

$$J = C_1 \Delta a^{C_2} \qquad \ldots.(6.2)$$

Where, C_1 and C_2 *are* the pre-exponent and exponent of the tearing curve respectively.

To avoid any confusion in correctly identifying this deviation point, the linear line is offset to 0.2 mm crack extension and takes this intersection point as ductile critical fracture toughness (J_{IC}) as shown in Fig. 6.4.

Variation in blunting line slope (slope of the initial linear region in the *J-R* curve) with change in ageing temperature is shown in Fig. 6.5. The slope first increased, then decreased and again increased with ageing temperature. There are absences of data points in between 350^oC–500^oC because of total brittle crack extension/pop-in-behaviour of the material. The variation of co-efficient in the tearing region also shows

similar trends (Fig. 6.6). The J_i and J_Q also vary with the ageing temperature. Figure 6.7 shows the variation of J_i, J_Q and J_u as a function of ageing temperature.

From the fracture toughness tests, it was apparent that most of the samples on ageing at various temperatures displayed *R*-curve behaviour. The samples aged at 400^{o}C to 500^{o}C were exceptions, in which crack instability was observed at early stage on loading. The *J-R* curves that could be obtained by analysing the test data as per the procedures laid down in ASTM standard E-1820 [218] are shown in Fig. 6.8. The load-displacement data obtained for the peak-aged conditions are given in Fig. 6.9, clearly indicate their brittle characteristics of fracture. Fig. 6.8 and Fig. 6.9 reveal that the fracture resistance of HSLA steel can be altered through a large range through changing its microstructure by selecting the ageing temperature. It may be noted that the fracture resistance is at a moderate level in the WQ condition, and further suffers a drastic embrittlement at ageing temperatures up to 500^{o}C, with acute fracture instability. It is surprising to note that the recovery of the *J-R* curve of the sample on ageing at 550^{o}C, maintained equivalent levels for the samples aged at temperatures up to 675^{o}C. It appears that on ageing at 700^{o}C, large increase in resistance of the material to fracture occurs.

A comparison based on the shape of *J-R* curves can often be misleading, and it is appropriate to make assessments based on the critical fracture toughness parameter. Accordingly, the critical initiation toughness J_{i} and the (unqualified) critical fracture toughness at 0.2mm ductile crack extension J_{Q} was obtained using the procedure of ASTM standard E-1820 [218], through the definition of a best-fit blunting line and employing a power curve to define the tearing region.

Beyond the requirement of the standard, the procedure was implemented in an iterative scheme so that the critical values and other parameters of the *J-R* curve were progressively refined until they converged. Fig. 6.10 shows the iterated blunting line fits and tearing curves were obtained for some of the microstructural conditions. For the microstructural conditions exhibiting fracture instability (i.e. ageing at 400^{o}C, 450^{o}C and 500^{o}C), and for which critical parameters could not be obtained through the *J-R* curve route, the critical fracture parameter J_u was derived considering the elastic energy and plastic work from the load-displacement plots using the basic equation for the calculation of *J*-integral.

The variation of fracture toughness with change in microstructure of HSLA steel on ageing at various temperatures is shown in Fig. 6.7. It can be seen from the figure that fracture toughness value of the water quenched condition falls sharply when aged at 500^{o}C, increases again considerably when aged above 500^{o}C. In contrast to the behaviour of mechanical strength properties, and in similarity to the observation for fatigue crack growth parameters *m* and *C*, there does not appear to be a sharp reversal of trends at the ageing temperature of 650^{o}C. In fact, there seems to be a direct correlation with the variation shown by the reduction in area for tensile specimens.

The fracture toughness values obtained for specimens that exhibited fracture instability appear to fall along the trend for ductile fracture specimens. The somewhat higher fracture toughness calculated for ageing at 450^{o}C is due to the fracture instability manifesting itself after a small amount of stable crack extension, as evident from the load-displacement plot in Fig. 6.9, in contrast to fracture instability prior to stable crack growth for ageing at 400^{o}C and 500^{o}C. The extent of stable crack extension at fracture instability for 450^{o}C ageing is probably of the order of 0.2mm, since the data point for this condition aligns well with the J_Q points.

The lowest fracture toughness value obtained in samples on ageing at 500^{o}C is due to the precipitation of coherent nano-size Cu particles. The increase in fracture toughness value occurs on ageing the samples beyond 500^{o}C are primarily due to the loss of coherency of Cu precipitates rather than softening and degeneration of the matrix through tempering effects. The sudden toughening exhibited at 550^{o}C is difficult to explain without invoking the fact that loss of coherency is apt to be sudden. The asymptotic rise in fracture toughness as the ageing temperature is increased above 650^{o}C is no doubt primarily due to the formation of reverted austenite and new martensite islands, since this is an additional factor in the process of microstructural evolution in this range of temperature. The martensite-austenite combination effectively acts as a local composite entity and toughens the material through resisting easy propagation of cracks.

It is interesting to study the variation of characteristics of the *J-R* curve, like the blunting slope *M* (obtained from the relationship $J = M.\sigma_0.\Delta a$ and fitted to the initial

linear region) and the pre-exponent and exponent of the tearing curve when expressed in the power-law equation 6.2.

Figures 6.5 and 6.6 show respectively their behaviours as a function of ageing temperature. In Fig. 6.5, *M* is found to be mostly below 2, which is conventionally thought to be the lower-limit of the blunting-line slope (earlier versions of ductile fracture toughness testing standards, for e.g. ASTM E 813 preferred this value) [219]. This is quite contrary to typical observations on ductile materials that show excellent toughness where it is customary to obtain blunting-line slopes as high as 8 [220]. The variation of *M* is within a very small range and it is believed that the actual trend in this range is not important and should not be interpreted as an effect of variations in microstructure on ageing. The rising nature of *M* may however be noted for increasing toughness on ageing from 550^{o}C to 700^{o}C. From Fig. 6.6, it can be seen that the value of C_2 is quite insensitive to changes in microstructure, while that of C_1 responds predominantly. C_2 reflects the shape of the tearing curve, which is similar for all cases of ductile fracture as seen in Fig. 6.10, and therefore it is not surprising to find that it does not change much with ageing. C_1, on the other hand, is the amplification factor that scales the *R*-curve, and since there is considerable change in fracture toughness with ageing, C_1 is liable to respond accordingly. An increasing trend is again observed with increasing fracture toughness as the ageing temperature is elevated.

6.3.2 Stretch Zone Width and Fracture Toughness of HSLA-100 Steel

The importance of SZW as a parameter for characterising the fracture toughness of materials should be considered. The SZW has been the subject of active consideration [221,222], and its measurement has been introduced into the JIS standard and is incorporated in the ESIS procedure for measurement of fracture toughness. The stretch zones as seen on the fracture surfaces of specimens are shown for a selection of microstructural conditions of HSLA steel in Fig. 6.11. It may be noted that for all ageing conditions, including those displaying fracture instability, the SZW could be readily identified. In fractographs (Fig. 6.11), the boundaries of the stretch regions are manually delineated to facilitate measurement. Identification of the boundary of stretch zone features is somewhat subjective, and errors may accrue into measurement from

this. On-line viewing of the fracture surface in the SEM, manipulating the specimen to gain a better insight of the elevation and details of the features, often facilitates the process. It is apparent that SZW is not uniform along the crack front, and a number of measurements are required in order to arrive at an average value. It is also recommended that measurements should be made on both halves of specimens since the fracture initiating from a blunted crack tip may not be symmetrical. The fractographs in Fig. 6.11 has been obtained at a magnification of 400x. Fractographic observation at lower magnifications, although incorporates a larger fraction of the specimen thickness however does not provide enough details to identify the boundaries accurately.

For quantitative analysis, the SZW was measured at 30 locations spanning a few fractographic frames at the centreline of the specimens for the various aged conditions. The average measurements are plotted in Fig. 6.12 as a function of the ageing temperature. It is interesting to observe that SZW of the samples on ageing at various temperatures remains almost constant including at ageing temperatures for which fracture instability prior to extended stable crack growth was observed. The near constancy of SZW is particularly apparent when compared alongside the critical crack extension at fracture initiation $\Delta\alpha_{\text{critical}}$, measured at the intersection of the blunting line and the tearing line for *J-R* curves, which is also plotted in Fig. 6.10. In the narrow range of evidently random variation of SZW, a slight increase in value may be obtained as the fracture toughness of the material improves with temperature of ageing, but this may not be significant considering the errors involved in measurement. With reference to Fig. 6.12, one fact that is glaringly evident is the difference between the $\Delta a_{\text{critical}}$ and SZW. Except for the microstructural condition for ageing at 350^{o}C (and perhaps for 400^{o}C, 450^{o}C and 500^{o}C also since fracture was significantly brittle for all these conditions and for which $\Delta a_{\text{critical}}$ data is not available), $\Delta a_{\text{critical}}$ always overestimates the SZW. This indicates that either the procedure for obtaining the blunting-line from the test data is grossly inappropriate, or the concept of crack blunting through stretching followed by initiation of stable (or unstable) crack extension that is used to model fracture behaviour is totally inaccurate.

6.4 Conclusions

From the study carried out, it was possible to develop an appreciation of the role played by microstructural constituents in controlling the fracture behaviour of HSLA-100 steel that has been quenched and aged. The major role played by the coherency of Cu precipitates is in restricting plastic flow, thereby limits the potential for initiation and growth of microvoids that are responsible for ductile fracture. The recovery of the background matrix and loss of coherency of Cu precipitates and its effect on fracture mechanics parameters was also observed. The evolution of reverted austenite and small martensite islands in the microstructure on ageing was responsible for a desirable combination of high strength and high toughness in the steel, and can be exploited to develop suitable microstructures for critical engineering applications. Following conclusions are made from the study-

(i) J_c decreases but SZW remains constant when specimen was aged between 350-500^{o}C,

(ii) J_c increases and there is an apparent trend of increasing M and C_1, whereas SZW remains constant when specimen was aged between 550-650^{o}C,

(iii) J_c continue to increase and there is an definite increasing trend for M, C_1, C_2, SZW when specimen aged between 675-700^{o}C

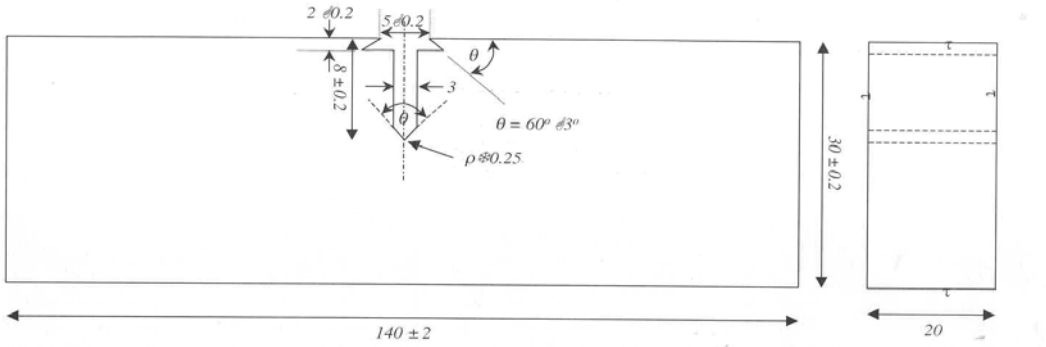

Figure 6.1: Schematic representation of three point bend (TPB) specimen for *J*-integral test.

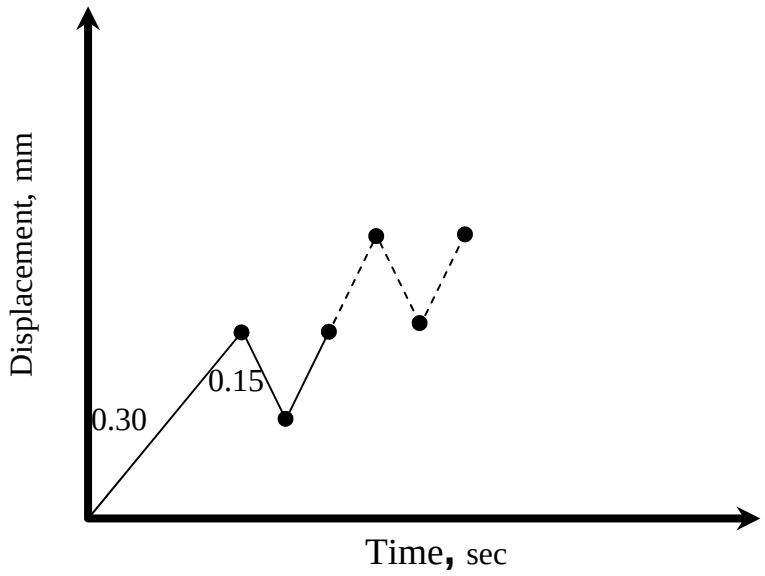

Figure 6.2: Schematic representation of the loading scheme used for *J*-test.

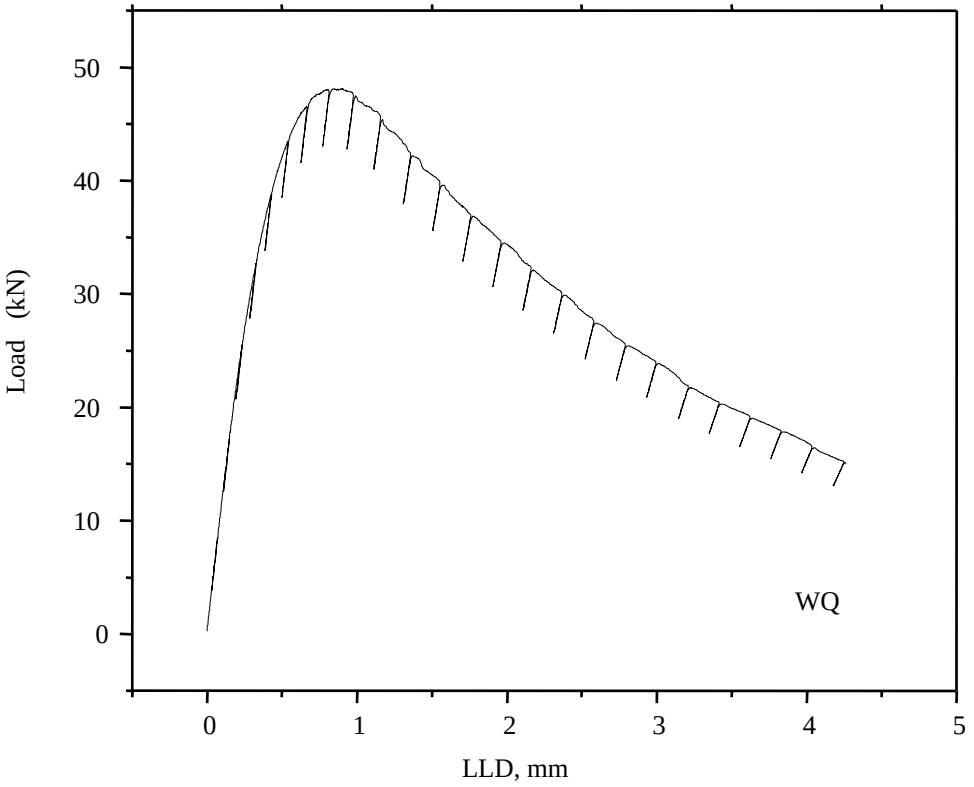

Figure 6.3: Load-Load Line Displacement plot for WQ specimen.

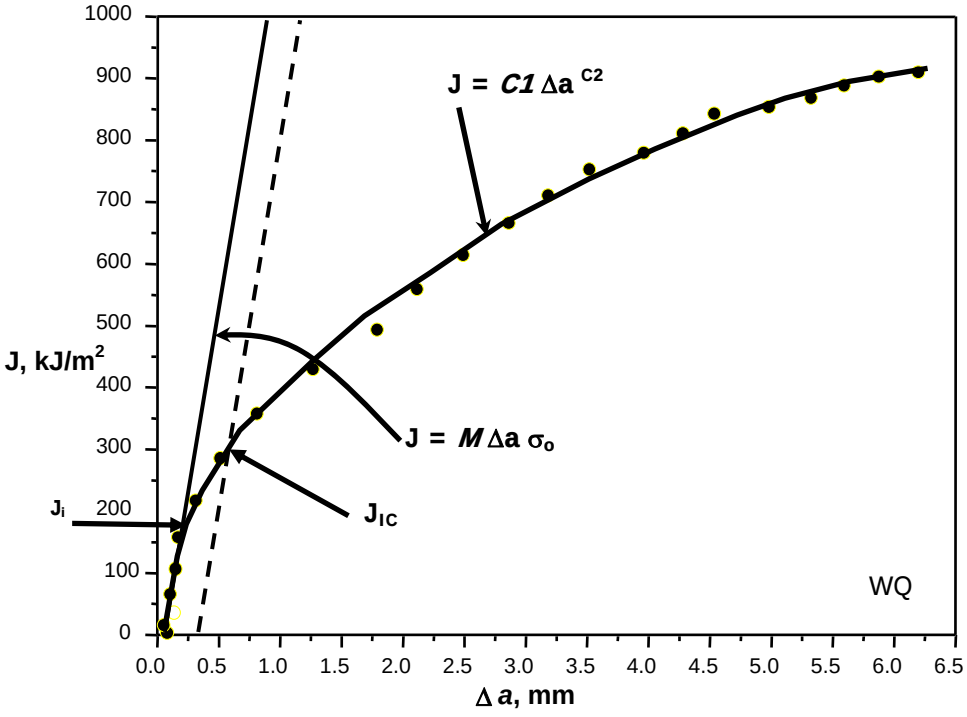

Figure 6.4: *J-R* curve for WQ specimen

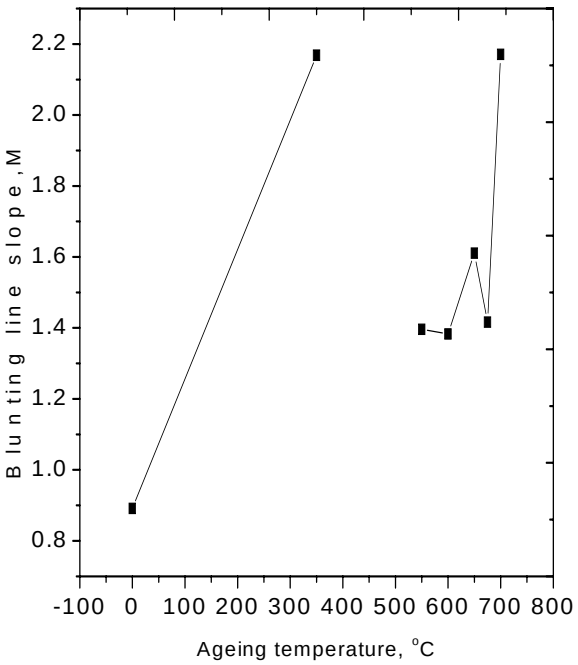

Figure 6.5: Blunting line slope vs. ageing temperature

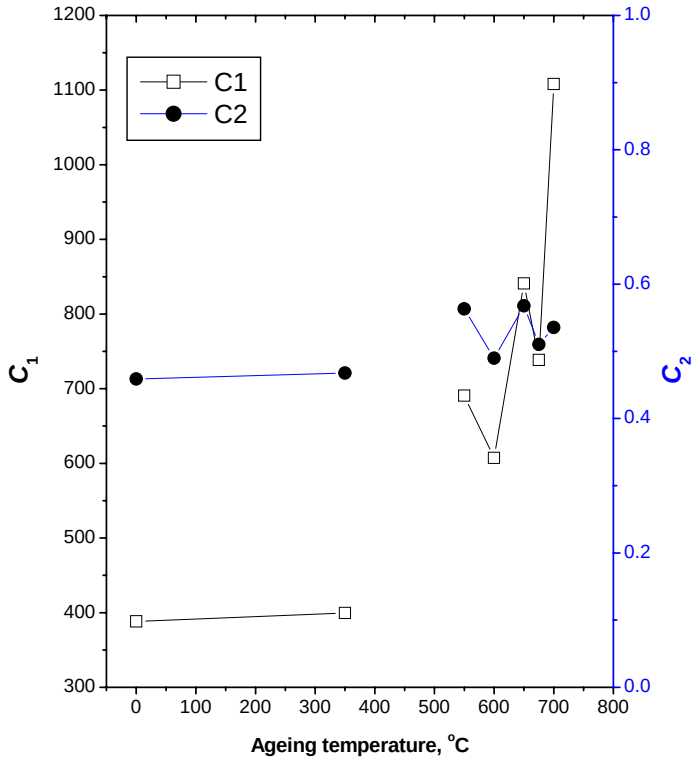

Figure 6.6: Tearing co-efficient (C_1 & C_2) as a function of ageing temperature

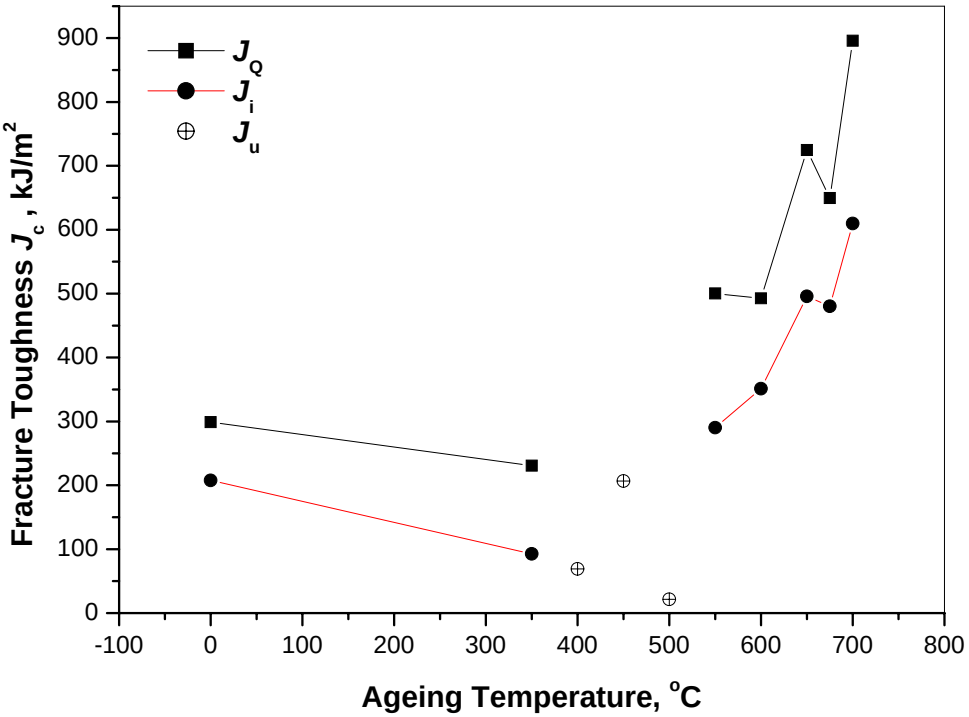

Figure 6.7: Variation of fracture toughness J_c of HSLA-100 steel with ageing temperature.

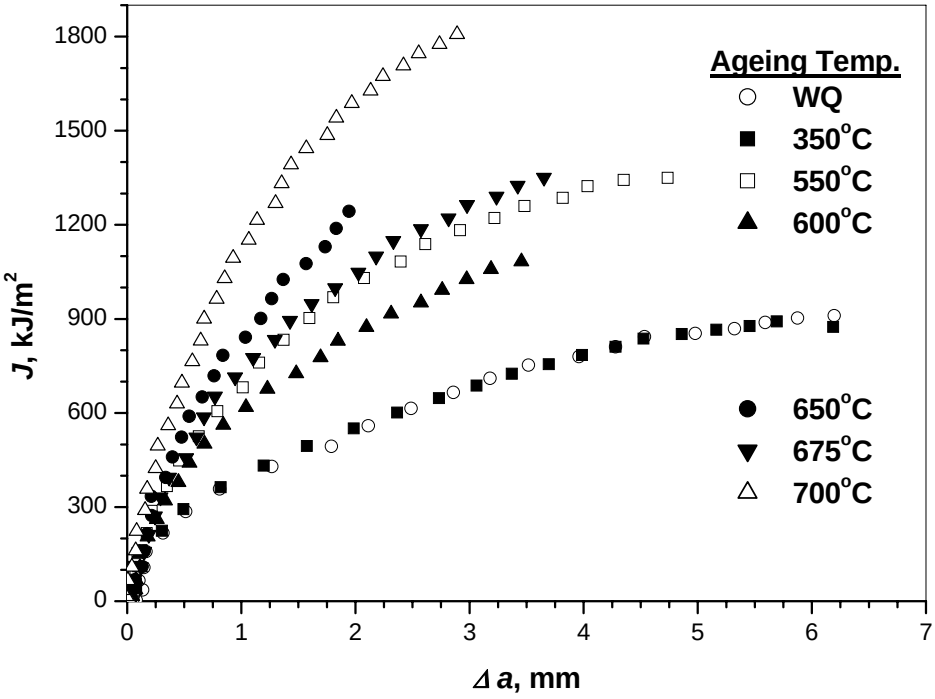

Figure 6.8: *J-R* curves of HSLA steel, water quenched and aged at various temperature

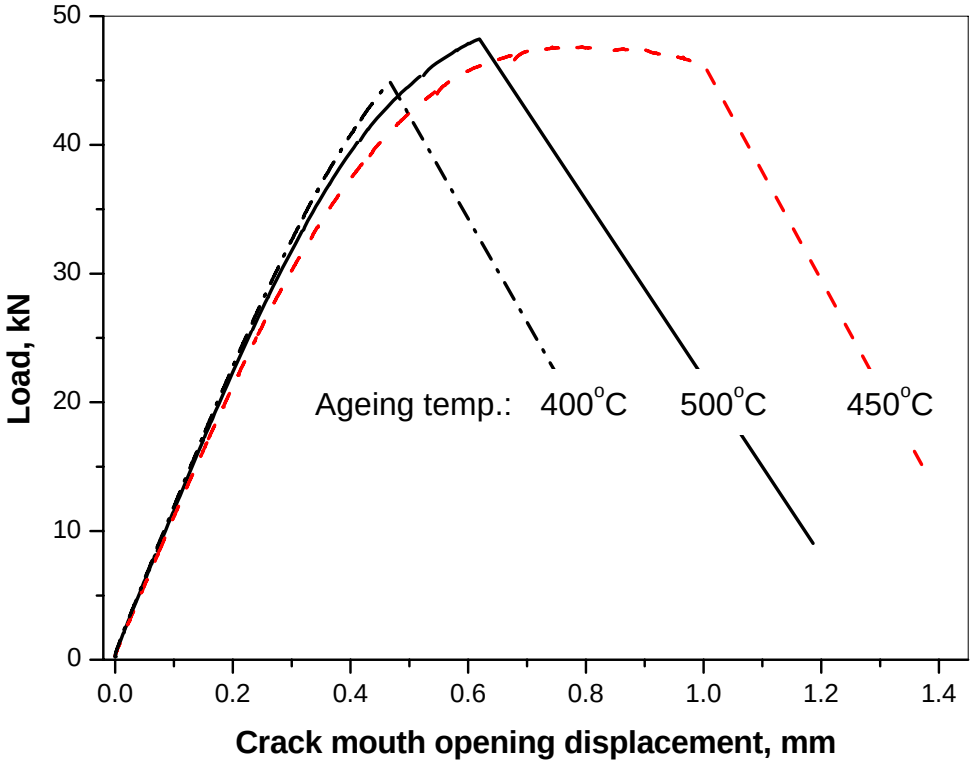

Figure 6.9: Load-displacement characteristics of HSLA microstructures that display fracture instability

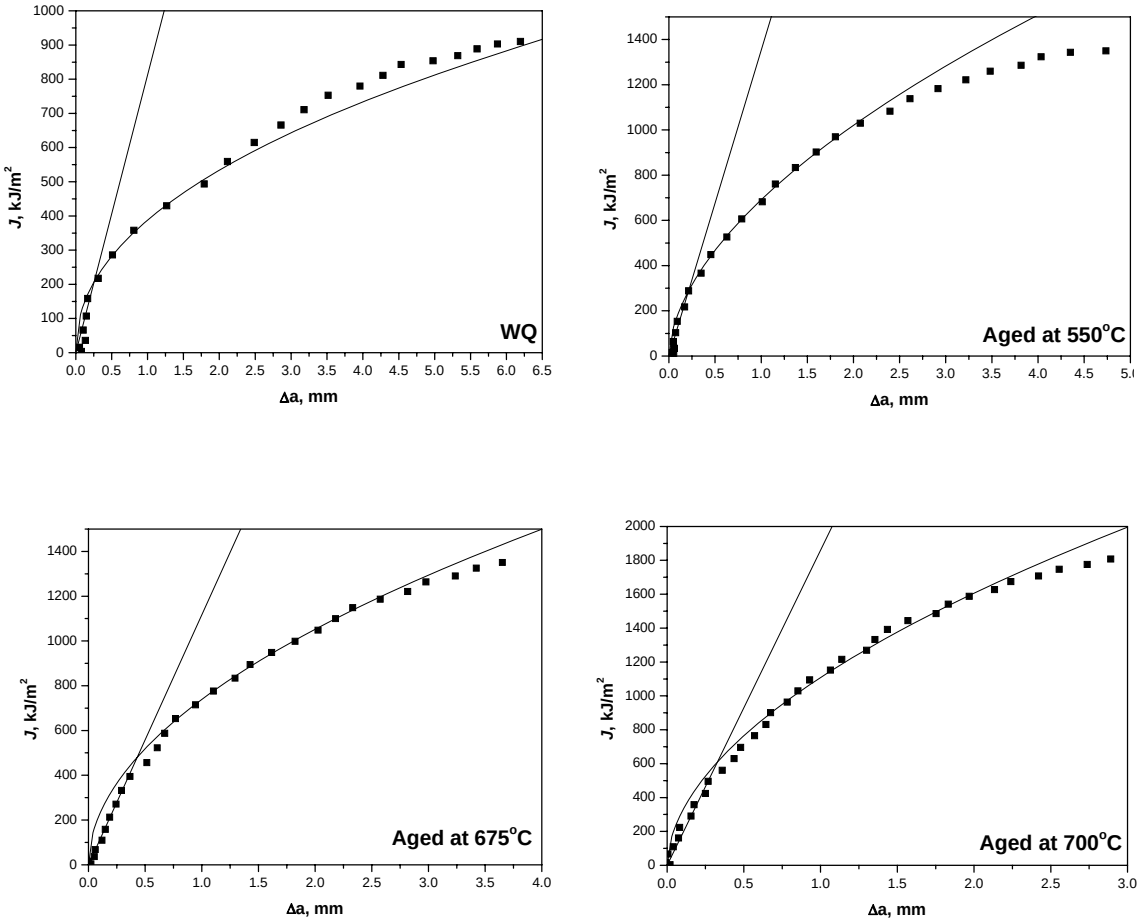

Figure 6.10: Blunting line and tearing curve fit to *J-R* curves for selected heat-treated HSLA steel specimens

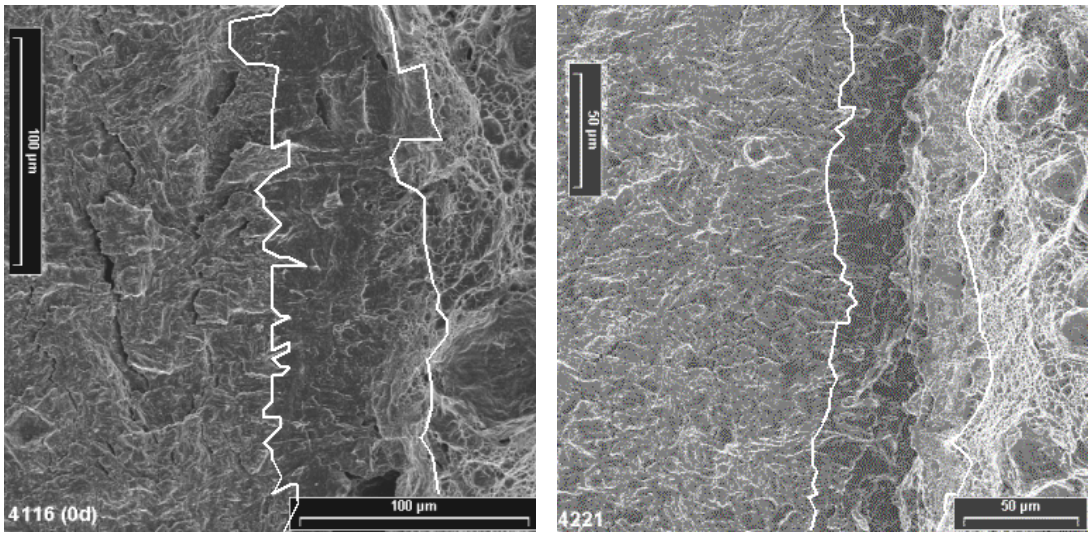

(a) (b)

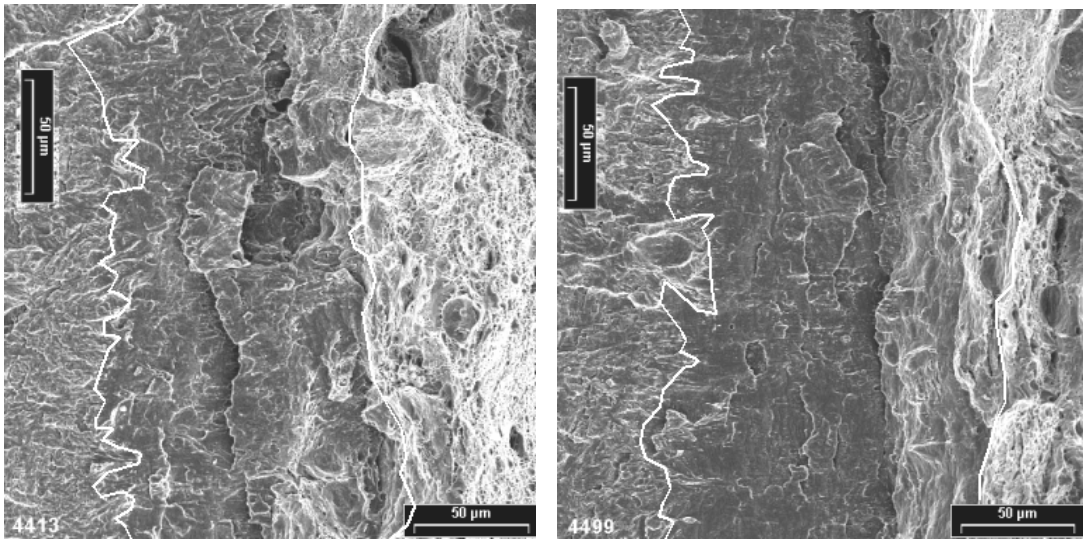

(c) (d)

Figure 6.11: Fractographs of HSLA-100 steel variously aged, showing the stretch zone region (a) WQ, (b) aged at 500^{o}C, (c) aged at 550^{o}C and (d) aged at 700^{o}C. The boundaries of stretch features are delineated.

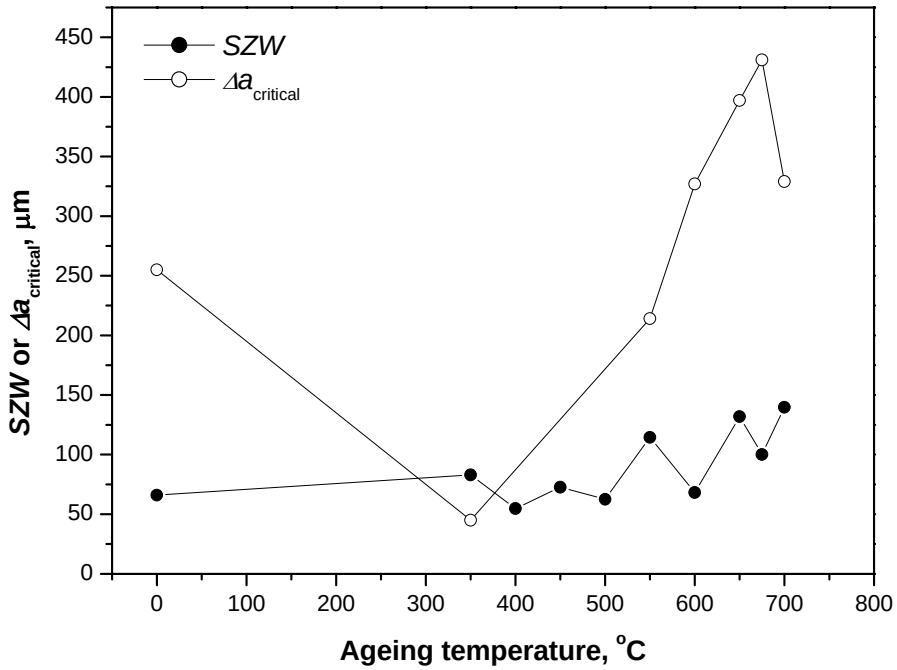

Figure 6.12: Variation of the SZW with temperature of ageing for HSLA steel. The critical crack extension at fracture initiation, as measured from *J-R* curves is also superimposed in the figure

Chapter 7.0

Summary and Conclusions

7.0

Summary and Conclusions

Microstructure of HSLA-100 steel used in this study consists of lath martensite, acicular ferrite and bainite in water-quenched condition. Small amount of retained austenite along with microalloying carbides & carbo-nitrides have been observed in the microstructure. On ageing, transformation of acicular ferrite to polygonal ferrite and recovery of martensite lath occurred. Precipitation of coherent Cu rich particles has also been observed on ageing at 400^{o}C. Nano-size coherent Cu precipitates gradually coarsened and lost coherency on ageing beyond 550^{o}C due to growth of fcc Cu precipitates. However, there was no change in shape & size of microalloying carbides and carbonitrides due to ageing below 700^{o}C for one hour.

Two types of micromechanism of fracture plays role during tensile fracture- (i) micro-cleavages are dominant in specimens on ageing between 400^{o}C–500^{o}C and (ii) initiation, growth and coalescence of microvoids are predominant for specimens on ageing beyond 550^{o}C. The plastic flow of material is restricted in the initial stage of ageing due to precipitation of very fine coherent Cu-rich particles and leads to an increase in brittleness and strength at the expense of ductility of material. The hardness of material also increases due to precipitation of coherent Cu particles. On ageing at higher temperatures, these precipitates coarsen and loose their coherency and facilitate an increase in ductility and flow of material.

The kinetics of Cu-precipitation was studied using a differential scanning calorimeter and the activation energy was found to be 68kCal/mol. The magnetic

coercivity didn't response in the same manner by an increase as that of mechanical strengthening induced by Cu precipitates, in contrast to what is usually expected. This may have an advantage for the use of this steel for soft magnetic applications. The material became magnetically softer at initial stage of ageing, which was due to tempering of lath microstructure. The Cu precipitation didn't have much influence on magnetic softness due to smaller size of precipitate in comparison with the domain wall width. However, the materials became magnetically harder when the precipitate's size increased, which ultimately hindered the domain wall movement. Barkhausen signal was analysed in the frequency domain and the results were explained in the light of change of eddy current within material due to Cu precipitation.

The microstructural changes due to ageing treatment strongly influence FCGR behaviour of HSLA-100 steel. Ageing treatment in the temperature range of 350^{o}C-500^{o}C caused a decrease in fatigue crack growth resistance. This was due to increase in strength owing to formation of coherent Cu precipitates. Ageing above 500^{o}C, causes a recovery in fatigue crack growth resistance. This was due to loss of coherency and growth of Cu-precipitates. Ageing at 700^{o}C, results in formation of fresh martensite islands and this in turn causes a decrease in the fatigue crack growth resistance.

From the present investigation, it is possible to develop an appreciation of the role played by microstructural constituents in controlling the deformation processes and the fracture behaviour of HSLA-100 steel. Since fatigue crack growth is also governed by accumulation of damage through localised plastic deformation, precipitate coherency is an important factor in controlling its rate. It should be noted that at elevated temperature of ageing, other factors (for e.g. formation of new austenite and martensite beyond 650^{o}C) also influence fatigue crack growth rate and change the trend observed at lower temperatures of ageing.

The conditions (400^{o}C-500^{o}C aged) under which microvoid coalescence was totally suspended in spite of a constant resident population of void initiating carbide and carbo-nitride particles, leading to brittle fracture through cleavage mode, were observed. The effect of tempering of the matrix on fracture mechanics parameters was also evidenced. The evolution of reverted austenite and small martensite islands in microstructure on ageing was responsible for a desirable combination of high strength

and high toughness in HSLA-100 steel, and can be utilised to develop suitable microstructure for critical engineering applications.

The major observations of the effect of variation of microstructure in HSLA-100 steel through quenching and ageing treatments on deformation and fracture modes studied are summarized in Table 7.1 together with inferences drawn on the influence of microstructure that substantiate the observations.

Table-7.1: Summary of the effect of ageing temperature regimes on the properties and characteristics displayed in HSLA-100 steel during deformation, fatigue crack growth and fracture.

Mode of failure	**Aged between 350^{o}C-500^{o}C**	**Aged between 550^{o}C-650^{o}C**	**Aged between 675^{o}C-700^{o}C**
Deformation	YS, UTS increases %El decreases %RA decreases	YS, UTS decreases %El increases %RA increases	YS, UTS increases %El remains almost same %RA remains almost same
Fatigue crack growth	FCGR increases *m* increases *C* decreases	FCGR decreases *m* decreases *C* increases	FCGR increases *m* decreases *C* increases
Fracture	J_c decreases SZW remains constant	J_c increases Apparent trend of increasing *M* and C_1 SZW remains constant	J_c continue to increase Definite increasing trend for *M*, C_1 and C_2 Small increase in SZW
Main microstructural manifestations that are responsible	***Coherent precipitation of Cu***	***Loss of coherency of Cu precipitates, with recovery of matrix***	***Formation of reverted austenite and small martensite islands; continuation of matrix degeneration***

References

References

1. F.B. Pickering: High strength low alloy steels – A decade of progress, Proc. Intl. Symp. Microalloying'75, Washington DC, October 1-3, 1975, p.9
2. C.I. Garcia and A.J. DeArdo: Microalloyed HSLA steels, Proc. World Materials Congress, Chicago, Illinois, September 24-30, 1988, p.291
3. M. Korchynsky (ed.): Proc. Intl. Symp. Micoalloying '75, Union Carbide Corp., New York, 1977
4. A.T. Davenport (ed.): Formable HSLA and Dual Phase Steels, Proc. Intl. Symp. TMS-AIME, Chicago, Illinois, October 26, 1977
5. J.M. Gray (ed.): HSLA Steels - Metallurgy and Applications, Proc. Intl. Conf. Beijing, China, November 1-8, 1985
6. G. Tither and Zhang Showhua (ed.): HSLA Steels: Processing, Properties and Applications, Proc. Intl. Conf. on HSLA Steels, TMS, Warrendale, October 28-November 2, 1990
7. M Mujahid, A.K. Lis, C.I. Garcia and A.J. DeArdo: Key Engineering Materials, 1993, Vol.84-85, p.209
8. C.S. Pande, M.A. Imam, C.L. Vold, E. Dantsker and B.B. Rath: Key Engineering Materials, 1993, Vol.84-85, p.145
9. S. Sivaprasad: Fracture and Fatigue Characteristics of Copper Strengthened HSLA Steels, PhD Thesis, IIT, Kharagpur, India, 1998
10. S.K. Mishra (Pathak), S. Ranganathan, S.K. Das and S. Das: Scripta Materialia, 1998, Vol.39, No.2, p.253
11. S. Das, A. Ghosh, S. Chatterjee and P. Ramachandra Rao: Scripta Materialia, 2003, Vol.48, p.51
12. S. Sivaprasad, S. Tarafder, V.R. Ranganath, S.K. Das and K.K. Ray: Metallurgical and Materials Transaction A, 2002, Vol.33, p.3731
13. J.M. Densley and J.P. Hirth: Scripta Materialia, 1998, Vol.39, No.7, p.881
14. D. Chae and D.A.Koss: Materials Science and Engineering A, 2004, Vol.366, p.299
15. K.S. Chan, Y.M. Pan, D. Davidson and R.C. McClung: Materials Science and Engineering A, 1997, Vol.222, p.1
16. S.P.Bhat and M.E. Fine: Materials Science and Engineering A, 2001, Vol.314, p.90

17. I. Chattoraj, M. Tarafder, S.K. Das and S. Tarafder: Materials Science and Engineering A, 2003, Vol.339, p.136
18. J.P. Christein and J.L Warren: Journal of Ship Production, 1995, Vol.11, p.97
19. W.M. Garrison Jr., J.L. Maloney and A.L. Wojcieszynsky: Key Engineering Materials, 1993, Vol.84-85, p.281
20. G. Spanos, R.W. Fonda, R.A. Vandermeer and A. Matuszeski: Metallurgical and Materials Transaction A, 1995, Vol.26, p.3277
21. J.Y. Yoo, W.Y. Choo, T.W. Park and Y.W. Kim: ISIJ International, 1995, Vol. 35, No.8, p.1034
22. E.J Czyrica, R.E. Link, R.J. Wong, D. A. Aylor, T.W. Montemarano and J.P. Gudas: Naval Engineering, 1990, Vol.102, p.63
23. R.A. Granze, V.E. Lambst and J.J. Harington: Transaction ASM, 1959, Vol.51, p.372
24. R.J. Jesseman and G.C. Schmid: Welding Journal Research Supplement, 1983, Vol.62, No.11, p.321
25. L.G. Kvidahl: Welding Journal, 1985, Vol.64, No.7, p.42
26. I.I.R. Kramer, R.H. Hafner and S.L. Toleman: Transaction of American Institute of Mining & Metallurgical Engineering, 1944, Vol.158, p.138
27. C.H. Lorig and R.R. Adans: “Copper as an alloying element in steel and cast iron”, McGraw-Hill Book Co., New York, 1948
28. K. Tsukada and T. Watanabe: Key Engineering Materials, 1993, Vol.84-85, p.16
29. K.J. Irvine and F.B. Pickering: Journal of Iron Steel Institute, 1983, Vol.201, p.944
30. S.W. Poole: Properties and Selection - Iron and Steel, Metals Handbook, 10^{th} edition, ASM, Metals Park, OH, 1973, Vol.1, p.403
31. Y. Okamura, M. Okushima, H. Tamechiro, T. Kasuya, M. Tanaka, R. Yamaba, H. Inoue and A. Seto: Nippon Steel Technical Report, 1995, Vol.66, p.65
32. T. Zaizen, M. Sato, T. Watanabe, T. Haze, K. Okamoto, Y. Ohno and T. Kanaya: Nippon Steel Technical Report, 1983, Vol.22, p.61
33. R.J. Schmitt and E.H. Phelps: Journal of Metals, 1970, Vol.9, p.47
34. F. Blekkenhost, G.M. Ferrari, C.J. Van Der Wekken and F.P. Ijesseling: Corrosion, 1988, Vol.23, p.165
35. R. Bruno, A. Tamba and G. Bombara: Corrosion, 1973, Vol.29, p.95
36. W.A. Laura: Materials Performance, 1991, Vol.9, p.62
37. Y. Yuichi: Corrosion, 1982, Vol.38, p.156

38. F. Blekkenhost, G.M. Ferrari, C.J. Van Der Wekken and F.P. Ijesseling: Corrosion, 1986, Vol.21, p.163
39. M. Staratmann, K. Bohnenkamp and T. Ramachandran: Corrosion Science, 1987, Vol.27, p.905
40. I. Suzuki and Y. Hisamatsu: Journal of Electrochemical. Society, 1984, Vol.10, p.2210
41. E.E. Fletch: High Strength Low Alloy Steels - Status, Selection and Physical Metallurgy, Metals and Ceramic Information Center, Battelle Press, Columbus, Ohio, 1979, p.1
42. W.C. Leslie: Metallurgical Transaction A, 1972, Vol.3, p.5
43. B.A. Graville: Cold Cracking in Welds in HSLA Steels, ASM, Metals Park, OH, 1978, p.85
44. L.E. Collins, J.D. Boyd, J.A. Jalkman, L.D. Bailey and M.R. Krishnadev: Microalloyed HSLA steels, World Materials Congress, Chicago, Illinois, September 24-30, 1988, p.607
45. C.I. Garcia, M. Mujahid, A.J. DeArdo: Proc. Intl. Conf. on High Performance Steels for Structural application, Cleveland, Ohio, 1995, p.135
46. E.C. Hamre and A.M. Gilroy-Scott: Proc. Intl. Symp. Microalloying'75, Washington DC, October 1-3, 1975, p.375
47. J.M. Gray: Microalloyed HSLA steels, World Materials Congress, Chicago, Illinois, September 24-30, 1988, p.61
48. T. Gladman: The Physical Metallurgy of Microalloyed Steels, Institute of Materials, London, 1997, p.38
49. R. Hammer and R.W. Simon: HSLA Steels, Technology and Applications, Proc. Intl. Conf., Philadelphia, ASM, 1983, p.359
50. W. Roberts: HSLA Steels, Technology and Applications, Proc. Intl. Conf., Philadelphia, ASM, 1983, p.33
51. M. Pontremoli, P. Bufalimi, A. Aprile and C. Jannml: Metals Technology, 1984, Vol.11, p.504
52. F. Fukuda, T. Hashimoto and K. Kunishige: Microalloying'75, Proc. Intl. Symp., Washington DC, October 1-3, 1975, p.136
53. K.J. Irvine: Steel Strengthening Mechanisms, Climax Molybdenum, Zurich, 1969, p.55
54. W.B. Morrison: Scandinavian Journal of Metallurgy, 1980, Vol.9, p.83

55. L. Meyer, F. Heisterkamp and W. Mueschenborn: Microalloying'75, Proc. Intl. Symp., Washington DC, October 1-3, 1975, p.153
56. A. Ghose, B. Mishra, S. Das and S. Chatterjee: Materials Science and Engineering A, 2005, Vol.396, p.330
57. Z. Xiaogong, X. Dianpel, A. Liege, Y. Weixun: HSLA Steels: Processing, Properties and Applications, Intl. Conf. on HSLA Steels, TMS, Warrendale, October 28-November 2, 1990, p.171
58. S.F. Media, M. Chapa, P. Valles, A. Quispe and M.I. Vega: ISIJ International, 1999, Vol.39, No.9, p.930
59. M. Prikryl, A. Kroupa, G.C. Weatherly and S.V. Subramanian: Metallurgical and. Materials Transaction A, 1996, Vol.27, p.1149
60. B. Dutta, E. Valdes and C.M. Sellars: Acta Materialia, 1992, Vol.40, No.4, p.653
61. E. Hornbogen and R.C. Glenn: Transaction of Metallurgical Society, AIME, 1960, Vol.218, p.1064
62. E. Hornbogen: Acta Materialia, 1962, Vol.10, p.525
63. E. Hornbogen: Transaction of American Society for Metals, 1964, Vol.57, p.120
64. K.C. Russel and L.M. Brown: Acta Materialia, 1970, Vol.20, p.969
65. S.R. Goodman, S.S. Brenner and J.R. Low: Metallurgical Transaction A, 1974, Vol.4, p.2363
66. T. Harry and D.J. Bacon: Acta Materialia, 2002, Vol.50, p.209
67. R. Monzen, K. Takada, and K. Matsuda: Metallkunde, 2003, Vol.94, No.11, p.1241
68. K. Nakashima, Y. Futamura, T. Tsuchiyama and S. Takaki: ISIJ International, 2002, Vol.42, No.12, p.1541
69. Metals Hand Book: Metallography, Structure and Phase diagrams, 8^{th} edition, ASM, Metals Park, OH, 1973, Vol.8, p.273
70. H.Okada, S. Sekino, Y. Hosoi and T. Murata: Copper in Iron and Steel, John Wiley and Sons, New York, 1982, p.83
71. C.I. Garcia, A.J. DeArdo, E. Raykin and J.D.S. Defilippi: High Performance Steel for Structural Applications, Proc. Intl. Symp., Cleveland, OH, 1995, p.155
72. M. Mujahid, A.K. Lis, C.I. Garcia and A.J. DeArdo: Journal of Materials Engineering and Performance, 1998, Vol.7, No.2, p.247
73. S.S. Ghasemi, D. Bandadouki, D.Yu and D.P. Dunne: ISIJ International, 1996, Vol.36, p.61

74. D.P. Dunne, S.S.B. Ghasemi, D. Yu and G. Krauss: Metallurgical and Materials Transaction A, 1996, Vol.27, p.1573
75. A.N. Bhagat, S.K. Pabi, S. Ranganathan and O.N. Mohanty: ISIJ International, 2004, Vol.44, No.1, p.115
76. M.R. Krishnadev and A. Galibos: Metallurgical Transaction A, 1974, Vol. 6, p.300
77. E.J. Czyryca: Advances in Low Carbon High Strength Ferrous Alloys, Proc. Intl. Conf., Trans Tech Publication, Switzerland, 1993, p.491
78. M. Mujahid, A.K. Lis, C.I. Garcia, A.J. DeArdo and R.S. Gilbert: Fundamentals of Ageing and Tempering in Bainite and Martensite Steel Products, Proc. Intl. Symp., Montreal, Quebec, Canada, October 25-28, 1992, p.345
79. T. Imao, O. Chiaki, T. Tomo and S. Hiroshi: Thermomechanical Processing of High Strength Low Alloy Steels, Butterworths, 1988, p.1
80. P. Bufalini, M. Pontremoli, M. Ghersi, A. Aprile and C. Jannone: Accelerated Cooling of Steel, Proc. Intl. Conf., TMS-AIME, Pittsburg, PA, 1985, p.387
81. I. Kozasu: Accelerated cooling of Steel, Proc. Intl. Conf., TMS-AIME, Pittsburg, PA, 1985, p.15
82. J.Y. Yoo, W.Y. Choo, T.W. Park and Y.W. Kim: ISIJ International, 1995, Vol.35, p.1034
83. E.J. Czyryca: Development of Low-Carbon Copper Strengthened HSLA Steel plate for Naval Ship Construction, R&D Report No. DTRC-SME-90/21, Ship Materials Engineering Dept., David Taylor Research Center, Bethesda, MD 20084-5000, 1990
84. J.M.B. Losz and K.D. Challenger: Trends in Welding Research, Proc. Intl. Conf., Gattisburg, Tennesee, USA, May 14-18, 1989, p.229
85. G. Spanos, R.W. Fonda and R.A. Vandermeer: Processing-Microstructure-Property Relationship in Advanced Naval Steel Welds, NRL Review, NRL/PU/5230-95-274, Naval Research Lab., Washington, May 1995
86. M.A. Cooke, B.H. Chapman and S.W. Thomson: Scripta Materialia, 1992, Vol.26, p.1553
87. G. Spanos, R.W. Fonda, R.A. Vandermeer and A. Matuszeski: Metallurgical and Materials Transaction A, 1995, Vol.26, p.3277
88. M.R. Krishnadev, V.K. Vasudevan, K.D. Challenger, J.T. Bower and J.T. McGrath: Trends in Welding Research, Proc. Intl. Conf., Gattisburg, Tennesee, USA, May 14-18, 1989, p.799

89. V.J. Pogorzhelskyj, Y.J. Matrosov and A.G. Nashilov: Microalloying'75, Proc. Intl. Symp., Washington DC, October 1-3, 1975, p.100
90. F.B. Pickering: Physical Metallurgy of Steels, McGraw Hill, New York, 1981
91. A. Massip and L. Meyer: Stahlund Eisen, 1978, Vol.98, p.983
92. E.O. Hall: Proceedings of Physical. Society of London, 1951, Vol.648, p.747
93. N.J. Petch: Journal of Iron and Steel Institute, 1953, Vol.25, p.174
94. R. Priestner and De Los Rios: Heat treatment'76, Metals Society, 1976, p.129
95. M. Cohen and W.S. Owen: Microalloying'75, Proc. Intl. Symp., Washington DC, October 1-3, 1975, p.2
96. F. Heisterkamp and L. Meyer: Thyssen Technical Report, 1971, Vol.1&2, p.55
97. J.E. Baeley and P.B. Hirsch: Philosophical. Magazine, 1960, Vol.5, p.485
98. A.S. Keh: Direct observation of imperfection of crystals, Interscience, New York, 1969
99. T.N. Baker: Hot Working and Forming Process, The Metals Society, London, 1979, p.32
100. D.T. Gawne and G.M.H. Lewis: Journal of Materials Science and Technology, 1985, Vol.1, p.183
101. G.A. Roberts and R.F. Mehl: Transaction of. American Society for Metals,1943, Vol.31, p.613
102. H.W. Paxton: Transformation and Hardenability in Steel, Proc. Intl. Symp., Michigan, Climax Molybdenum Co. Ltd., 1967, p.3
103. H.I. Aaroson and H.A. Domain: Transaction of AMIE, 1966, Vol.236, p.781
104. J.L. Lee, S.C. Wang and G.H. Chang: Journal of Materials Science and Technology, 1989, Vol.5, p.674
105. T. Tanaka: International Metal Review, 1981, Vol.4, p.185
106. F.B. Pickering: HSLA Steels Technology and Applications, Proc. Intl. Conf., Philadelphia, American Society for Metals, 1983, p.1
107. Y.E. Smith, A.P. Coldren and R.L. Cryderman: Towards Improved Ductility and Toughness, Proc. Intl. Conf., Kyoto, Climax Molybdenum Co. Ltd., 1972, p.119
108. H.D.K.H. Bhadeshia: Bainite in Steels, Transformation Microstructure and Properties, The Institute of Materials, London, 1992
109. N.J. Kim, A.J. Yang and G. Thomas: Metallurgical Transaction A, 1985, Vol.16, p. 471

110. G.V. Kurdjumov: Phenomena occurring in the quenching and tempering of steel, 12th Hadfield Memorial Lecture, Journal of Iron and Steel Institute, 1960, p.195
111. Z. Nishiyama: Martensite Transformation (Eng. Ed.), Academic Press, New York, 1978
112. S.W. Thompson, D.J. Colvin and G. Krauss: Metallurgical Transaction A, 1990, Vol.21, p.1493
113. A.J. DeArdo: ISIJ International, 1995, Vol.35, No.8, p.946
114. A.D. Wilson, E.G. Hamburg, D.J. Colvin, S.W. Thompson and G.Krauss: Microalloying'88, Proc. Intl. Conf., World Materials Congress, American Society for Metals, Metals Park, OH, September, 1988, p.259
115. R.J. Jesseman, and G.J. Murphy: Journal of Heat Treating, 1984, Vol.3, No.3, p.228
116. B.H. Chapman, M.A. Cooke and S.W. Thompson: Scripta Materialia, 1992, Vol.26, p.1547
117. D. Wenpu, F. Zuobao, Y. Long: Materials Characterization, 1996, Vol.37, p.167
118. H. Kwun and G.L. Brkhardt: Journal of Applied Physics, 1987, Vol.61, p.1576
119. D.K. Bhattacharya: Journal of Non Destructive Evaluation, 1996, Vol.17, p.1
120. J.F. Bussiere, M.Lord and M. Nott: Nondestructive Testing, Oxford, UK, Pergamon Press, 1987, p.1863
121. R. Ranjan, D.C. Jiles and P.K. Rastogi: IEEE Transaction on Magnetics, 1987, Vol.23, p.1869
122. D.C. Jiles: Physics Status Solidi, 1988, Vol.108, p.417
123. D.C. Jiles: Journal of Physics D: Applied. Physics, 1988, Vol.21, p.1196
124. A. Mitra, M.R. Govindraju and D.C. Jiles: IEEE Transaction on Magnetics, 1995, Vol. MAG-31, p.4053
125. M.N. Mikheev and E.S. Gorkunov: Soviet Journal of Non Destructive Testing, 1982, Vol.17, p.579
126. J.B. Goodenough: Physical Review, 1954, Vol.95, p.917
127. P. Haasen: Materials Science and Engineering, 1972, Vol.9, p.191
128. H. Sakamoto, M. Okada and M. Homma: IEEE Transaction on Magnetics, 1987, Vol. MAG-23, p.1869
129. V. Moorthy, S. Vaidyanathan, T. Jayakumar, Baldev Raj and B.P. Kashyap: Metallurgical and Materials Transaction A, 2000, Vol.31, p.1053

130. Baldev Raj, V. Moorthy, T. Jayakumar and K. Bhanu Sankara Rao: International Materials Review, 2003, Vol.48, p.273
131. K.S. Ryu, S.H. Nahm, Y.B. Kim, K.M. Yu and D. Son: Journal of Magnetism and Magnetic Materials, 2000, Vol.222, p.128
132. S. K. Das, A. Joarder and A. Mitra: NDT&E International, 2004, Vol.37, p.243
133. H.E. Kissinger: Analytical Chemistry, 1957, Vol.29, p.1702
134. G.R. Irwin: Handbuch der Physik, VI, Springer, Berlin, 1958, p.551
135. D.S. Dugdale: Journal of the Mechanics and Physics of Solids, 1960, Vol.8, p.100
136. G.T. Hahn and A.K. Rosenfield: International Journal of Fracture Mechanics, 1968, Vol.4, p.79
137. S. Banerjee: Engineering Fracture Mechanics, 1981, Vol.15, p.343
138. J.A. Jacobs : Philosophical Magazine, 1950, Vol.F41, p.349
139. F.A. McClintock: Journal of Applied Mechanics, 1958, Vol.25, p.582
140. J.R. Rice and G.F. Rosengren: Journal of the Mechanics and Physics of Solids, 1968, Vol.16, p.1
141. F.A. McClintock and G.R. Irwin: ASTM STP 381, 1965, p.84
142. G.T. Hahn and A.R. Rosenfield: Acta Materialia, 1965, Vol.13, p.293
143. G.T. Hahn, R.G. Hoagland and A.R. Rosenfield: Metallurgical Transaction A, 1972, Vol.3, p.1189
144. A. Wells: British Welding Journal, 1963, Vol.10, p.563
145. J.N. Goodier and F.A. Field: Fracture of solids, Wiley, New York, 1963, p.103
146. F.M. Burdekin and D.E.W. Stone: Journal of Strain Analysis, 1966, Vol.1, p.145
147. D.P. Rooke and F.J. Bradshaw: Fracture, Chapman & Hall, UK, 1969, p.46
148. D. Broek: Elementary Engineering Fracture Mechanics, Martnus Nijihoff Publication, The Netherlands, 1979, p.224
149. British Standards Institution Document BS5762: Methods for Crack Opening Displacement (COD) testing, 1979
150. E 1290-89: Standard Test Method for Crack Tip Opening Displacement (CTOD), Fracture Toughness Measurement, Annual Book of ASTM Standards, ASTM, Philadelphia, PA, Vol.03.01., 1994, p.946
151. R.W. Nicolas, F.M. Burdekin, A. Cowan, D. Elliot and T. Ingham: Practical Fracture Mechanics for Structural Steel, Proc. Intl. Conf., Chapman & Hall, Risley, England, April 1969
152. J.N. Robinson and A.S. Tetelman: ASTM STP 559, 1974, p.139

153. A.A. Wells: The Status of COD in Fracture Mechanics, Proc. of 3rd Canadian Congress of Applied Mechanics, Calgary, 1971, p.59
154. D.J. Hayes and C.E. Turner: International Journal of Fracture Mechanics, 1974, Vol.10, p.1
155. M.G. Dawes: ASTM, STP 668, 1979
156. J.R. Rice: Journal of Applied Mechanics, 1968, Vol.35, p.379
157. J.W. Hutchinsol: Journal of the Mechanics and Physics of Solids, 1968, Vol.16, p.13
158. J.D. Eshelby: Solid State Physics, Academic, New York, 1956, Vol.3, p.79
159. G.P. Cherepanov: Journal of Applied. Mechanics Translation, 1967, Vol. 31, p.504
160. J.A. Begley and J.D. Landes: ASTM, STP 514, 1972, p.1
161. J.D.G. Sumpter and C.E. Turner: International Journal of Fracture Mechanics, 1973, Vol.9, p.320
162. J.D. Landes, H. Walker and G.A. Clarke: ASTM STP 668, 1979, p.266
163. J.D. Landes and J.A. Begley: ASTM STP 460, 1974, p.170
164. E 813-89: Standard Test Method for J_{1C}, A Measurement of Fracture Toughness, Annual Book of ASTM Standards, ASTM, Philadelphia, USA, Vol.03.01, 1994
165. J.R. Rice, P.C. Paris and J.G. Merkle: ASTM STP 536, 1973, p.231
166. J.P.G. Sumpter and C.E. Turner: ASTM STP 601, 1976, p.3
167. C.E. Turner: Materials Science and Engineering, 1976, Vol.11, p.275
168. T. Hollstein, N. Schmitt and G. Blauel: Journal of Test Evaluation, 1983, Vol.11, p.174
169. M.G. Dawes: Journal of Pressure Vessel and Piping, 1978, Vol.6, p.165
170. G.R. Irwin: ASTM Bulletin, 1960, p.29
171. E 1152-87: Standard Test Method for Determining J-R Curves, Annual Book of ASTM Standards, Vol.03.01, ASTM, Philadelphia, PA, 1994, p.847
172. E 399-90: Test Method for Plane–Strain Fracture Toughness of Metallic Materials, Annual Book of ASTM Standards, ASTM, Philadelphia, PA, Vol. 03.01, 1994, p.847
173. E 561-92: Standard Practice for R-Curve Determination, Annual Book of ASTM Standards, ASTM, Philadelphia, PA, 1994, Vol. 03.01, p.597
174. P. Doig and K.R. Abbott: Journal of Testing and Evaluation, 1984, Vol.12, p.297
175. S.J. Hudak Jr. and A. Saxena: International Journal of Fracture,1978, Vol.14, p.453
176. S.X. Wu : International Journal of Fracture, 1984, Vol.24, p.33

177. J.M. Lowes and G.D. Fearnehough: Engineering Fracture Mechanics, 1971, Vol.3, p.103
178. F. Nilson and B. Ostensson: Engineering Fracture Mechanics, 1978, Vol.10, p.223
179. K.H. Schwalbe and D. Hellmann: Journal of Testing and Evaluation, 1981, Vol.9, p.128
180. P.C. Paris, H. Tada, A.Zahoor and H. Ernst: ASTM STP 668, 1979, p.5
181. R.O. Ritchie and A.W. Thompson: Metallurgical Transaction A, 1985, Vol.16, p.233
182. C.F. Shih, G.A. Clarke: Journal of Testing and Evaluation, 1979, Vol.7, p.49
183. J.G. Merkle and H.T. Corton: Journal of Pressure Vessel Technology, 1974, Vol.96, p.286
184. J.R. Rice, W.J. Drugan and T.L. Sham: ASTM STP 700, 1980, p.189
185. P. Paris and J. Erdogan: Journal of Basic Engineering, 1963, Vol.85, p.528
186. J.F. Knott: Fundamentals of Fracture Mechanics, Butterworths, 1973
187. A.K. Head: Philosophical Magazine, 1953, Vol.44, p.925
188. N.E. Frost and D.S. Dugdale: Journal of the Mechanics and Physics of Solids, 1958, Vol.6, p.92
189. N.E. Frost, J. Holden and C.E. Phillips: Crack Propagation, Proc. Intl. Symp., Cranfield, 1961, Vol.1, p.166
190. H.W. Liu: Journal of Basic Engineering, 1961, Vol.83, p.23
191. B. Tomkin: Philosophical Magazine, 1971, Vol.23, p.687
192. A.J. McEvily and W. Illg: Nasa Technical Note 4394, 1958
193. N.E. Frost, L.P. Pook and K. Denton: Engineering Fracture Mechanics, 1971, Vol.3, p.109
194. S. Pearson: Nature, 1966, Vol.211, p.1077
195. P.R.V. Evans, N.B. Owen and B.E. Hopkin: Journal of Iron and Steel Institute, 1970, Vol.208, p.560
196. C.R. Carman and M.F. Schuler: Journal of Iron and Steel Institute, 1970, Vol.208, p.463
197. R.O. Ritchie and J.F. Knott: Acta Materialia, 1973, Vol.21, p.639
198. D. Broek: Fracture, Proc. 2nd Intl. Conf., Brighton, Chapman and Hall, 1969, p.754
199. R.G. Forman, V.E. Kearney and R.M. Engle: Journal of Basic Engineering, 1967, Vol.89, p.459

200. E24.04.04. ASTM Task Group, Proposed Appendix X2: Recommended Practice for Determination of Fatigue Crack Opening Load from Compliance, 1990
201. W. Elber: ASTM STP 486, 1971, p.230
202. E-8M-03, Standard test method for tensile testing of metallic materials (Metric), Annual Book of ASTM Standards, Vol. 03.01, ASTM, West Conshohocken, PA, 2003
203. M.T. Miglin, J.P. Hirth, A.R. Rosenfield and W.A.T. Clark: Metallurgical Transaction A, 1986, Vol.17, p.791
204. D.P. Dune, S.S.B. Ghasemi and D. Yu: ISIJ International, 1996, Vol.36, p.324
205. S.W. Thompson and G. Krauss: Metallurgical and Materials Transaction A, 1996, Vol.27, p.1573
206. B. Soylu and R.W.K. Honeycombe: Materials Science and Technology, 1991, Vol.17, p.137
207. K. Osamura, H. Okuda, S. Ochiai, M. Takashima, K. Asano, M. Furusaka, K. Kishida and F. Kurosawa: ISIJ International, 1994, Vol.4, p.359
208. T.L. Anderson: Fracture Mechanics-Fundamentals and Applications, Second Ed., CRC Press, Boca Raton, New York, 1995, p.265
209. A. Mitra, A.K. Panda, S.R. Singh, V. Rao and P. Ramachandrarao: Philosophical Magazine, 2003, Vol.83, p.1495
210. E-647-00, Standard Test Method for Measurement of Fatigue Crack Growth Rates, Annual Book of ASTM Standards, Vol. 03.01, ASTM, West Conshohocken, PA, 2003
211. S. Tarafder: “High temperature crack growth in 2.25 Cr-1 Mo steel”, Ph.D. Thesis, University of Cambridge, UK, 1990
212. S. Sivaprasad, S. Tarafder, V.R. Ranganath, M. Tarafder, K.K. Ray: Corrosion Science, 2006, Vol.48, p.1996
213. G.H. Bray, M. Glazov, R.J. Rioja, D. Li, R.P. Gangloff: International Journal of Fatigue, 2001, Vol.23, p.S265
214. L.W. Tsay, T.S. Chern, C.Y. Gau, J.R.Yang: International Journal of Fatigue, 1999, Vol.21, p.857
215. V. Sinha, W.O. Soboyejo: Materials Science and Engineering A, 2001, Vol.319-321, p.607

216. S. Shademan, V. Sinha, A.B.O. Soboyejo, W.O. Soboyejo: Mechanics of Materials, 2004, Vol.36, p.161

217. S. Sankaran, V. Subramanya Sarma, K.A. Padmanabhan, Koethe G. Jaeger: Materials Science and Engineering A, 2003, Vol.362, p.249

218. E-1820-99a, Standard Test Method for Measurement of Fracture Toughness, Annual Book of ASTM Standards, Vol. 03.01, ASTM, West Conshohocken, PA, 2003

219. E 813-89: Standard Test Method for J_{1C} , A Measurement of FractureToughness, Annual Book of ASTM Standards, Vol.03.01.ASTM, Philadelphia, USA, 1994

220. S. Sivaprasad, S. Tarafder, V.R. Ranganath and K.K. Ray: Fatigue Fracture Engineering Material and Structure, 2004, Vol.27, p.897

221. A. Halim, W. Dahl and K.E. Hagedorn: Engineering Fracture Mechanics, 1998, Vol. 31, p.857

222. H. Kobayashi, H. Nakamura and H. Nakazawa: “Evaluation of blunting line and elastic-plastic fracture toughness”, Elastic-Plastic Fracture: Second Symposium, Vol II, Fracture resistance curves andengineering applications, ASTM STP 803. American Society for Testing and Materials, Philadelphia, 1983, p.420.

List of Publications

A. Publications from Thesis

1. **S.K. Das**, S. Sivaprasad, S. Das, S. Chatterjee and S. Tarafder: “The Effect of Variation of Microstructure on Fracture Mechanics Parameters of HSLA-100 Steel”- Materials Science and Engineering A, 2006, Vol.431, p.68
2. **S.K. Das**, S. Chatterjee and S. Tarafder: “Study on Tensile Fracture Behaviour of Microstructurally Engineered Copper Bearing High Strength Low Alloy Steel”- Materials Science and Technology, 2006, Vol.22, No.12, p.1409
3. **S.K. Das,** N. Narasaiah, S. Sivaprasad, S. Chatterjee and S.Tarafder: “Effect of Ageing on Fatigue Crack Growth Behaviour of Cu-Bearing HSLA-100 Steel”- Materials Science and Technology, 2007, Vol.23, No.2 , p.177
4. A.K. Panda, **S.K. Das**, A. Mitra, D.C. Jiles, C.C.H. Lo: “Evaluation of Deformation Behaviour of HSLA-100 Steel using Magnetic Hysteresis technique”- IEEE Trans. on Magnetics, 2006 Oct., Vol. 42, No.10, p.3264
5. **S.K. Das,** S. Tarafder, A.K. Panda, S. Chatterjee and A. Mitra: “Magnetic and mechanical properties of Cu-strengthened aged HSLA-100 steel”- Philosophical Magazine, 2007, Vol. 87, No.32, p.5065

B. Research Papers (from Thesis) Presented in Conferences/Seminars

1. **S.K. Das**, S. Shivaprasad, S. Chatterjee and S. Tarafder: "Influence of Ageing on Microstructure and Properties of Cu-Strengthened High Strength Low Alloy (HSLA) Steel" National conf. on Advances in Materials and their Processing (AMTP-2003), BEC, Bagalkot, Karnataka, India, Dec.22-23, 2003
2. **S.K. Das**, S.Tarafder, S. Chatterjee and A. Mitra: "Characterisation of heat treated HSLA steel by magnetic technique", National Seminar on NDE-2003, ISNT, Thiruvananthapuram, Kerala, India, Dec.11-13, 2003
3. **S.K. Das**, S. Shivaprasad, S. Chatterjee and S. Tarafder: "Characterisation of Flow Behaviour of Cu-Strengthened High Strength Low Alloy Steel", Annual Technical Meeting (ATM) of Indian Institute of Metals, Tiruvananthapuram, Kerala, India, 14-17th Nov, 2004

4. S. Tarafder, **S.K. Das** and S. Sivaprasad, E. Roos and M. Sidenfuss: " The Effect of Variation of Microstructure on Fracture Mechanics Parameters ", 3rd Indo-German Seminar on Advances in Structural Integrity & Safety, BARC, Mumbai, India, Nov. 15-17, 2005
5. **S. K. Das**, S. Tarafder and S. Chatterjee –Influence of copper precipitation on fracture mechanics parameters in a microalloyed HSLA steel-Microalloyed Steels – Emerging Technologies and Applications- Proceedings of the Intl. conf. on Microalloyed Steels- 9-11 March 2007 Kolkata India
6. **S. K. Das**, S. Chatterjee and S. Tarafder -Deformation Behaviour of Cu-Strengthened HSLA Steel-National Seminar on Deformation and Damage-2007, 24-25 January,2007, organized by Metallurgical and Material Engineering Dept. Jadavpur University, Kolkata
7. **S. K. Das**, N. Narasaiah, S. Sivaprasad and S. Tarafder –Effect of Microstructure on Deformation and Fracture Behaviour of HSLA Steel-Symposium on Fatigue, Fracture and Integrity Assessment, 6-7 March 2007, organized by Tata Steel and Indian Institute of Welding, Jamshedpur

C. Author's other Publications on HSLA Steel

1. S.K.Mishra (Pathak), S.Ranganathan**, S.K.Das** and Samar Das: "Investigations on precipitation characteristics in a high strength low alloy (HSLA) steel" – Scripta Materialia, 1998, Vol.39, No.2, pp.253-259
2. S. Shivaprasad, S. Tarafder, V.R. Ranganath, **S.K. Das** and K.K. Ray: "Effect of prestrain on stretch-zone formation during ductile fracture of Cu-strengthened high-strength low-alloy steels" - Metallurgical and Materials Transaction A, 2002, Vol. 33, p.3731
3. I Chattoraj, M. Tarafder, **S.K. Das**, S. Tarafder: "Hydrogen induced brittle crack growth in Cu-strengthened HSLA-100 steels" - Materials Science and Engineering A, 2003, Vol.339, p.136
4. A. Kumar, S. Tarafder, P. Mukherjee, **S.K. Das**, B. Ravikumar, I. Chattoraj: "Effect of plasma ion implantation on the hydrogen embrittlement of Cu strengthened HSLA-100 steel"- Journal of Materials Science, 2003, Vol.38, p.2667

5. I. Chottoraj, A. Kumar, **S.K. Das**, M. Tarafder and S. Tarafder: “Factors influencing the extent of hydrogen-enhanced brittle cracking in a Cu-strengthened HSLA steel during monotonic loading” - Metallkunde, Nov. 2003, Vol. 94, p.1228
6. I. Chattoraj, A. Kumar, **S.K. Das**, and S. Tarafder: - “Different stages in the hydrogen embrittlement of a high strength steel” - Metals Materials and Process, 2004, Vol.16, No. 2-3, p.307